OAK RIDGE
NATIONAL LABORATORY
MANAGED BY UT-BATTELLE
FOR THE DEPARTMENT OF ENERGY

ORNL/TM-2005/218

Status of Physics and Safety Analyses for the Liquid-Salt-Cooled Very High-Temperature Reactor (LS-VHTR)

December 2005

UT-BATTELLE
ORNL-27 (4-00)

ORNL/TM-2005/218

Status of Physics and Safety Analyses for the Liquid-Salt-Cooled Very High-Temperature Reactor (LS-VHTR)

D. T. Ingersoll

Contributors:

K. T. Clarno, C. W. Forsberg, and J. C. Gehin
Oak Ridge National Laboratory

R. W. Christensen, C. B. Davis, G. L. Hawkes, and J. W. Sterbentz
Idaho National Laboratory

T. K. Kim, T. A. Taiwo, and W. S. Yang
Argonne National Laboratory

Issued: December 2005

Prepared by
OAK RIDGE NATIONAL LABORATORY
Oak Ridge, Tennessee 37831-6283
managed by
UT-BATTELLE, LLC
for the
U.S. DEPARTMENT OF ENERGY
under contract DE-AC05-00OR22725

This page intentionally blank

CONTENTS

Page

This page intentionally blank

LIST OF FIGURES

Figure **Page**

This page intentionally blank

LIST OF TABLES

Table **Page**

This page intentionally blank

LIST OF ACRONYMS

ANL	Argonne National Laboratory
AVR	Arbeitsgemeinshaft Versuchsreaktor
BP	burnable poison
CVR	coolant void reactivity
ENDF/B-V	Evaluated Nuclear Data Files Version 5
ENDF/B-VI	Evaluated Nuclear Data Files Version 6
ESC	Extended Step-Characteristics
FTC	fuel temperature coefficient
GT-MHR	gas-turbine modular high-temperature reactor
INL	Idaho National Laboratory
LOFC	loss of forced circulation
LRM	linear reactivity model
LS-VHTR	liquid-salt-cooled very high-temperature reactor
LWR	light-water reactor
MCNP5	Monte Carlo N-Particle code Version 5
MSR	molten salt reactor
MSRE	Molten Salt Reactor Experiment
NGNP	Next Generation Nuclear Plant
NVR	net void reactivity
ORNL	Oak Ridge National Laboratory
pcm	percent milli
PRISM	Power Reactor Inherently Safe Module
RERTR	Reduced Enrichment for Research and Test Reactors
RVACS	reactor vessel auxiliary cooling system
S-PRISM	Super Power Reactor Inherently Safe Module
THTR	Thorium High-Temperature Reactor
VHTR	very high-temperature reactor

This page intentionally blank

ABSTRACT

A study has been completed to develop a new baseline core design for the liquid-salt-cooled very high-temperature reactor (LS-VHTR) that is better optimized for liquid coolant and that satisfies the top-level operational and safety targets, including strong passive safety performance, acceptable fuel cycle parameters, and favorable core reactivity response to coolant voiding. Three organizations participated in the study: Oak Ridge National Laboratory (ORNL), Idaho National Laboratory (INL), and Argonne National Laboratory (ANL). Although the intent was to generate a new reference LS-VHTR core design, the emphasis was on performing parametric studies of the many variables that constitute a design. The results of the parametric studies not only provide the basis for choosing the optimum balance of design options, they also provide a valuable understanding of the fundamental behavior of the core, which will be the basis of future design trade-off studies.

A new 2400-MW(t) baseline design was established that consists of a cylindrical, nonannular core cooled by liquid $^{7}Li_2BeF_4$ (Flibe) salt. The inlet and outlet coolant temperatures were decreased by 50°C, and the coolant channel diameter was increased to help lower the maximum fuel and vessel temperatures. An 18-month fuel cycle length with 156 GWD/t burnup was achieved with a two-batch shuffling scheme, while maintaining a core power density of 10 MW/m^3 using graphite-coated uranium oxicarbide particle fuel enriched to 15% ^{235}U and assuming a 25 vol-% packing of the coated particles in the fuel compacts.

The revised design appears to have excellent steady-state and transient performance. The previous concern regarding the core's response to coolant voiding has been resolved for the case of Flibe coolant by increasing the coolant channel diameter and the fuel loading. Also, the LS-VHTR has a strong decay heat removal performance and appears capable of surviving a loss of forced circulation (LOFC) even with failure to scram. Significant natural convection of the coolant salt occurs, resulting in fuel temperatures below steady-state values and nearly uniform temperature distributions during the transient.

This page intentionally blank

1. INTRODUCTION

The Liquid-Salt-Cooled Very High-Temperature Reactor (LS-VHTR) is a variant of the gas-cooled very high-temperature reactor (VHTR) concept and combines four established technologies in a new way: (1) coated-particle graphite-matrix fuels successfully used in helium-cooled reactors, (2) passive safety systems and plant designs previously developed for liquid-metal-cooled fast reactors, (3) low-pressure liquid-salt coolants studied extensively for use in liquid-fueled reactors, and (4) high-temperature Brayton power cycles. The new combination of technologies enables the design of a high-power [2400 to 4000 MW(t)], high-temperature (850 to 950ºC) reactor with fully passive safety capability and the economic production of electricity or hydrogen [Forsberg, 2003].

Although the primary novelty of the LS-VHTR is the use of liquid-salt coolant, its technical basis is derived from billion-dollar programs in the 1950s and 1960s that developed the technology for use of liquid salts in nuclear systems. Two experimental reactors were built and successfully operated. The Aircraft Reactor Experiment was a 2.5-MW(t) reactor that was operated in 1954 at a peak temperature of 860ºC and used a sodium-zirconium fluoride salt. This was followed in 1965 by the Molten Salt Reactor Experiment (MSRE), an 8-MW(t) reactor that used a lithium-beryllium fluoride salt and demonstrated most of the key technologies for a power reactor. In addition, test loops with liquid salts were operated for hundreds of thousands of hours, and materials of construction were code qualified to 750ºC. Unlike these earlier molten salt reactors (MSR) that circulated the fuel within the coolant, the LS-VHTR uses the same solid fuel as the gas-cooled VHTR and a clean liquid salt as a coolant. However, the earlier MSR programs demonstrated several critical technologies for the LS-VHTR, and the results are documented in more than 1000 technical reports.

The primary driver for the LS-VHTR is its potential for significant improvements in plant economics. Preliminary overnight capital costs of a 2400-MW(t) LS-VHTR have been determined relative to other higher-temperature reactor concepts (gas-cooled and sodium-cooled) on a common output basis. The overnight capital costs for a LS-VHTR are estimated to be about one-half that of either General Electric's Super Power Reactor Inherently Safe Module (S-PRISM) design or General Atomics' Gas-Turbine Modular High-Temperature Reactor (GT-MHR) design [Ingersoll, 2004]. The improved economics relative to the modular S-PRISM and GT-MHR is an expected consequence of the economy of scale, because the LS-VHTR electrical output is approximately four times that of the modular reactors but should have similar physical size and complexity. The potential for improved economics compared with light-water reactors, for a plant of equal output power, is a consequence of higher efficiencies provided by higher coolant temperatures, higher power cycle power density, a low-pressure containment, and the elimination of active safety equipment.

1.1 REFERENCE LS-VHTR DESIGN

The LS-VHTR uses coated-particle graphite-matrix fuels and a liquid-fluoride-salt coolant. The fuel is the same type that has been successfully used in high-temperature gas-cooled reactors such as Peach Bottom, Fort St. Vrain, the Arbeitsgemeinshaft Versuchsreaktor (AVR), and the Thorium High-Temperature Reactor (THTR). This type of fuel can be subjected to fuel-failure temperatures in excess of 1600°C without damage. The optically transparent liquid-salt coolant is a mixture of fluoride salts with freezing points near 400°C and atmospheric boiling points of

~1400°C. Several different salts can be used as the primary coolant, including lithium-beryllium and sodium-zirconium fluoride salts. Optimization studies to select the most promising salt are in progress and involve the assimilation of several considerations, including thermo-physical properties, material compatibilities, nuclear performance, toxicity, and cost. The reactor operates at near-atmospheric pressure, and at operating conditions, the liquid-salt heat-transfer properties are similar to those of water. Heat is transferred from the reactor core by the primary liquid-salt coolant to an intermediate heat-transfer loop. The intermediate heat-transfer loop uses a secondary liquid-salt coolant to move the heat to a thermochemical hydrogen (H_2) production facility or to a turbine hall to produce electricity. If electricity is produced, a multireheat nitrogen or helium Brayton power cycle (with or without bottoming steam cycle) is used. Figure 1.1 is a schematic of the plant system.

The reactor layout for the LS-VHTR is shown in Fig. 1.2. The 9.2-m-diam vessel is the same size as that used by the S-PRISM design; however, the LS-VHTR power output is 2400 MW(t) rather than 1000 MW(t) for S-PRISM. The LS-VHTR uses a passive reactor vessel auxiliary cooling system (RVACS) similar to that developed for decay heat removal in the sodium-cooled S-PRISM. The reactor and decay-heat-cooling system are located in a below-grade silo. The reactor decay heat is (1) transferred from the reactor core to the reactor vessel graphite reflector by natural circulation of the liquid salts, (2) conducted through the graphite reflector and reactor vessel wall, (3) transferred across an argon gap by radiation to a guard vessel, (4) conducted through the guard vessel, and then (5) removed from outside of the guard vessel by natural circulation of ambient air. There are no pumps, valves, or other active systems necessary for successful decay heat removal. Note also that the low pressure reactor vessel is enclosed by a guard vessel so that any coolant leaks from the reactor vessel will be contained by the guard vessel, making a loss-of-coolant accident nearly impossible. Therefore, the design basis accident for this reactor is a loss of flow accident.

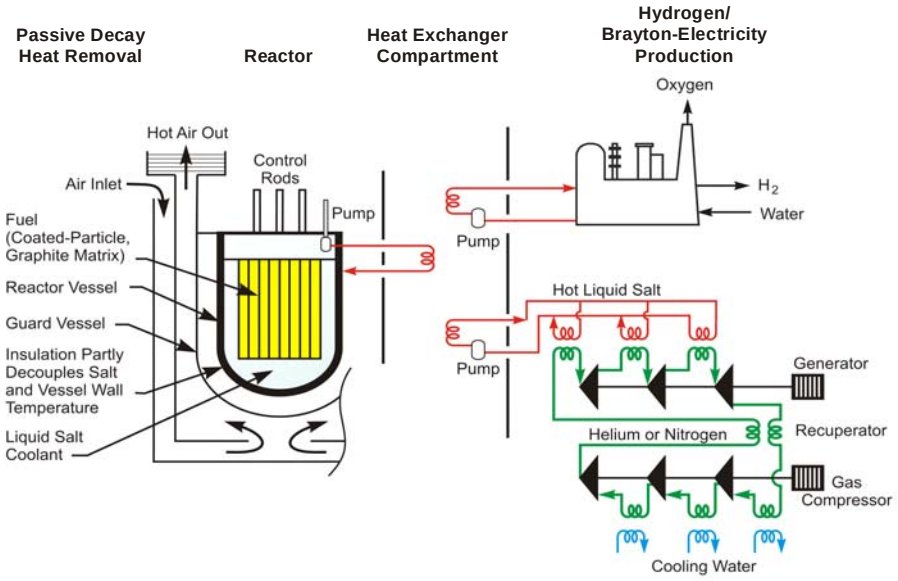

Fig. 1.1. Schematic of the LS-VHTR for cogeneration of electricity and hydrogen.

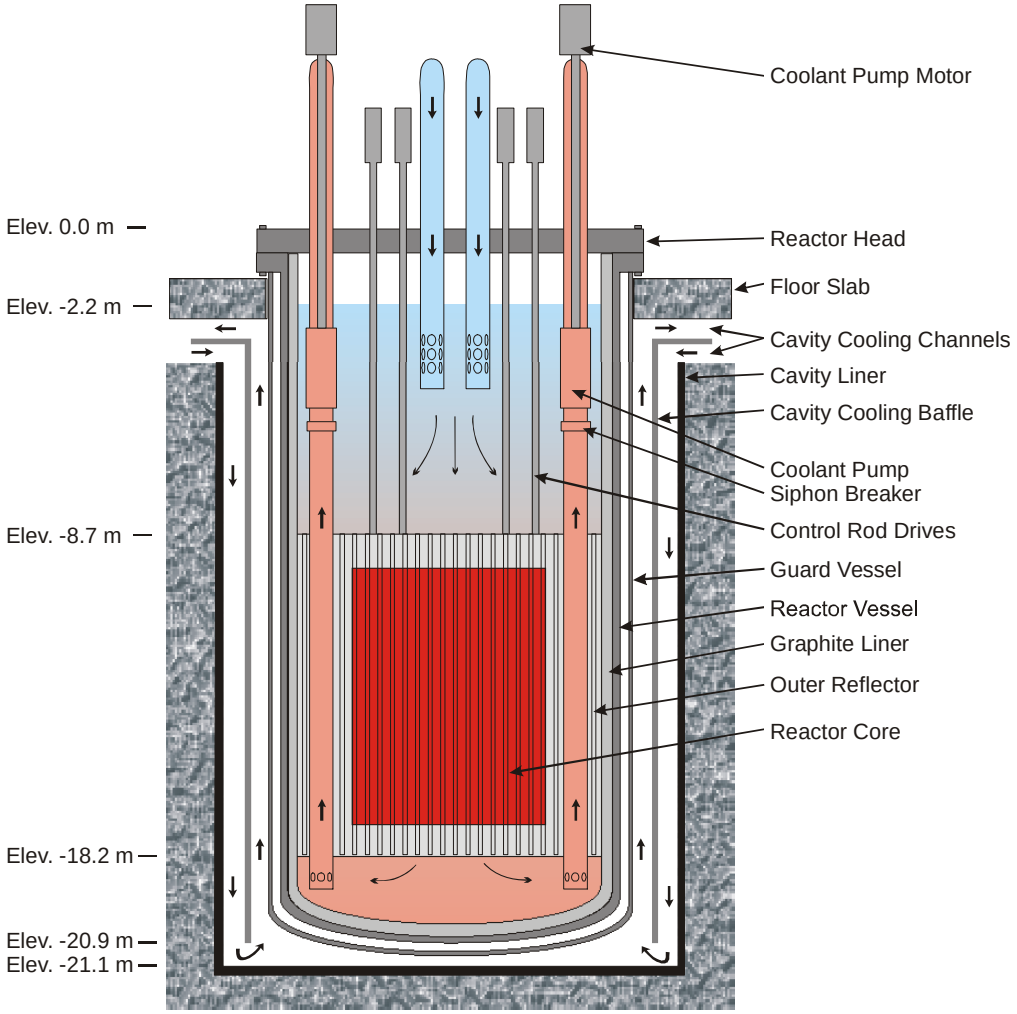

Fig. 1.2. Elevation view of baseline LS-VHTR reactor.

A preliminary physics viability study was completed in 2004 [Ingersoll, 2004]. The reactor core design for that initial study was very similar to that of the gas-cooled VHTR reactor: the same coated particle fuel, cylindrical compacts, and hexagonal graphite moderator blocks; similar fuel enrichment and compact loading; similar power density; and a similar annular core shape. The conclusions from the study were that there were no physics viability issues with the LS-VHTR, although there are substantial development and engineering challenges driven by the relatively high freeze temperature of salt coolant, and salt chemistry issues that might impact material compatibilities. The parametric physics analyses also indicated that the annular VHTR-like core design, which had been optimized for gas coolant, was far from optimal for liquid coolant.

Building on the success of the 2004 study, the 2005 effort for the LS-VHTR focused on developing a new baseline core design that is more optimized for liquid coolant and which satisfies the primary safety and fuel cycle targets. The first change was to remove the inner graphite reflector, which is present in a gas-cooled reactor to improve heat transfer from the core during a loss of forced circulation (LOFC) accident. A LOFC simulation for the LS-VHTR

showed that significant natural circulation of the liquid-salt coolant occurred during the transient and provided effective heat transfer to the vessel. Thus, the inner reflector is not required, and removing it improves the overall neutron economy of the LS-VHTR by reducing the neutron leakage from the core. The change also eliminates the problem of severe power peaking near the inner reflector-core interface as observed in the gas-cooled VHTR. Figure 1.3 compares the 2004 LS-VHTR core and reflector layout with the initial 2005 baseline design.

Figure 1.4 shows the baseline fuel block design used for this study. Several alternative designs were considered as part of the study, including changing the fuel and coolant channel diameters, the pitch between the channels, the number of fuel pins and coolant channels, and a more heterogeneous clustering of the fuel pins. Other core design features were studied, such as the number of radial rows of fuel blocks and the inclusion of burnable poisons (BPs). Options for using BPs included distributing them in the fuel, distributing them in the graphite blocks, using discrete BP pins, and distributing them in discrete axial layers of the core. Table 1.1 lists the initial design features and baseline assumptions used by all organizations participating in this study.

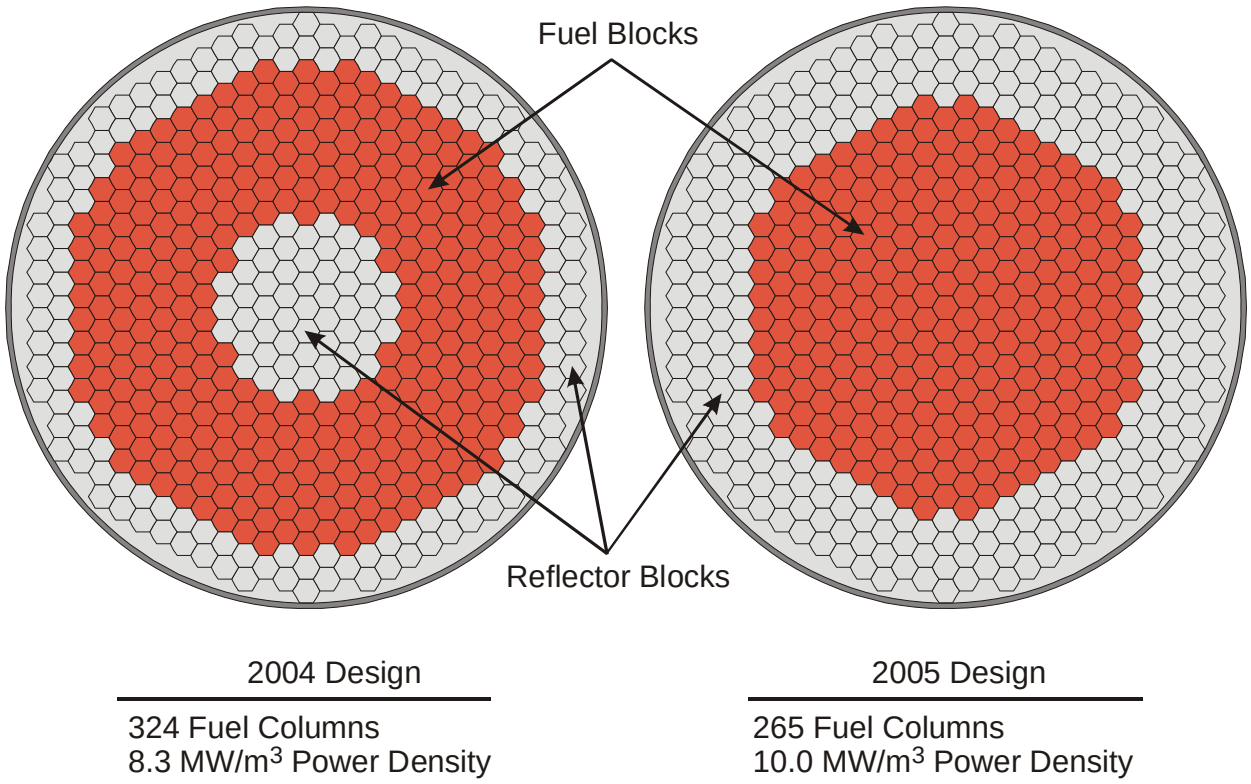

Fig. 1.3. LS-VHTR core and reflector pattern from 2004 study (left) and initial baseline 2005 design (right).

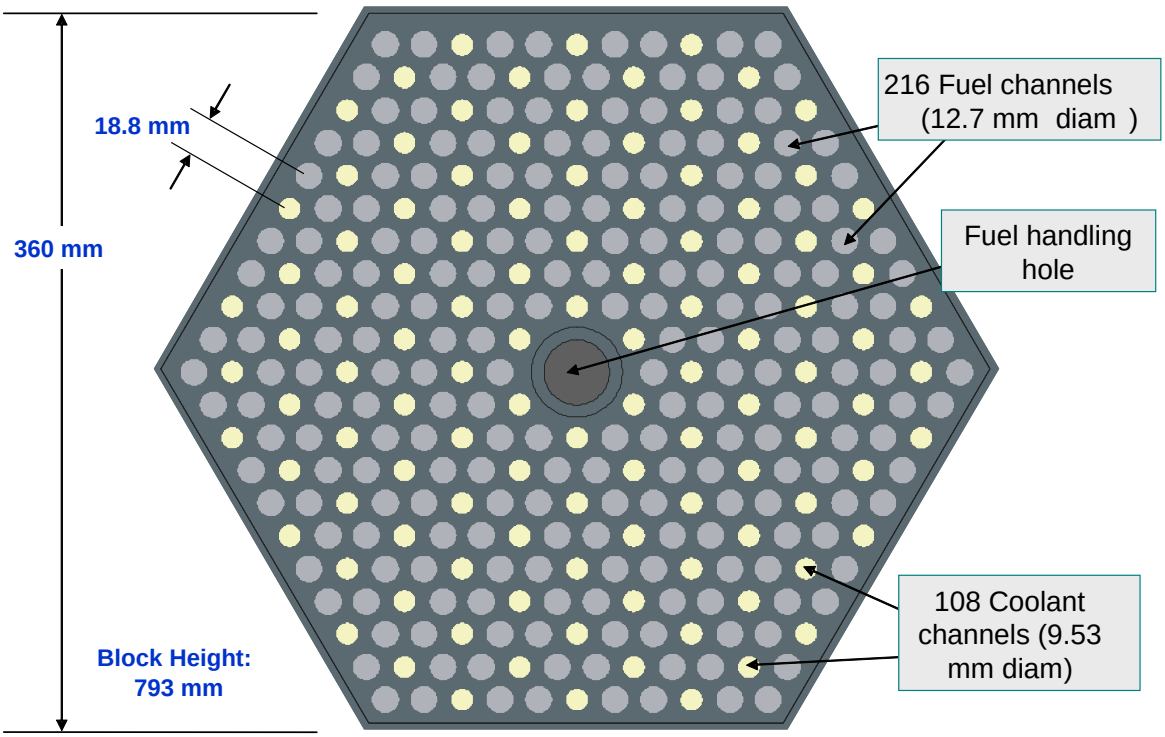

Fig. 1.4. Baseline LS-VHTR fuel block.

Table 1.1. Key parameters and targets for 2005 baseline LS-VHTR design

Parameter	Value	Parameter	Value
Total power output	2400 MW(t)	Discharge burnup	≥100 GWd/t
Coolant salt	^{2}LiF-BeF_2	Fuel element:	
^{7}Li isotopic concentration	99.995%	– Graphite density	1.74 g/cm^3
Outlet coolant temperature	1000°C	– Diameter (across flats)	36.0 cm
Inlet coolant temperature	≥850°C	– Height	79.3 cm
Reactor vessel diameter	9.2 m	– Fuel channel diameter	1.27 cm
Fuel kernel composition	$U_{1.0}C_{0.5}O_{1.5}$	– Number of fuel channels	216
Fuel kernel diameter	425 μm	– Coolant channel diameter	0.953 cm
Particle diameter	845 μm	– Number of coolant channels	108
Fuel kernel density	10.5 g/cm^3	– Pitch between channels	1.88 cm
^{235}U enrichment	≤20%	Power density	10.0 MW/m^3
Particle packing fraction	≤30 vol %	Number of fuel columns	265
Fuel cycle length	≥18 months	Number of fuel blocks per column	10

It was determined in the 2004 study that the neutronic performance of the core, especially the reactivity response of the core to voiding of the liquid coolant, was highly dependent on the isotopic and elemental composition of the salt and to the core composition and geometry. A large number of material and design options were identified that needed to be considered in achieving an optimized core configuration. It was clear that a more systematic approach would be needed to sort through the numerous trade-offs, which became the planning basis for the 2005 design effort. A parallel task in 2005 was established to evaluate and compare thermo-physical properties and chemical behaviors of several candidate salts for this application [Williams, 2005a and 2005b]; therefore it was decided that the present design study would use a single salt composition, $^{2}LiF\text{-}BeF_2$, and focus on characterizing the performance of the core relative to other design options. The baseline salt, referred to as "Flibe," has been used in previous nuclear applications [Weinberg, 1970] and was also judged to be the most neutronically favorable of the candidate salts. Once a core design using Flibe is developed with acceptable operational and safety performance, alternative salts can be evaluated relative to the Flibe performance.

1.2 OVERVIEW OF REPORT

Several organizations were involved in the present LS-VHTR study. These include: Oak Ridge National Laboratory (ORNL), Idaho National Laboratory (INL), and Argonne National Laboratory (ANL). The roles of the three organizations were interrelated and somewhat overlapping in order to provide some independent verification of results. Generally, the organizational roles were:

- INL focused on safety analyses, including the power removed from the vessel by the RVACS and the response of the reactor to a LOFC transient. They also investigated core power distributions and the impact of design variations on core reactivity.
- ANL investigated fuel assembly performance such as the particle fuel double heterogeneity effect and fuel/moderator/coolant geometries. Additionally, they looked at fuel cycle issues such as enrichment, discharge burnup and fuel cycle length, and whole-core parameters such as core size and power density.
- ORNL provided overall coordination and focused on reducing the coolant void reactivity through the use of alternate geometries and material compositions.

In general, each of the organizations used a different set of computational tools and data sets, which are discussed in Sect. 2 organized by laboratory. The remaining sections are organized by topic and integrate results from all participants who contributed to the specific topic. Section 3 presents results from various whole-core analyses and Sect. 4 presents data and several analyses related specifically to the use of Flibe coolant. The neutronics performance of the baseline core is presented in Sect. 5, including several parametric studies for design variations that impact the core's response to voiding of the coolant. The thermal-hydraulic and safety performance of the reactor is presented in Sect. 6. Finally, Sect. 7 gives a summary of results, a revised LS-VHTR design, and a discussion of future activities.

2. ANALYSIS TOOLS

Each of the organizations involved in this study used an extensive set of computational tools and nuclear or material property data libraries. These are described in the following sections.

2.1 ORNL METHODS AND DATA

The physics analysis at ORNL was performed with tools contained within the SCALE5.1 [ORNL, 2004] system. The SCALE system consists of data libraries, cross-section processing codes, radiation transport codes, and fuel depletion and activation routines that are used in a modular manner to perform comprehensive reactor analyses. The lattice physics and core calculations were performed using the TRITON depletion sequence, which combines the BONAMI/CENTRM resonance processing, the NEWT or KENO-VI neutron transport, and the ORIGEN-S depletion and activation tools.

All analyses were performed with a 238-group Evaluated Nuclear Data Files Versin 6 (ENDF/B-VI) cross-section library that was processed with AMPX. The resonance processing procedure uses the Bondarenko methodology (BONAMI) for the unresolved resonance region and a continuous energy methodology for the resolved resonance region (CENTRM). The CENTRM resonance processing tool performs a near-continuous energy (pointwise), one-dimensional, discrete-ordinates (S_8, P_3) transport calculation for each pin-cell type in the problem. This leads to a highly accurate, problem-dependent flux spectrum incorporating resonance interference effects that is used as a weighting function for the near-continuous energy cross sections from ENDF/B-VI to create a problem-dependent 238-group cross-section library using the PMC code.

Recent additions to TRITON include the ability to perform resonance processing of cross sections for doubly heterogeneous fuel. This utilizes two CENTRM/PMC calculations in series: (1) to determine the spectrum of a particle and weight the particle cross sections, then (2) to determine the spectrum in the compact/pebble and re-weight the cross sections accordingly. This is necessary for a proper analysis of the multiplication factor (k_{inf}) in the LS-VHTR, which utilizes particle fuel within compacts. However, the reactivity change due to voiding proved insensitive to the double heterogeneity of the fuel; so many calculations within the study did not utilize this more complex option.

Two transport methods are available within TRITON: KENO-VI and NEWT. KENO-VI is a three-dimensional, multigroup stochastic transport code that was recently added to the TRITON depletion sequence. Three-dimensional analyses of the full LS-VHTR core were performed using KENO-VI along with many of the other three-dimensional analyses, such as the parfait core design. The two-dimensional analyses were performed using NEWT, a two-dimensional, multigroup deterministic transport code that was originally developed for use in TRITON. It utilizes Extended Step-Characteristics (ESC) discretization to solve the characteristics form of the transport equation on an arbitrary polygonal mesh.

To better support the analysis of the LS-VHTR geometry, a hexagonal array option was added into NEWT. This required several changes to the Coarse-Mesh Finite-Difference acceleration algorithm but proved to be a very useful tool for calculating the two-dimensional effects of BPs and geometry distributions within a fuel block. Because of the acceleration of the

deterministic transport solution, the NEWT calculations only required a few minutes of CPU time.

The TRITON depletion sequence utilizes the ORIGEN-S module to calculate fuel depletion, actinide transmutation, fission product buildup and decay, and associated radiation source terms. This tool was necessary for both the activation/transmutation of the salt coolant options and the dependence of the reactivity change due to coolant voiding on fuel burnup. Branch calculations were performed using TRITON to determine the change in the multiplication factor due to voiding as a function of fuel depletion for every time-step in the depletion sequence.

2.2 ANL METHODS AND DATA

The calculations done for this study mostly used the lattice codes WIMS8 [AEA, 1999] and DRAGON [Marleau, 1998] and the linear reactivity model (LRM) [Driscoll, 1990] to represent the LS-VHTR core. WIMS8 and DRAGON allow treatment of the double heterogeneity effect of the coated-fuel particles in the graphite matrix during assembly-level calculations. Prior to the final calculations, the performance of the codes were evaluated by comparing the code results with those obtained using the Monte Carlo code MCNP4C [LANL, 1993].

The WIMS8 code provides an extensive software package for neutronics calculations. The code employs an open structure that permits the linking of various methods to create computational schemes for a given thermal reactor design. These can range from simple homogeneous cells to complex whole-core calculations. Most generally, however, the lattice capabilities of the code are used for reactor analysis. Geometries are available for analyzing PWR, BWR, VVER, AGR, RBMK, CANDU, other reactor core designs, storage pools, and experiments.

Methods for the neutron flux solution in WIMS8 include collision probability (1-D or 2-D), method of characteristics, S_n method (1-D or 2-D), diffusion theory, and hybrid methods. The code also provides an integrated Monte Carlo method (MONK) for the purpose of internal validation. WIMS8 is supplied with 69- and 172-group cross-section libraries based on the validated JEF2.2 nuclear data. It is noted that the WIMS8 code has the PROCOL module that provides a capability for calculating the collision probabilities of particulate fuel in an annular geometry that could be used in flux solvers to model the double heterogeneity effect of that fuel form.

The DRAGON code has a collection of models for simulating the neutronic behavior of a unit cell or a fuel lattice in a nuclear reactor. The typical functionalities found in most modern lattice codes are contained in DRAGON. These include interpolation of microscopic cross sections supplied by means of standard libraries; resonance self-shielding calculations in multidimensional geometries; multigroup and multidimensional neutron flux calculations which can take into account neutron leakage; transport-transport or transport-diffusion equivalence calculations; and modules for editing condensed and homogenized nuclear properties for reactor calculations.

The current version of the code contains three algorithms for the solution of the integral transport equation, ranging from a simple collision probability method coupled with the interface current method to the full collision probability method. The code also performs isotopic depletion calculations. At ANL, the 69- and 172-group cross section libraries created in WIMSD4-format by the Reduced Enrichment for Research and Test Reactors (RERTR) project

are used with the DRAGON code. The depletion chains and types of fission products to be tracked by the code are obtained from the cross-section library used. For the DRAGON calculations, cross-section data for the heavy nuclides are tabulated at different temperatures (2–4 points), and all the heavy nuclides contained in the library are treated as resonance materials.

An attractive feature of the DRAGON code is its ability to treat particle fuel in a graphite matrix in a full-assembly calculation. This capability has been used for modeling the fuel assemblies of block-type, high-temperature gas-cooled thermal reactors and the pebble elements in alternative pebble-bed concepts.

It is noted that in the DRAGON full-assembly model for very high-temperature reactors (VHTRs) hexagonal block, the block is formed by a collection of pin-cell-sized hexagons. Each pin-cell contains the fuel compact and its surrounding block graphite. When all the fuel and coolant-hole pin-cells are represented, the block graphite content is not totally accounted for and, therefore, an extra ring of pin-cell-sized hexagons is used to represent the remaining graphite. The number density of the graphite in these peripheral cells is modified to preserve the graphite content of the assembly block. Due to the use of the pin-cell-sized hexagons, the DRAGON assembly model has jagged boundaries, not the flat boundaries of the hexagonal block.

A distinction between the DRAGON and WIMS8 models for the VHTR assembly is that the WIMS8 code does not provide the particle-fuel double heterogeneity treatment at the assembly level like DRAGON. A two-step scheme is, therefore, utilized in the WIMS8 calculation. In the first step, the PROCOL module is used for detailed treatment of the double heterogeneity at the pin-cell level; other items, such as Doppler and resonance treatments are considered. A super-cell calculation is performed at this stage. The super-cell model is prepared by converting the hexagonal unit pin-cell to an equivalent annular cell and introducing an extra region representing a fraction of the graphite block outside the fuel cells. The fraction is determined such that the graphite volume in the super-cell is equal to the ratio of the graphite block volume to the number of fuel cells. The result of the pin-cell calculation is homogenized fuel pin-cell cross sections. These cross sections are then used in the second step, which embodies the full-assembly calculation. Besides the homogenized geometry of the fuel pin-cell, the detailed geometries of the other cells are retained in the assembly calculation. The full-assembly calculation is performed using the CACTUS module of the WIMS8 code. A schematic of the two-step procedure is provided in Fig. 2.1.

The LRM assumes that the core reactivity behavior with burnup (k_{eff} let-down) is linear and can be predicted using a series of unit assembly calculations. The approach is particularly useful for estimating the enrichment requirements and fuel compositions with burnup. In this regard, estimates of the required fuel enrichment can be obtained for the critical burnup states. The relationship between the core critical burnup (B_c) and the assembly discharge burnup (B_d) is

$$B_c = \frac{n+1}{2n} B_d , \tag{1}$$

where *n* denotes the number of fuel management batches. In a three-batch core with a cycle burnup of 33.3 GWd/t, the discharge burnup is 100 GWd/t, and according to Eq. (1), the critical burnup is 66.67 GWd/t.

The LRM cannot, however, be used for accurately estimating the core power peaks. The key assumption of the model was verified by comparing the multiplication factor variation with

burnup of a unit fuel element (assembly) calculation to that of a whole-core calculation, and the core leakage impact on the reactivity was estimated.

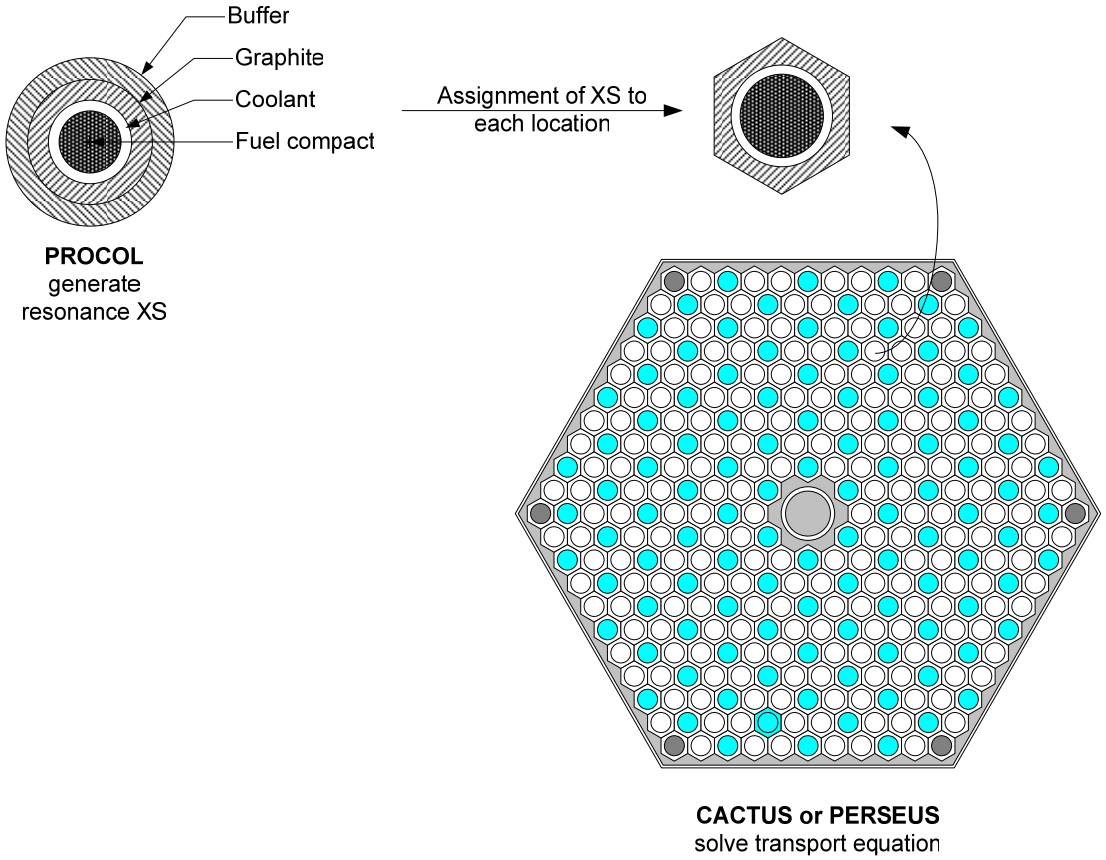

Fig. 2.1. WIMS8 procedure for VHTR full-assembly calculation.

2.3 INL METHODS AND DATA

The Monte Carlo N-Particle code Version 5 (MCNP5) was used in the INL neutronic calculations [LANL, 2004]. This code is a general purpose, continuous energy, generalized geometry, coupled neutron-photon-electron Monte Carlo transport code and is well-known and widely used worldwide. The geometry capability allows for very explicit, three-dimensional representations of the reactor core details, allowing for detailed representation of a partial- or full-reactor core. The code also has the ability to accurately calculate many reactor core physics parameters, such as the core k-effective, control rod worth, neutron flux, neutron spectrum, nuclear reaction rate, and group cross sections.

The continuous-energy neutron cross sections typically range from 10^{-5} eV to 20 MeV. The photon energy range is from 1 keV to 100 MeV, and the electron energy is from 1 keV to 1,000 MeV. A wide variety of nuclide cross-section and reaction data are available from the Evaluated Nuclear Data Files Version 5 and 6 (ENDF/B-V and ENDF/B-VI). The LS-VHTR model used predominantly ENDF/B-VI data. In addition, MCNP temperature-dependent cross sections at high temperatures have recently been generated over the temperature range of 1000 to 2200°C for application with the prismatic VHTR. The 1100°C data libraries were used in the neutronic calculations for the fuel temperature.

Because the MCNP computer code is a Monte Carlo code, the calculated results are reported by the code with an associated statistical uncertainty or relative error. The relative errors translate into one-sigma statistical uncertainty values by multiplication of the relative error and the calculated result. Two-sigma and three-sigma confidence intervals are obtained by further multiplying the one-sigma values by a factor of 2 and 3, respectively. The confidence levels associated with one-, two-, and three-sigma values are 68.3, 95.4, and 99.7%, respectively. All calculated results reported here had three-sigma statistical errors less than the size of the plot symbol.

The RELAP5-3D computer program [INEEL, 2003] was used to model the LS-VHTR for the safety analyses. The program was originally developed for thermal-hydraulic analysis of light-water reactors and related experimental systems during loss-of-coolant accidents and operational transients. The code has recently been improved to simulate candidate Generation IV designs cooled by gas [Davis, 2005a], supercritical water [MacDonald, 2005], and lead-bismuth [MacDonald, 2002]. Thermo-physical properties of liquid-salt coolants have also been implemented into the code [Davis, 2005b], which allows it to simulate the LS-VHTR.

This page intentionally blank

3. REACTOR CORE CHARACTERIZATION

3.1 LATTICE CODE VALIDATION

A previous study had been performed to evaluate the performance of the WIMS8 and DRAGON code models for the analysis of the helium-cooled VHTR [Kim, 2004b]. The study demonstrated that the codes are capable of calculating lattice parameters of interest very accurately compared to Monte Carlo reference solutions in the range of interest. While the helium-cooled VHTR and the liquid-salt-cooled VHTR employ similar assembly designs, the different characteristics of the coolants suggested the need for further verification of the performance of the lattice codes.

The performances of the deterministic lattice codes WIMS8 and DRAGON for analyzing the LS-VHTR fuel element were evaluated by comparing results from the codes to those from the Monte Carlo code MCNP4C. The MCNP4C calculations for the fuel assembly were performed using the ENDF/B-VI nuclear data library distributed with the code. The calculations were for the cold state (293 K) and have been performed without S(α,β) data for the light nuclides in the liquid-salt coolant because the data do not exist currently in both the MCNP4C and the deterministic codes. In the WIMS8 and DRAGON calculations, the 172-group transport equations were solved.

In this study, the packing fraction, uranium enrichment, and coolant-hole diameter are 25%, 10%, and 0.953 cm respectively; the values suggested for the reference LS-VHTR design. A lithium-enrichment value of 99.995% was used. Results from the study are summarized in Tables 3.1 and 3.2. In addition to the traditional element eigenvalue, an estimate of the double heterogeneity effect was also obtained. This effect was determined by taking the difference in the multiplication factor (k_{inf}) values derived from calculations using the spatially heterogeneous and homogeneous compact models. In the heterogeneous model the coated-fuel particles are explicitly represented in the compact. In the homogeneous model, the compositions of the coated-fuel particles are smeared with those of the graphite matrix using volume weighting. In the latter model, the self-shielding effect of the fuel at the particle level is not represented.

Table 3.1 summarizes the eigenvalues calculated by the WIMS8 and DRAGON lattice codes and the MCNP4C Monte-Carlo code. The WIMS8 and DRAGON codes calculated fuel element k_{inf} values that are within 100 and 200 percent milli (pcm), respectively, of those from MCNP4C calculations. The reactivity differences were computed using $\Delta\rho = \Delta k/k_1k_2$. Components of these differences come from the different nuclear data files used in the calculations (e.g., JEF2.2 for WIMS8). These differences are similar to those observed during the Next Generation Nuclear Plant (NGNP) sensitivity study performed in FY 2004 [Kim, 2004b].

The deterministic and Monte Carlo codes predicted very similar values for the double heterogeneity effect in the LS-VHTR fuel element (difference in k_{inf} from calculations using the smeared and explicit heterogeneous fuel compact models). The MCNP4C calculation predicted a value of 2.6% $\Delta\rho$, and the two lattice codes give a deviation of about 0.1% $\Delta\rho$ for these cases (see Table 3.2). These are surprisingly small differences. For comparison, an earlier MCNP4C calculation for the helium-cooled VHTR fuel element gave a value of 2.3% $\Delta\rho$ for the double heterogeneous effect.

Table 3.1. Comparison of k_{inf} values for fuel element at cold state

Compact model	Code	Eigenvalue	Difference from reference (pcm Δρ)
Heterogeneous	MCNP4C	1.53861 ± 0.00067[a]	Reference
	WIMS8	1.53756	–44
	DRAGON	1.53832	–12
Homogeneous	MCNP4C	1.47886 ± 0.00075	Reference
	WIMS8	1.47681	–94
	DRAGON	1.48216	151

[a] 1.53867 ± 0.00075 with MCNP5.

Table 3.2. Double heterogeneity effect (Δρ)

Code	Double heterogeneity effect (%Δρ)
MCNP4C	2.6
WIMS8	2.7
DRAGON	2.5

3.2 DISCHARGE BURNUP AND URANIUM ENRICHMENT

Parametric studies were performed for the LS-VHTR in order to ensure that the constraint on the fuel enrichment will be met for an assumed target cycle length of 18 months and target discharge burnup greater than 100 GWd/t, similarly to those used in recent helium-cooled VHTR studies [Kim, 2004]. The linear reactivity model discussed in Sect. 2.2 was used for the study. In this study, the plant capacity factor and lithium enrichment were assumed to be 90 and 99.995% ^{7}Li, respectively. The fuel kernel diameter was fixed as 425 μm.

First, the cycle length and discharge burnup were evaluated as a function of uranium enrichment, packing fraction, lithium enrichment, and number of batches. Results are summarized in Table 3.3. The cycle lengths obtained for the single-batch cases are plotted in Fig. 3.1.

The overall trends of the LS-VHTR are similar to those for the helium-cooled VHTR: the cycle length increases with uranium enrichment and packing fraction, and the optimum packing fraction was observed around 25% (see Fig. 3.1). Additionally, the discharge burnup increases with an increase in the number of batches, but the cycle length decreases. The cycle length is observed to increase with an increase in lithium enrichment; increasing the lithium enrichment from 99.99 to 99.995% results in an increase of the cycle length by 12 EFPD (~1.9%).

Table 3.3. Cycle length and discharge burnup (1.5% Δk leakage approximation)

Uranium enrichment (%)	Lithium enrichment (%)	Packing fraction	Specific power density (W/g HM)	Single batch		Three batch	
				Cycle length (EFPD)	Discharge burnup (GWd/t)	Cycle length (EFPD)	Discharge burnup (GWd/t)
10.0	99.995	0.10	396	200	79	100	120
		0.20	198	422	83	211	127
		0.30	132	472	62	236	96
15.0	99.995	0.10	396	313	124	156	187
		0.20	198	644	127	322	194
		0.30	132	731	96	366	148
	99.990	0.20	198	632	125	316	188
20.0	99.995	0.10	396	420	166	210	251
		0.20	198	853	169	427	256
		0.30	132	983	130	492	198

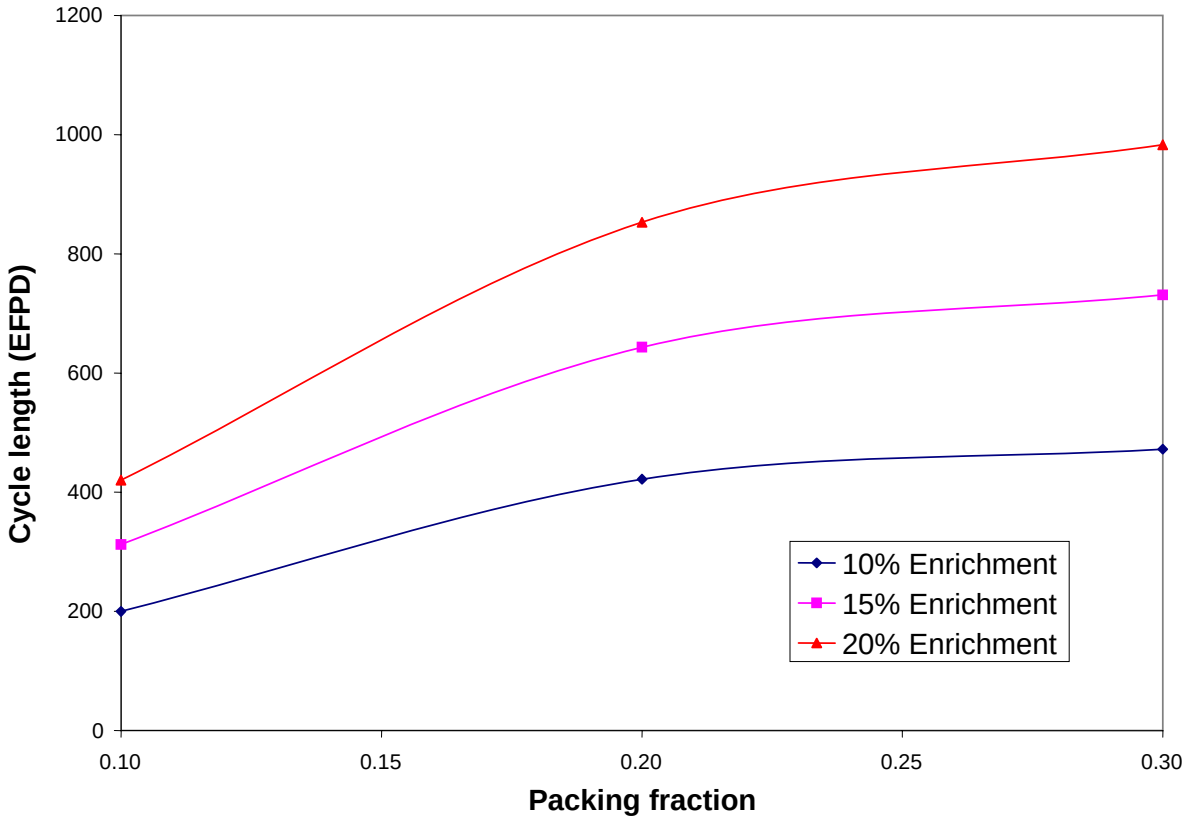

Fig. 3.1. Single batch cycle length as function of packing fraction and uranium enrichment.

The cycle length of the LS-VHTR as a function of the fuel management scheme (i.e., number of batches) and uranium enrichment are plotted in Fig. 3.2. Generally, the cycle length increases as the uranium enrichment increases, but decreases with an increase in the batch size. To utilize the uranium resources effectively, a high-discharge burnup is desirable. By increasing the batch size, it is possible to increase the discharge burnup; however, the cycle length could become smaller than the target cycle length. In this study, the target cycle length is assumed to be 18 months. The required uranium enrichment to obtain the target cycle length and the corresponding discharge burnup were estimated using the data in Fig. 3.2, and the results are provided in Table 3.4. In the calculations, the plant capacity factor and the core power density were assumed to be 90% and 10.2 MW/m^3, respectively. Also, a lithium enrichment of 99.995% was used.

The results in Table 3.4 indicate that the required enrichment and discharge burnup increase with the number of batches. The target cycle length can be obtained by adjusting the uranium enrichment in the single-, two- and three-batch schemes. Although the three-batch scheme appears to require an enrichment that is slightly greater than the 20% limit that is imposed by proliferation concerns, it is likely that further optimization of the core could result in acceptable enrichment for even the three-batch case. The required enrichment is smallest for the one-batch case, but its discharge burnup is smaller than the target value. Therefore, the two-batch scheme is desirable to satisfy simultaneously the target cycle length and discharge burnup and the constraint on the fuel enrichment.

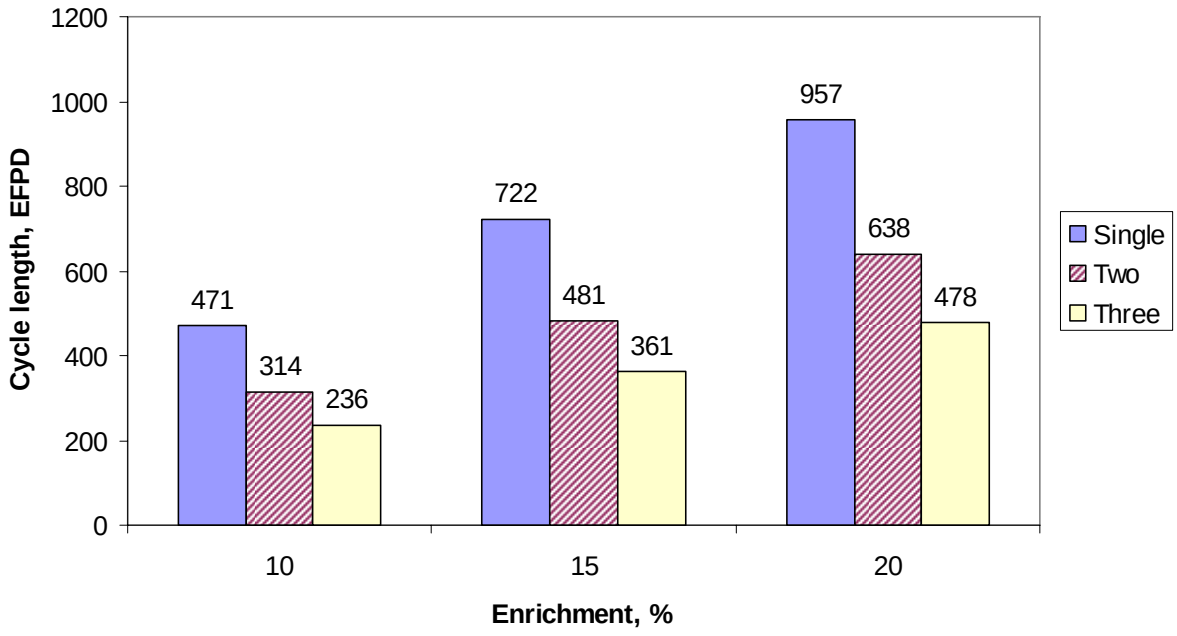

Fig. 3.2. Comparison of cycle lengths as function of uranium enrichment and fuel management scheme.

Table 3.4. Uranium enrichment and discharge burnup for 18-month cycle length

Fuel management scheme	Single batch	Two batch	Three batch
Uranium enrichment, %	10.4	15.3	20.6
Average discharge burnup, GWd/t	78	156	234

3.3 POWER DISTRIBUTION

Radial power distributions were generated using the MCNP code and an explicit 1/12-core model for both a 10-ring and a 9-ring core layout. The distributions were needed to support the thermal-hydraulic and safety analyses discussed in Sect. 6. An MCNP fission tally was defined for each of the fuel rods in every fuel block in all active core rings. An average block power was then estimated from the sum-average of all the fuel rod fission tallies in a given block. Figures 3.3 and 3.4 show the calculated radial peak-to-average fission power profiles for the 10- and 9-ring LS-VHTR core designs, respectively. On each figure are two curves—the lower curve is the radial peak-to-average fission power for a single block in each ring, which is useful for understanding the relative fuel rod power peaking across the core, and the upper curve is the radial peak-to-average fission power for the full core in which the ring average is weighted by the number of blocks in each ring. This latter curve is designated as the "core" curve in these figures and is the profile used for the thermal-hydraulic calculations described in Sect. 6.

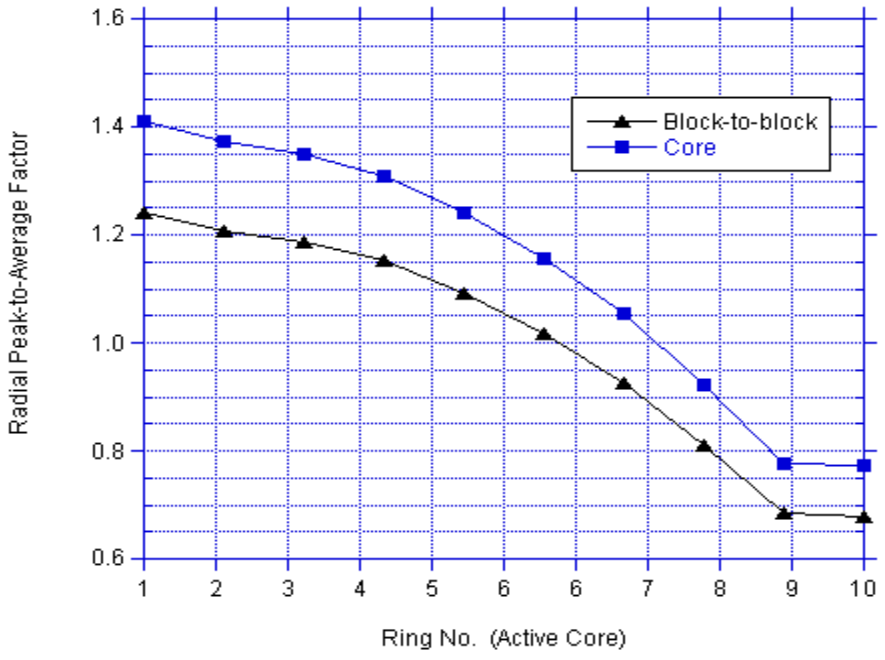

Fig. 3.3. Radial power profiles for the 10-ring LS-VHTR core.

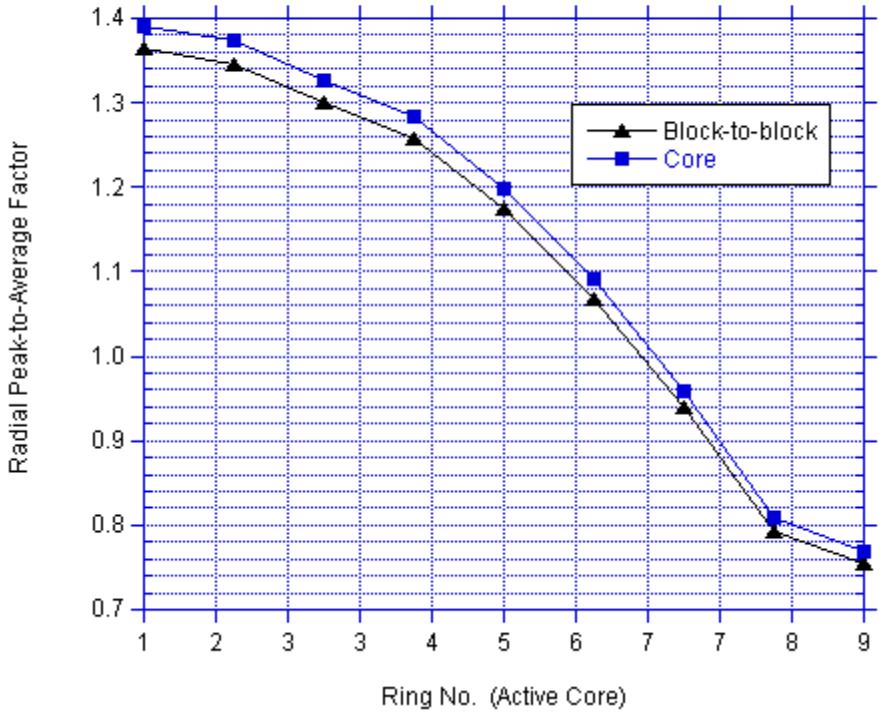

Fig. 3.4. Radial power profiles for the 9-ring LS-VHTR core.

In the case of the 10-ring LS-VHTR core design, the peak-to-average is approximately 1.4 with the radial core power split (50:50) boundary occurring between rings 7 and 8, or almost at the exact middle of ring 7. This means that half the core power is developed in rings 1 through 7.5 and the other half generated in rings 7.5 to 10. This power split seems somewhat lopsided until one considers the relatively large number of fuel blocks in rows 8, 9, and 10, representing about 40% of the total fuel volume.

Note also the comparable power levels of rings 9 and 10. This is indicative of significant fuel rod power-peaking in ring 10, and in particular the fuel rods (rows 1–5) adjacent to the outer graphite reflector where the reflected thermal neutron flux from the reflector is relatively large. Maximum power-peaking factors are approximately 2.0 for these fuel rods. Power-peaking mitigation would need to be implemented in an optimal LS-VHTR core design through grading of the particle packing fraction and the use of BP rods.

3.4 POWER DENSITY AND FUEL MANAGEMENT

The better heat transfer property of the Flibe liquid-salt coolant compared to the helium coolant is a reason why a solid cylindrical core configuration is being considered for the LS-VHTR. A solid core is attractive since it allows the increase of the core power level at a fixed power density and, hence, the potential for better plant economy relative to an annular core design. The good thermal properties of Flibe also provide an opportunity to increase the power

density. The power density of the baseline LS-VHTR is about 50% higher than that of the helium-cooled VHTR (10.2 vs 6.6 MW/m^3). The increase in power density for a fixed power level improves the economy by reducing the reactor size, but it increases the fuel depletion rate and thus reduces the cycle length for a fixed fuel loading. A neutronic sensitivity study was performed to determine the maximum power density of the LS-VHTR that meets the cycle length and discharge burnup goals within the constraints on uranium enrichment (<20%), though core thermal and safety performance will also impact the final value as discussed in Sect. 6.

Various power densities were obtained by changing the total number of fuel columns. The power densities evaluated in this study were obtained by decreasing the number of fuel rings from 10 (reference value) to 8 rings. The numbers of fuel columns in the cases with 10, 9, and 8 rings are 265, 211, and 169, respectively; note that for cases in which all the rings have no vacancies, the total number of columns in the core is 3N(N-1)+1, where N is the number of rings. The cases with 10 and 9 rings are assumed to have six vacant fuel columns (see Fig. 1.1 for the 10-ring case). Note that in the sensitivity calculations performed for this work, it is assumed that all core columns contain fuel elements only (i.e., no control elements have been modeled). Additionally, the lithium enrichment and packing fraction are assumed to be 99.995 and 25%, respectively.

The linear reactivity model discussed in Sect. 2.2 was used in the study. The targeted cycle length for the study is 18 months. The WIMS8 model developed for the reference core was modified to reflect the change in the specific power (power density) level resulting from the decrease of the fuel loading (fuel elements). With this new specific power, the WIMS8 code was used to determine the enrichment that gives a cycle length of 18 months.

The results of the maximum power density study are provided in Table 3.5. For the purpose of comparison, the results for the two-batch helium-cooled VHTR core having a power level of 600 MW(t) and a power density of 6.6 MW/m^3 is included in the table. The results indicate that a higher enrichment is required to increase the power density of the LS-VHTR from the reference value of 10.2 MW/m^3. The constraint on the fuel enrichment (less than 20% for proliferation reasons) and the targeted discharge burnup (greater than 100 GWd/t) define the neutronic bounds for the acceptable power density.

Table 3.5. Sensitivity results of maximum power density

Parameter		VHTR	LS-VHTR		
Power, MW(t)		600	2400		
Total number of fuel columns		102	265[a]	211	169
Power density, MW/m^3		6.6	10.2	12.8	15.9
Specific power density, MW/t		103	158	199	248
Single-batch	Enrichment, %		10.4	13.0	16.3
	Burnup, GWd/t		78	98	122
Two-batch	Enrichment, %	14.0	15.3	19.5	24.7
	Burnup, GWd/t	100	156	196	244
Three-batch	Enrichment, %		20.6	26.2	33.1
	Burnup, GWd/t		234	293	366

[a]Baseline LS-VHTR core model.

With the single-batch fuel management scheme, only the case with a power density of 15.9 MW/m^3 (of the three cases evaluated) meets the targeted cycle length and discharge burnup and the constraint on the enrichment simultaneously. With the use of higher number of batches, the discharge burnup is greater than 100 GWd/t for all the cases. However, the enrichment limit is met only for the two-batch fuel management cases using power densities of 10.2 MW/m^3 (reference) and 12.8 MW/m^3. Using a higher number of batches or power density results in a higher enrichment requirement. It is noted that discrete values of power densities have been used in this study, and that a more detailed study would be required to determine the exact boundaries of the design space that meets the core design requirements and constraints. However, higher power densities have not been considered because preliminary thermal and safety calculations indicate that it would be difficult to retain the passive safety attributes of the core with a much higher power density than the reference value. Also, there is some evidence that the integrity of the coated particle fuel may not be ensured for a power density above 10 MW/m^3.

Taken as a whole, the results show that neutronically, the reference power density can be increased by over 50% (from 10.2 to 15.9 MW/m^3) when the single-batch fuel management scheme is employed. This is equivalent to 2.4 times the value for the helium-cooled VHTR design but may be constrained by fuel performance. Increasing the number of batches is detrimental because of the increase in the enrichment requirement (could be more than 20%).

It is also important to notice in Table 3.5 that the baseline LS-VHTR core yields a 50% higher burnup than the VHTR with a similar fuel enrichment. This is due to the better neutron economy in the large 2400 MW(t) LS-VHTR core resulting from reduced neutron leakage. This translates to 30% lower fuel cycle costs and reduced waste volume relative to the gas-cooled VHTR.

3.5 CONCLUSIONS FROM CORE CHARACTERIZATION

The cycle length and discharge burnup were evaluated as a function of uranium enrichment, packing fraction, lithium-enrichment, and number of batches. The overall trends of these parameters for the LS-VHTR were found similar to those of the helium-cooled VHTR: the cycle length increases with uranium enrichment and packing fraction, and the optimum packing fraction was observed to be around 25%. The cycle length increases slightly when the lithium-enrichment is increased from 99.99 to 99.995%.

The required uranium enrichment to obtain the target cycle length (18 months) and the corresponding discharge burnup were determined from parametric studies. The results indicate that the required uranium enrichment and discharge burnup increase with the number of batches. The three-batch scheme is, however, impractical because the required uranium enrichment is greater than 20%, which is precluded because of proliferation concerns. The required enrichment is smallest for the one-batch fuel management scheme, but its discharge burnup is smaller than the target value (100 GWd/t). Therefore, the two-batch scheme is desirable to satisfy simultaneously the target cycle length and discharge burnup and the enrichment (similar conclusion was obtained in the helium-cooled VHTR study).

The power distribution across the core was studied for both the baseline 10-row core layout and a reduced 9-row layout. The peak-to-average power peaking is approximately 1.4, which can be reduced by coated-particle packing fraction or enrichment grading. Significant power

peaking in the outer fuel pin rows of the outer most fuel blocks (adjacent to the outer reflector) was also observed. Maximum power peaking factors were approximately 2.0 for these rods.

The maximum power density of the LS-VHTR was investigated for the single-, two-, and three-batch schemes. A higher enrichment is necessary to increase the power density of the LS-VHTR. To increase the power density to 150% of the reference core, the required uranium enrichment is less than 20% in the single-batch fuel management scheme, while it is impractical to increase the power density to this level in the two- or three-batch schemes because the enrichment would exceed 20%. Finally, the fuel cycle costs may be as much as 30% lower than the helium-cooled VHTR because of the higher burnup that can be achieved with the improved neutron economy of a large core.

This page intentionally blank

4. COOLANT CHARACTERIZATION

Like helium in the VHTR, the effect of the coolant on the core physics of the LS-VHTR is relatively small. First, because of the excellent thermal properties of salt, the coolant fraction in the core can be quite small—less than 7% for the baseline LS-VHTR design. Second, the reference salt option, Flibe, has very small neutron cross sections, which makes it relatively transparent to neutrons. However, other salts that are not as good as Flibe neutronically are available and may have thermal, economic, or operational characteristics that make them more attractive for the LS-VHTR. The various candidate salts were studied in a parallel task during 2005 with respect to thermo-physical properties [Williams, 2005a] and chemical issues [Williams, 2005b]. Key nuclear characteristics of Flibe are presented here to help interpret and understand results of the core neutronics analyses presented in Sect. 5, and to help justify the decision to focus on Flibe for the present design study.

4.1 NUCLEAR CROSS SECTIONS

The macroscopic cross sections of the Flibe coolant were compared with the other basic materials in the core (graphite and fuel) to understand their relative magnitudes. Figure 4.1 shows the macroscopic capture and scatter cross sections for the core materials as a function of energy (from the SCALE 238-group ENDF/B-VI library). The Flibe cross sections are plotted with two lithium enrichments—a low enrichment (99.99% ^{7}Li = 100 ppm ^{6}Li) and a high enrichment (99.999% ^{7}Li = 10 ppm ^{6}Li).

The graphite (in blue) is easily seen as an excellent moderator with a large scattering cross section and very small capture cross section. The fuel (in green) has the largest neutron capture cross section (nonfission) at all energies except the high epithermal range. In addition, it also has a larger scattering cross section than the Flibe (pink and maroon). The thermal (and low-epithermal) capture cross section of the low-enriched Flibe (100 ppm ^{6}Li) is a factor of 2 larger than the high-enriched (10 ppm), but otherwise they are nearly equal. Therefore, we can see that the capture and scattering cross section of the Flibe is relatively small compared to the fuel. The Flibe coolant is a weak neutron moderator, but also a weak absorber, thus, nearly transparent to neutrons.

The baseline coolant used in this study is 50 ppm ^{6}Li (99.995% ^{7}Li). This level of ^{7}Li enrichment was chosen based on the Flibe material that was used in the MSRE [Thoma, 1971]. Sampling of the MSRE salt yielded enrichments ranging from 99.992 to 99.996%. As will be discussed in Sect. 5, the neutronic performance of Flibe is very sensitive to the ^{6}Li isotopic content. The reason for this is clearly demonstrated in Fig. 4.2, which shows the microscopic cross sections of ^{6}Li and ^{7}Li for both the elastic scattering and total cross sections. While the ^{7}Li total and elastic scattering cross sections are nearly identical, the substantial difference between the ^{6}Li total and elastic scattering cross sections is due to the ^{6}Li(n,t) capture reaction, which dominates all other lithium reactions.

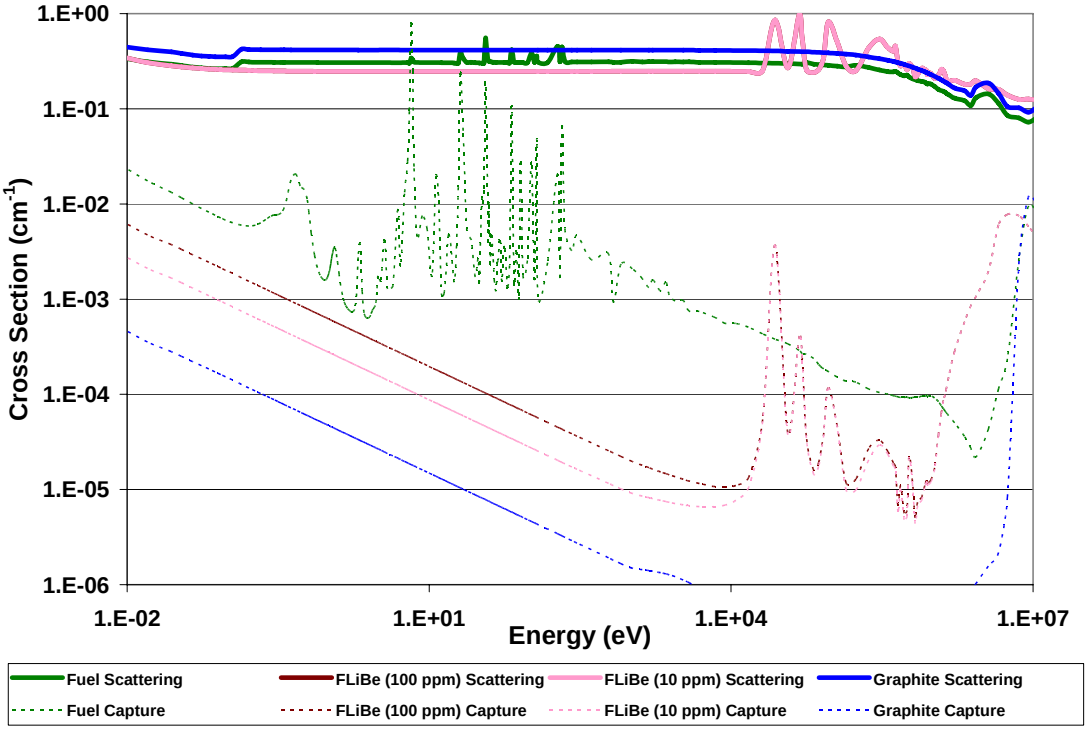

Fig. 4.1. Macroscopic cross sections of basic materials in the LS-VHTR core.

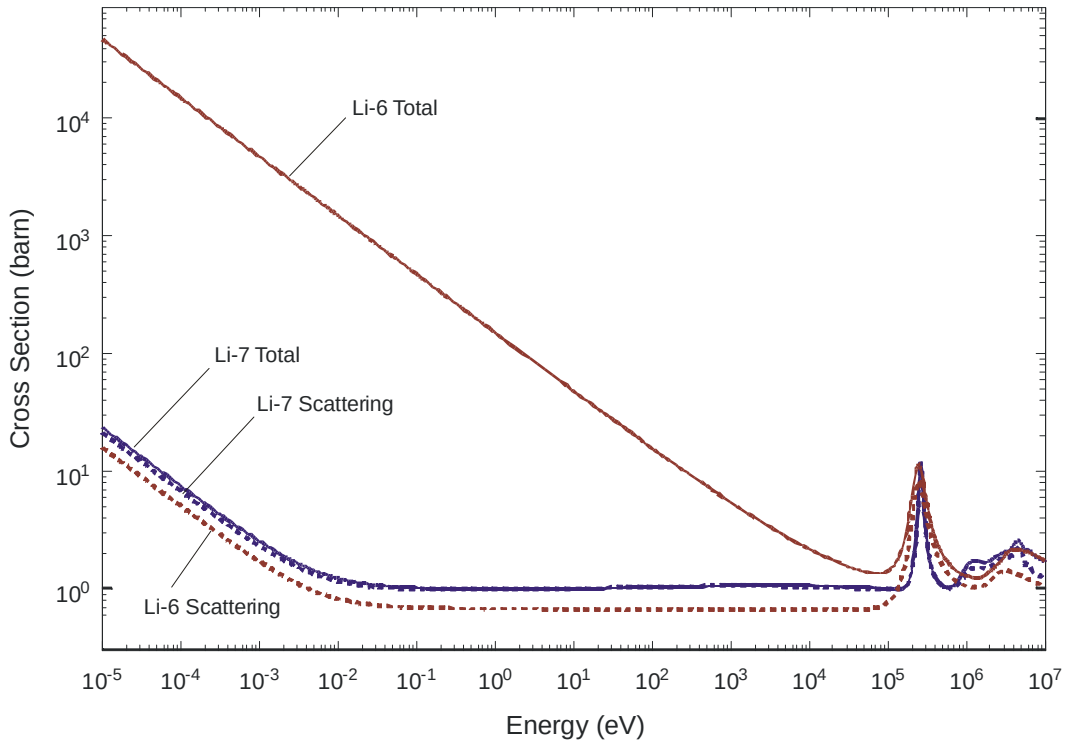

Fig. 4.2. Comparison of ^{6}Li and ^{7}Li microscopic cross sections.

4.2 ABSORPTION AND MODERATING PROPERTIES

The thermal-spectrum LS-VHTR reactor core design consists of three major constituents—fuel, moderator, and coolant. The fuel consists of TRISO-coated particles in cylindrical fuel compacts. The graphite moderator reduces the energy of neutrons so that they will be easily absorbed in the fuel to cause additional fissions. Any neutrons that are captured and do not result in a fission reaction are considered parasitic to the critical chain reaction in the core. Graphite has a very small probability of capturing neutrons; therefore, a major component of parasitic neutron capture is the liquid-salt coolant (in addition to ^{238}U, other actinides, and fission products). The parasitic neutron capture rate is directly related to the efficiency of fuel utilization—increased parasitic neutron capture requires additional fuel to maintain a critical system.

The ability of the coolant to moderate neutrons can offset the negative impact of parasitic capture. The relationship between capture and moderation is especially significant during a theoretical accident scenario, when all or part of the coolant is lost and the coolant channels are voided. The LS-VHTR is designed to be very under-moderated, such that if moderator (such as the coolant) is lost, the reactivity is reduced. The balance between moderation and absorption determines if the loss of the coolant results in a positive or negative reactivity effect.

In addition, the parasitic neutron captures in the salt activate the coolant materials, which results in additional, often radioactive, isotopes flowing throughout the coolant circuit. These present a challenge to online maintenance and refueling processes. Radioactive isotopes that are produced by prolonged irradiation of the coolant may also present challenges to disposal of this coolant after the lifetime of the reactor.

Table 4.1 displays the parasitic neutron capture rates for several candidate salts relative to pure graphite (on a per unit volume basis). The table also displays the Moderating Ratio, which is a Figure of Merit that relates the effectiveness of moderation vs the parasitic neutron capture for a given energy range:

$$Moderating\ \ Ratio = \frac{\xi\Sigma_s\phi(\Delta E)}{\Sigma_c\phi(\Delta E)} \tag{1}$$

where

$\xi\Sigma_s\phi(\Delta E)$ is the rate of energy loss (lethargy gain) due to neutron scattering for a given energy range,

$\Sigma_c\phi(\Delta E)$ is the rate of parasitic neutron capture for the same energy range, and

ΔE is 0.1 to 10 eV for this analysis.

Table 4.1. Neutronic efficiency for candidate coolants and comparison materials

Material	Total neutron capture relative to graphite (per unit volume)	Moderating ratio (Avg. 0.1 to 10 eV)
Heavy water	0.2	11449
Light water	75	246
Graphite	1	863
Sodium	47	2
UCO	285	2
UO_2	3583	0.1
LiF-BeF_2 (67-33)	8	60
LiF-BeF_2-ZrF_4 (64.5-30.5-5)	8	54
NaF-BeF_2 (57-43)	28	15
LiF-NaF-BeF_2 (31-31-38)	20	22
LiF-ZrF_4 (51-49)	9	29
NaF-ZrF_4 (59.5-40.5)	24	10
LiF-NaF-ZrF_4 (26-37-37)	20	13
KF-ZrF_4 (58-42)	67	3
RbF-ZrF_4 (58-42)	14	13
LiF-KF (50-50)	97	2
LiF-RbF (44-56)	19	9
LiF-NaF-KF (46.5-11.5-42)	90	2
LiF-NaF-RbF (42-6-52)	20	8

In Table 4.1, the total neutron capture of light water (H_2O) is very large; much larger than the other traditional moderators, such as heavy water (D_2O) or graphite, and also most of the salts. However, the excellent moderating power of light water leads to a much larger moderating ratio than any salt coolant. The neutron capture rate of the salts is much larger than (pure) graphite; therefore, minimizing the coolant in the core will improve the fuel efficiency substantially from a neutronics perspective.

The BeF_2 salts (red font) have the best neutronics properties (large moderating ratios and small parasitic capture rates), while the alkali fluorides (green font) have the worst. The salts with low moderating ratios can be expected to have the highest increase in reactivity when a void displaces coolant.

4.3 CONCLUSIONS ON SALT NUCLEAR PROPERTIES

Many aspects of reactor design must be considered to determine the most suitable salt for the LS-VHTR. From a nuclear properties perspective, the salt should have very little parasitic neutron capture and high moderating power. The coolant that best matches these characteristics is Flibe. The fluorine and highly enriched ^{7}Li have very small neutron cross sections and beryllium is an excellent moderator. Therefore, the majority of initial studies focused on this coolant, although some investigations considered other options.

This page intentionally blank

5. COOLANT VOID REACTIVITY

A major requirement of any nuclear reactor design is its favorable response to anticipated transients or severe accidents. One common aspect of many accident simulations is the loss of coolant (or depressurization) in all or part of the reactor core, which could occur, in theory, from coolant boiling, a gas bubble entrapped in the system, or a blocked coolant channel. In these transients, the increase in reactivity should be minimized (preferably decrease) when the coolant is removed and replaced by a voided region. To ascertain the effect of coolant voiding on the reactivity of the system, the coolant void reactivity (CVR) is defined as the reactivity of the cooled system minus the reactivity of the voided system:

$$CVR = \frac{1}{k_{cool}} - \frac{1}{k_{void}}, \tag{2}$$

where k_{cool} is the infinite neutron multiplication factor (k_{inf}) for the system with the coolant present, and k_{void} is the multiplication factor with the coolant removed (voided). The units of CVR are either in milli-k (mk) or dollars ($), where one milli-k is one thousandth of a unit of reactivity, and a dollar is relative to the delayed neutron fraction $\left(\frac{\nu_d}{\nu} \approx 0.007\right)$. Therefore,

$$CVR(mk) = \left(\frac{1}{k_{cool}} - \frac{1}{k_{void}}\right) * 1000, \tag{3}$$

$$CVR(\$) = \left(\frac{1}{k_{cool}} - \frac{1}{k_{void}}\right)\left(\frac{\nu}{\nu_d}\right). \tag{4}$$

Ideally, the CVR should be negative such that a voiding of coolant will lead to a reduction in reactivity, which effectively shuts down the reactor. A positive reactivity insertion of less than one dollar requires the contribution of delayed neutrons to maintain a supercritical reactivity level, which allows more time for operator intervention during a transient, if required. One dollar of reactivity is considered a prompt-critical reaction, which cannot be controlled by the operator, and control of the reactor must be contained through inherent properties of the system.

5.1 FOUR-FACTOR FORMULA ANALYSIS

The four-factor formula is a simple breakdown of the reaction rates to determine how the spatial and spectral changes to the flux affect the multiplication factor. The components of the four-factor formula can be used to understand the physics that result in changes in the multiplication factor and, therefore, the coolant void reactivity. The factors evaluated include:

- reproduction factor (η): fission neutrons from thermal neutrons per absorption of a thermal neutron in the fuel,
- fuel utilization factor (*f*): thermal neutrons absorbed in fuel per total thermal neutron absorbed,
- fast fission factor (ε): total fission neutrons produced per fission neutron from thermal neutrons, and

- resonance escape probability (p): probability that a neutron does not get absorbed in the fast or epithermal energy range.

The eigenvalue is the product of all of these factors: $k = \eta f \varepsilon p$.

Therefore, the contribution to the CVR from each factor individually is defined as

$$\Delta r(\$) = \left(\frac{1}{k^r_{cool}} - \frac{1}{k^r_{void}} \right) \left(\frac{\nu}{\nu_d} \right) \qquad r = \eta,\ f,\ \varepsilon,\ or\ \ p, \tag{5}$$

where:

$$k^r_x = \left(\frac{r_x}{r} \right) \bar{k}, \qquad x = cool\ or\ void,$$

$$\bar{r} = \frac{1}{2}\left(r_{cool} + r_{void} \right), \quad \bar{k} = \bar{\eta}\,\bar{f}\,\bar{\varepsilon}\,\bar{p}.$$

The components of the four-factor formula were calculated and compared for the fully voided and fully cooled states of the basic design of the LS-VHTR. Reaction rates were obtained with the following group structures: 0 to 0.625 eV (thermal), and 0.625 eV to 20 MeV (fast). The fuel in four-factor analyses presented below has an enrichment of 14% rather than the baseline 10% to reflect an update in the LS-VHTR design to meet an 18-month cycle length. This higher fuel enrichment increases the CVR for the base LS-VHTR design from \$0.05 to \$0.37.

Table 5.1 shows the results of the four-factor analysis for the base LS-VHTR design with 14% enriched fuel and no BP. The reproduction factor (η) is essentially unchanged because there is little change in the thermal spectrum and all fuel is identical. There is a \$0.62 increase in the CVR due to the increased fast fission factor (ε). The spectrum hardens slightly because of a loss of moderation and a loss of a thermal neutron absorber, so the ratio of fast to thermal neutrons increases, and more fast fission occurs—relatively. The fuel utilization factor (f) also increases significantly (\$1.40) because the coolant was the only significant nonfuel thermal neutron absorber. However, the hardening of the spectrum results in relatively more neutrons being in the resonance range, which significantly decreases the resonance escape probability (p). This leads to a small positive CVR, \$0.37, for the base geometry with 14% enriched fuel and no BP.

Table 5.1. Four-factor analysis of the baseline geometry

Baseline geometry	Cooled	Voided	Effect on CVR
η	1.9855	1.9854	\$0.00
ε	1.1532	1.1603	\$0.62
f	0.9717	0.9854	\$1.40
p	0.6391	0.6287	–\$1.65
Eigenvalue	1.4220	1.4272	\$0.37
Uncertainty	0.0001	0.0001	\$0.02

5.2 IMPACT OF LITHIUM ENRICHMENT AND FUEL BURNUP

CVR was calculated as a function of burnup for the reference fuel-element design, using the deterministic lattice codes WIMS8 and DRAGON. The burnup-dependent CVRs were obtained by branch calculations at the burnup points of interest using full voiding of the coolant to derive the 100% voiding reactivity effect. The results were then normalized to the reactivity change per percent voiding. Due to the limited resources available for the ANL analysis, there was insufficient time to prepare cross sections corresponding to the high temperatures in the LS-VHTR. Hence the results are more appropriate for relative comparisons. For the assembly CVR study, an assembly fuel enrichment of 15% and fuel packing fraction of 25% were used. Variation of the lithium enrichment (from the reference value of 99.995 to 99.99%) was utilized to evaluate the impact of this parameter on the reactivity coefficient result.

Results of the study are summarized in Table 5.2. Note that the CVR is expressed in terms of "pcm/%void," which is numerically equivalent to "milli-k" defined earlier. Noticeable differences are observed in the CVR values calculated by the WIMS8 and DRAGON codes. The differences between the two codes were also found to become larger with burnup. The reason for these differences has not been investigated completely in the current study. It is, however, probably due to differences in basic cross-section data (JEF2.2 for WIMS8 and ENDF/B-VI for DRAGON) and differences in material compositions at burnup points arising from different solution methodology and code data. It is noted that the magnitude of the differences is actually small, the largest difference being about 600 pcm for 100% voiding for the case with lithium enrichment of 99.99% and about 300 pcm for 100% voiding for the case with lithium enrichment of 99.995%. The results also show that the magnitude of the positive CVR is small, being less than $1 per 100% voiding (assuming a delayed neutron fraction value of 600 to 700 pcm). Further evaluations of the differences with burnup, however, need to be performed.

Additionally, the results indicate that the WIMS8 and DRAGON codes give similar trends for the CVR. It is observed that the coefficient is positive at the beginning of cycle and decreases with increasing burnup. At a burnup between 15 and 20 GWd/t, the fuel element CVR becomes negative in the case using a lithium enrichment of 99.995%. This suggests that by using more than one fuel batch, the coefficient could be made negative. This has to be confirmed in future studies with whole-core models. It is expected that the unit element CVR values presented in Table 5.2 are actually more positive (i.e., higher) than those that would be obtained from whole-core calculations, because neutron leakage tends to reduce the CVR. Furthermore, the results show that the CVR is dependent on the lithium enrichment. The coolant void reactivity coefficient for the 99.99% lithium enrichment case is more positive than that for the case with a lithium enrichment of 99.995%.

The reduction of the CVR value with burnup is due to the decrease in the neutron absorption in lithium arising from the competition with other absorbers (fission products) created as part of the fission process. It is also noted that the spectrum hardens with burnup which further enhances the reduction. The decrease of the CVR with increasing lithium enrichment results primarily from the reduction of the neutron absorption in ^{6}Li. Clearly, one approach to reduce the CVR is to increase the lithium enrichment. This could, however, be costly.

Table 5.2. Comparison of coolant void reactivity (pcm/%void)

	Lithium enrichment of 99.99%		Lithium enrichment of 99.995%	
Burnup (GWd/t)	**WIMS8**	**DRAGON**	**WIMS8**	**DRAGON**
0.0	3.6	5.4	0.2	1.5
15.0	3.0	2.9	–0.4	–0.2
30.0	1.6	0.4	–1.8	–2.4
45.0	0.6	–2.0	–3.0	–4.2
60.0	–0.2	–4.2	–4.0	–6.1
90.0	–1.0	–7.1	–5.3	–8.6

5.3 IMPACT OF FUEL TEMPERATURE

A parametric study was performed that involved hot and cold operating temperatures representing the inlet and outlet conditions. Additional calculations were performed at room temperature for comparison with MCNP, although all salts are solid at room temperature and, therefore, voiding is not possible.

The specific temperatures used in the analyses are as follows:

	Temperature (^{o}C)		
	Flibe	**Graphite**	**Fuel**
Hot (outlet)	1000	1030	1120
Cold (inlet)	900	930	1020
Room temperature	25	25	25

Figure 5.1 shows that the CVR is substantially lower at operating temperatures than the room temperature calculations that were used for an MCNP benchmarking analysis. Therefore, it is important to perform the core analysis calculations at, or near, the nominal conditions of the reactor. Subsequent analyses reported here use only the operating temperatures.

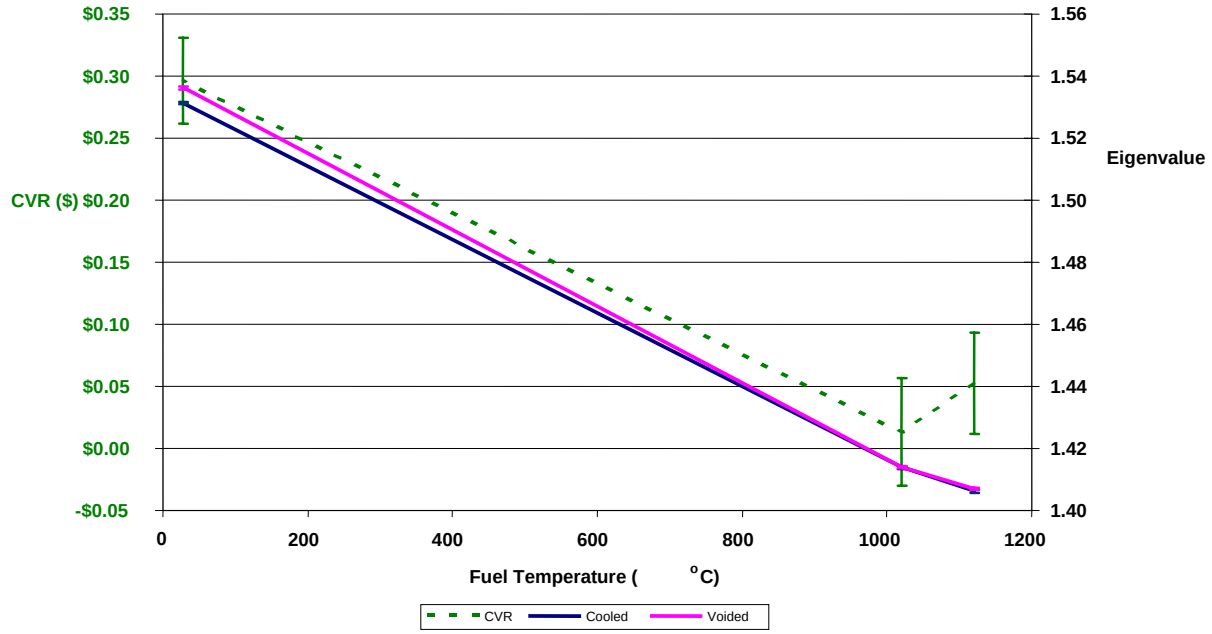

Fig. 5.1. Eigenvalue (k_{cool}) and CVR as a function of fuel temperature.

One major inherent property of a nuclear reactor that contributes to its stability is the Doppler reactivity effect. As the temperature rises in a material, the resonances in the cross section broaden over a larger energy range and more neutrons are captured without producing a fission reaction. The isotope of greatest significance in most thermal spectrum reactors (including the LS-VHTR) is ^{238}U; however, many BPs (like erbium) also have very significant resonances. The fuel temperature coefficient (FTC) is defined as the change in reactivity per degree change in fuel temperature:

$$FTC = \frac{\left(\frac{1}{k_1} - \frac{1}{k_2}\right)}{T_1 - T_2}. \qquad (6)$$

The Doppler broadening of cross sections in the LS-VHTR leads to a very strong negative FTC (–\$0.50/100°C) as compared to a traditional light-water reactors (LWRs) (–\$0.006/100°C). Therefore, even with a positive CVR (but still below one dollar), the increase in fuel temperature will quickly shut down the critical reaction. However, there is substantial interest in providing a design of the LS-VHTR that has a negative CVR and, thus, does not rely on the FTC to ensure that the fuel will not fail in the event of a coolant voiding situation.

In the case of coolant voiding resulting from boiling, in which the coolant temperatures are substantially larger than the operating temperature (>1400°C), then the corresponding fuel temperature would also increase from the nominal operating conditions. Therefore, the overall reactivity effect is a combination of the CVR and FTC. The fuel temperature rise would, as a result of the Doppler broadening of the cross sections, reduce the net reactivity change with respect to a simple constant temperature voiding scenario.

In Fig. 5.2, a new parameter has been defined—the net void reactivity (NVR). The NVR is a combination of the fuel temperature coefficient and the coolant void reactivity [defined in Eq. (6)]. Therefore, if the initial operating temperature is equal to the final transient temperature ($\Delta T=0$), the NVR is simply the CVR. However, if an increase in fuel temperature is taken into account, the NVR will be reduced by the negative FTC.

$$NVR(\$,\Delta T) = CVR + FTC * \Delta T = \left(\frac{1}{k_{cool}(T_i)} - \frac{1}{k_{void}(T_i + \Delta T)} \right) \tag{7}$$

As shown in Fig. 5.2, the reactivity is very negative when a simple ten-degree temperature rise is assumed because the FTC is very large compared with the CVR. This shows that a voiding scenario that leads to a temperature rise would quickly be shut down even if the CVR is slightly positive.

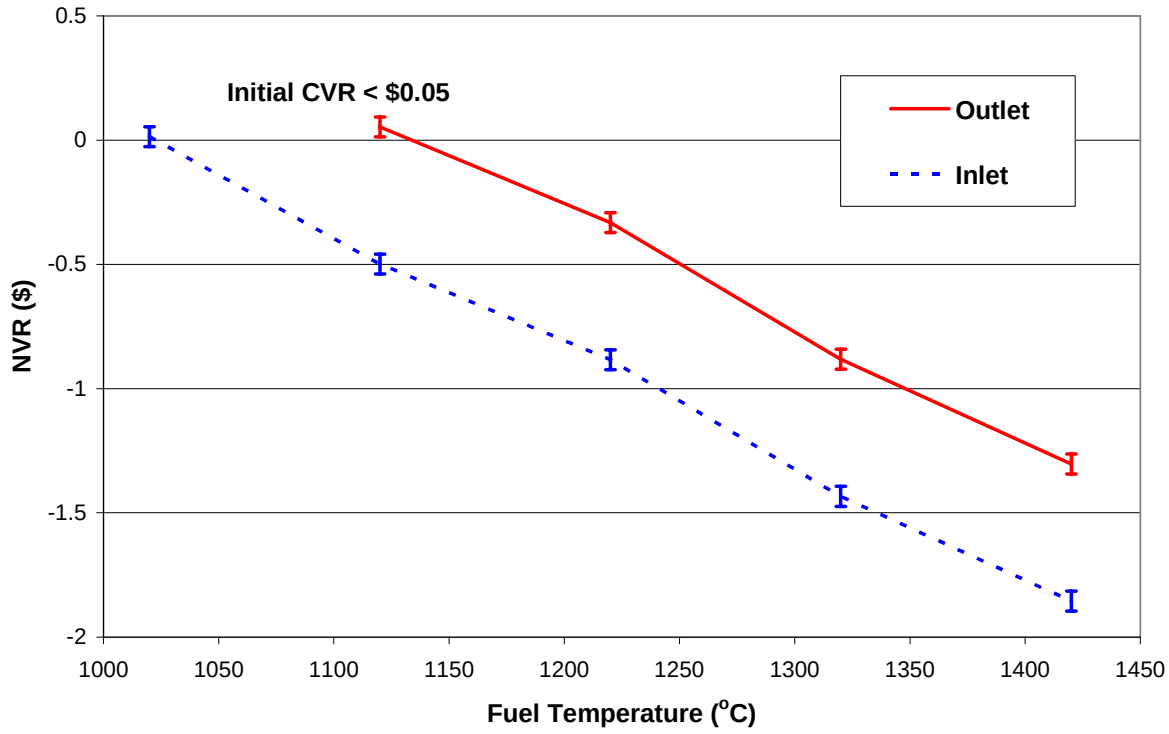

Fig. 5.2. NVR by initial fuel temperature.

5.4 IMPACT OF FUEL ENRICHMENT AND LOADING

A parametric study was performed to evaluate the effect of uranium enrichment and fissile ^{235}U block loading on the void coefficient. It should be noted that each fuel block loading was assumed to be uniform across the active core.

Figure 5.3 shows the void reactivity (Δk) as a function of both fissile uranium ^{235}U loading and enrichment for the reference 2:1 molar ratio Flibe or $^{2}LiF\text{-}BeF_2$. For the three enrichments considered—10, 15, and 20 wt % ^{235}U—the void reactivity (Δk) changed from positive to negative with increasing ^{235}U fissile loading. From this result, the design goal would be to employ as heavily loaded fuel blocks as possible in the LS-VHTR core, and interestingly enough, our estimated range of 900 to 1200 g ^{235}U per block to meet power cycle requirements coincides nicely with the negative void coefficients. In fact, the void coefficients are strongly negative in the 900 to 1200 g ^{235}U per block range, particularly for 10 to 15 wt % enrichment.

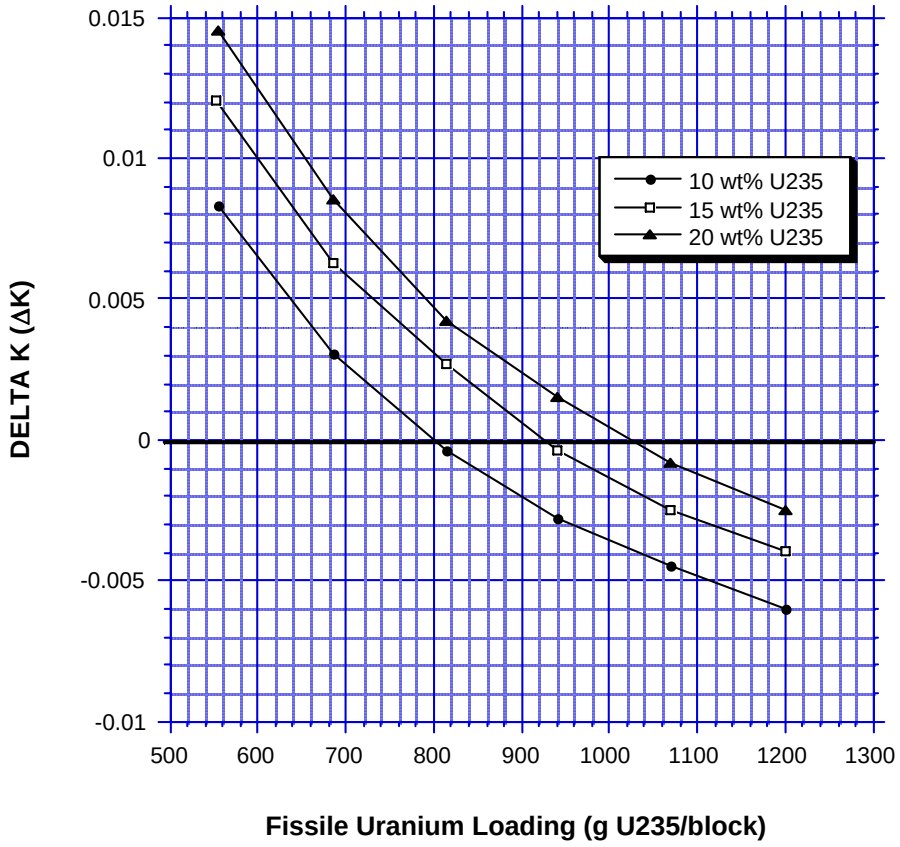

Fig. 5.3. Flibe void reactivity as a function of uranium enrichment and ^{235}U fissile block loading.

Also, it is readily observed in Fig. 5.3 that the lower the uranium enrichment, the more negative the void coefficients become. This is indicative of the important role ^{238}U plays in the spectral absorption interplay between the uranium and Flibe necessary to produce these more negative void coefficients. A lower uranium enrichment will also help reduce LS-VHTR fuel costs, although the overall uranium mass per block will increase.

5.5 IMPACT OF BURNABLE POISONS

The results presented in Sect. 5.2 show that the CVR is reduced with burnup. This trend suggests that the void reactivity coefficient of a *multibatch* core could be negative at the beginning and throughout the equilibrium cycle. This trend does not, however, preclude the fact that a solution must be found for the coolant void reactivity coefficient of the *initial* core. Burnable poisons have, therefore, been suggested as a means of ensuring a negative void reactivity coefficient for the LS-VHTR. Generally, BPs are used in reactor designs to compensate the excess reactivity (reduce the control rod worth requirements) and to suppress core power peaks. In the helium-cooled VHTR, the control of power peaks using burnable absorber is very important because high power values would develop otherwise at the interface between the core and the inner reflector. This power peak suppression role is less important in the LS-VHTR because of the use of the solid cylindrical core. However, a BP could prove useful for reducing the CVR and, hence, the performance of typical BP has been evaluated in this study.

From physics reasoning, the introduction of the BPs provides competition for neutron absorption in lithium and, thus, reduces the impact of the loss of coolant (primarily ^{6}Li effect) on the CVR. A BP having appropriately located thermal absorption resonances could make the void reactivity coefficient negative following neutron spectral hardening arising from the coolant voiding. Figure 5.4 is a plot of the absorption cross sections of candidate BP nuclides and ^{6}Li. It also includes the neutron spectrum of the LS-VHTR fuel assembly. The neutron spectrum of the LS-VHTR has a thermal neutron flux peak at about 0.3 eV. The lowest resonance absorption energies of ^{167}Er, ^{163}Dy, and ^{157}Gd are 0.5, 1.74, and 2.85 eV, respectively. The absorption cross sections of these nuclides have a 1/v shape below these resonance energies, as does ^{6}Li. This figure suggests that erbium is the most favorable candidate for BP of the LS-VHTR because the resonance of ^{167}Er is closest to the thermal neutron flux peak. Gadolinium would likely be the most ineffective, particularly because of its large thermal absorption cross section and location of its first resonance peak. These two features combined might make the coolant void reactivity coefficient more positive than the case without BP, particularly at low burnup.

In the current study, it is assumed that the BP is distributed uniformly in the graphite block in minute (mg per kg) quantity. While the impact of this assumption on the thermal and structural performance of the graphite block has not been evaluated, placing BP in the blocks might be necessary neutronically, since it ensures that fuel compact locations in the fuel element are not used for BP compacts. Using lumped BP compacts also reduces the poisoning effect due to resonance self-shielding. In the LS-VHTR design, the replacement of fuel compacts with BP compacts might result in quite high uranium enrichment requirement or the inability to meet the cycle length requirement. It might however be necessary, for the sake of completeness, to consider the use of BP compacts in future studies.

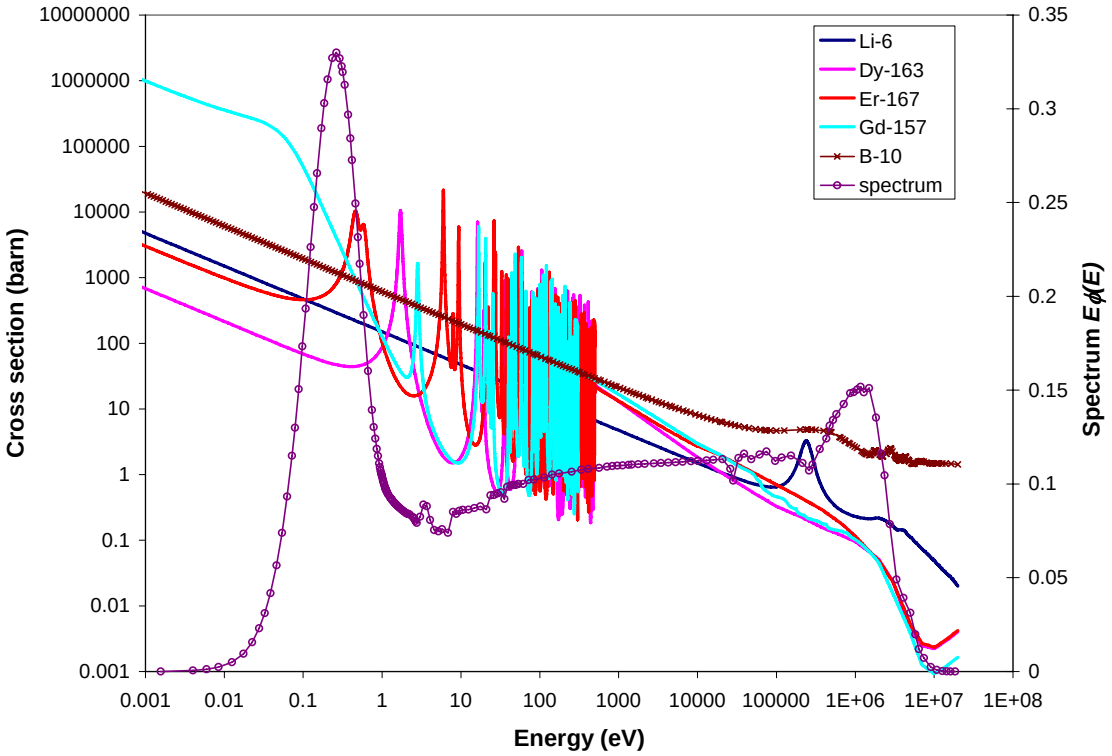

Fig. 5.4. Comparison of absorption cross sections and LS-VHTR spectra.

In Fig. 5.5, the void reactivity coefficients are compared for LS-VHTR fuel elements using the different BP nuclides. In these calculations, the BP content in the graphite block is 150 ppm (mass fraction) for the rare earth elements. Because the atomic weight of boron is about one-tenth of the rare earth isotopes, the boron content was reduced to 15 ppm in order to have a similar BP number density in the graphite blocks for all cases. As expected, gadolinium increases the coolant void reactivity coefficient at low burnup due to the 1/v nature of the gadolinium capture cross section in the vicinity of the thermal flux peak. Other BP nuclides decrease the coolant void reactivity coefficient, relative to the no-BP case due to capture resonances just above the thermal peak, especially erbium (shown in Fig. 5.4). The competition with fission product nuclides and other irradiation products (e.g., plutonium and minor actinides) is the reason why dysprosium appears attractive at high burnup. However, all of the BPs burn out quickly and their impact on the void reactivity becomes negligible comparable to the no-BP case beyond a burnup of 15 GWd/t.

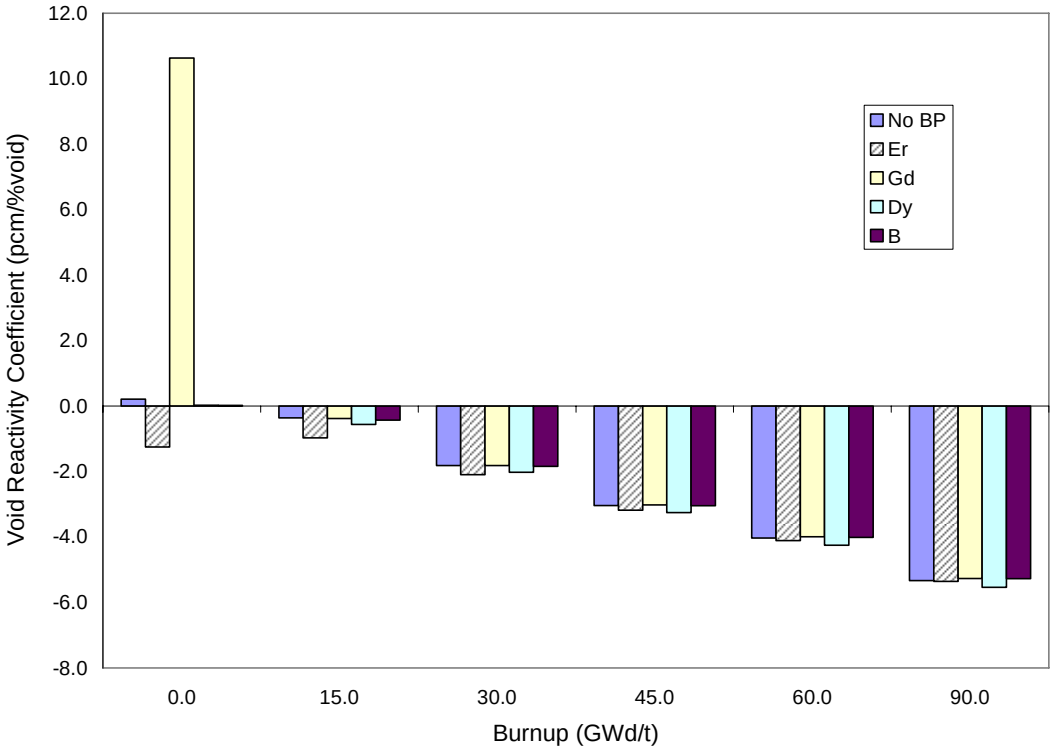

Fig. 5.5. Impact of BPs on CVR.

As noted in the previous section, when the coolant channels of the LS-VHTR are voided, there is a slight hardening of the energy spectrum because of a loss of moderation and loss of thermal absorber. Therefore, if BPs with resonances near the upper thermal and lower epithermal energy range are placed in the fuel, then when the spectrum hardens there will be an increased number of neutrons in the poison's resonance range (relatively). Erbium is a good option for a BP because of its 0.5-eV resonance.

Table 5.3 shows the change in the CVR based on the four-factor components as erbium is introduced into the fuel. Because of the hardened spectrum, there are more neutrons absorbed in the epithermal resonances (reduced *p*) and the thermal resonance in the fuel (reduced η). However, there is also an increase in the fast fission factor (ε) as the amount of thermal fission is reduced, relative to fast. This results in a net reduction of the CVR to a very small (positive or negative) number. In addition, because the multiplication factor is approaching unity as the poison is added to the fuel, there is only a limited range of applicability.

Table 5.3. Four-factor analysis of the baseline configuration with erbium poison

Baseline geometry	No poison	25 mg/cm^3 of Er_2O_3	50 mg/cm^3 of Er_2O_3
k_{cool}	1.42	1.24	1.10
η	\$0.00	–\$0.17	–\$0.35
ε	\$0.62	\$0.90	\$1.16
f	\$1.40	\$1.40	\$1.40
p	–\$1.65	–\$2.05	–\$2.27
CVR	\$0.37	\$0.08	–\$0.06
Uncertainty	\$0.02	\$0.01	\$0.01

5.6 SPECTRAL EFFECT ON THE CVR

The use of neutron spectrum variation to make the void reactivity coefficient more negative was also evaluated. The spectrum was changed by varying the fuel-to-moderator ratio (i.e., increasing the diameter of the coolant hole or increasing the total number of fuel pins). The changes in the design parameters and the results are summarized in Table 5.4. These variations in core parameters would affect the thermal hydraulic and safety characteristics of the reactor. At this point, however, only the impacts on the neutronics characteristics have been evaluated to provide guidelines for the void reactivity coefficient as a function of neutron spectrum. The primary design data of the three cases are nearly the same except for the total number of fuel pins (as well as coolant holes) and coolant hole diameter. The total number of fuel pins is increased to 234 (the total number of coolant holes decreases to 90) in the *many-fuel-pin* case and the diameter of the coolant hole in the *large-coolant-hole* case is increased to that of the diameter of the current helium-cooled VHTR design.

Table 5.4. Comparison of liquid-salt-cooled VHTR design data

Case	Reference case	Many fuel pins	Large coolant hole
Total number of fuel pins in assembly	216	**234**	216
Total number of coolant holes in assembly	108	**90**	108
Fuel rod channel OD, cm	1.27	1.27	1.27
Coolant channel OD, cm	0.953	0.953	**1.5875**
Pitch between fuel holes, cm	1.8796	1.8796	1.8796
Specific power density, W/g	158	**146**	158
Packing fraction, %	25	25	25
Initial k_{inf}	1.4749	1.4549	1.4335
Reactivity swing, %Δρ	30.8	29.9	28.9
Discharge burnup of two-batch core, GWD/t	156	144	138
Cycle length of two-batch core, EFPD	**494**	**494**	**435**

The spectra of the three cases are compared in Fig. 5.6. The increase in the total number of fuel pins or the change to a larger coolant-hole diameter results in a reduction of the thermal flux and an increase in the epithermal flux. Since lithium and ^{19}F have resonances at ~250 keV and ~27 keV, respectively, the resonance effects of the coolant constituents are observed for the case with the large coolant holes. The spectrum changes affect the core neutronic performance and characteristics as indicated by the results provided in Table 5.4. For the *large coolant-hole* case, the initial k_{inf} and the cycle length decrease compared to those of the reference case (435 EDPD vs 494 EFPD) because the poison effect of the coolant increased and the reduced moderation resulting from removal of graphite. For the *many-fuel-pin* case, the initial k_{inf} and discharge burnup decrease compared to those of the reference case, but the cycle length is similar due to the smaller specific power density.

The fuel-element CVR and reaction rate variations are summarized in Table 5.5. The reaction rates have been normalized to the corresponding total reaction rate of the unvoided state. The neutron production rate of ^{235}U decreases with coolant voiding, while the neutron production rate of ^{238}U increases by the same magnitude. Thus, the total neutron production rate is unchanged. The total neutron absorption rate is dependent on the fuel element designs. The normalized neutron absorption rates of the heavy metal and graphite increase with coolant voiding, while that of the coolant decreases. Thus, the balance of the neutron absorption rates of the coolant and other materials determines the sign of the void reactivity coefficients.

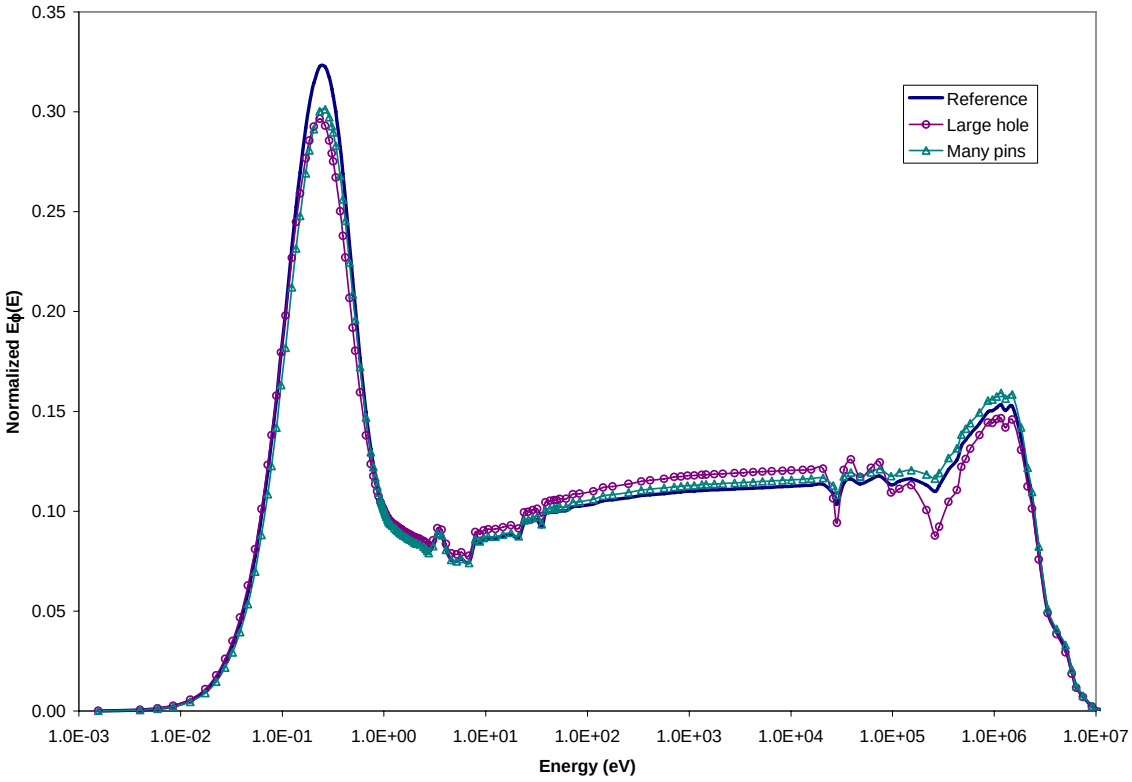

Fig. 5.6. Comparison of spectra of unvoided states.

Table 5.5. Normalized reaction rate variations and CVRs.

	Reference case		Many fuel pins		Larger coolant hole	
	Absorption	**Production**	**Absorption**	**Production**	**Absorption**	**Production**
Change of reaction rate due to coolant voiding (%) at 0 GWd/t burnup						
Graphite	0.02		0.01		0.04	
Coolant	–0.89		–0.68		–2.38	
^{235}U	0.10	–0.03	0.09	–0.03	0.36	0.09
^{238}U	0.75	0.03	0.66	0.03	2.47	0.09
Total	–0.02	0.00	0.09	0.00	0.49	0.00
Void reactivity coefficient (pcm/% voided)						
0 GWd/t	0.2		–0.5		–3.2	
15 GWd/t	–0.4		–1.1		–5.6	
30 GWd/t	–1.8		–2.4		–10.7	
60 GWd/t	–4.0		–4.6		–19.1	
90 GWd/t	–5.3		–5.9		–25.0	

For the reference case, the total neutron absorption rate decreases with coolant voiding, because coolant poison effect is larger than those of other materials. Thus, the void reactivity of the reference case is positive. For the *many-fuel-pin* case, the CVR is negative because the total absorption rate increases slightly. For the *large-hole* case, the neutron absorption rate changes more significantly. In particular, the absorption rate of ^{238}U increases, and it is larger than the coolant poison effect (2.47 vs 2.38). Thus, the void reactivity coefficient becomes more negative compared to the other cases. The increase of the ^{238}U absorption rate can be understood when the spectra of the unvoided and voided cases are compared (see Fig. 5.7); the spectrum hardening due to coolant voiding increases the ^{238}U resonance capture.

In conclusion, these results show that a more negative void reactivity coefficient can be obtained by hardening of the neutron spectrum, relative to the reference design.

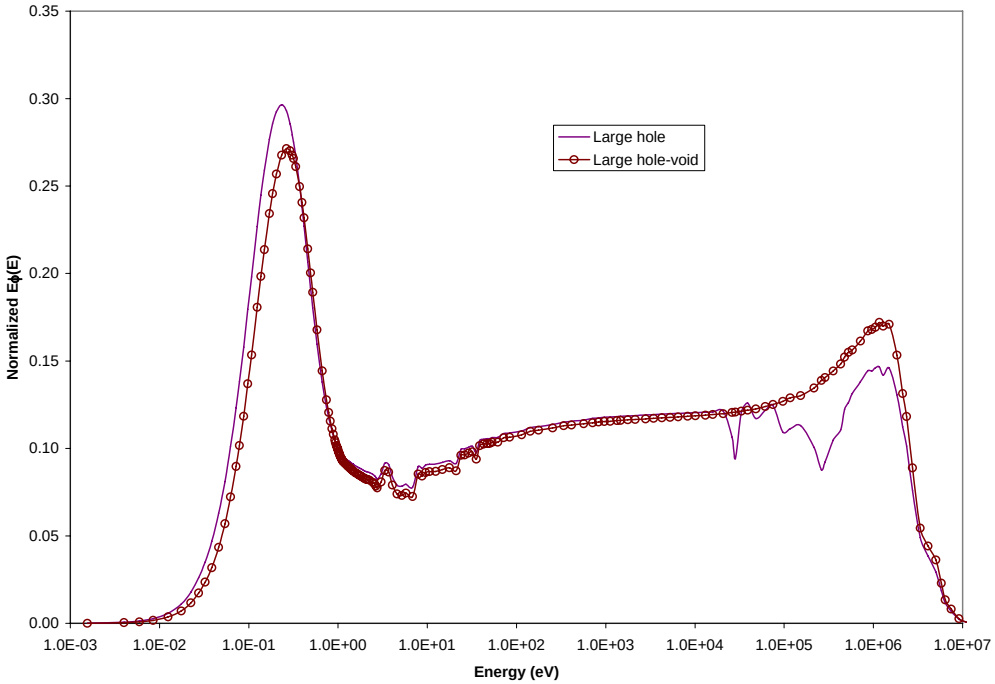

Fig. 5.7. Spectra of unvoided and voided states of large coolant hole case.

5.7 IMPACT OF CORE GEOMETRY

5.7.1 Channel Dimensions and Pitch

The dependence of the CVR and multiplication factor (k_{cool}) in the LS-VHTR on the geometry of the basic design was also analyzed. The fuel and coolant radii were modified with a constant pitch (Figs. 5.8 and 5.9, respectively), and the pitch was modified with a constant fuel/coolant/graphite ratio (Fig. 5.10).

Increasing the fuel radius (replacing graphite with fuel) effectively decreases the moderation in the block, which decreases the eigenvalue. This shows that the current design is substantially under-moderated because a loss of moderation reduces the multiplication factor. Because the coolant has some moderating power, the effect of voiding contributes to a loss of moderation and a reduction in the CVR. Also, the increased amount of fuel adds ^{238}U, which provides additional resonance absorption. In this case, the CVR becomes negative for both the cold and hot states as the fuel radius is increased and the block becomes more under-moderated.

In Fig. 5.9, we can see the effect on the multiplication factor and CVR of a change in the coolant radius. Increasing the coolant radius replaces the graphite moderator with coolant. The multiplication factor decreases slightly because the graphite is a better moderator and has less neutron capture than the coolant. However, the CVR is relatively constant, which shows that the Flibe coolant (99.995% ^{7}Li) is essentially neutronically transparent.

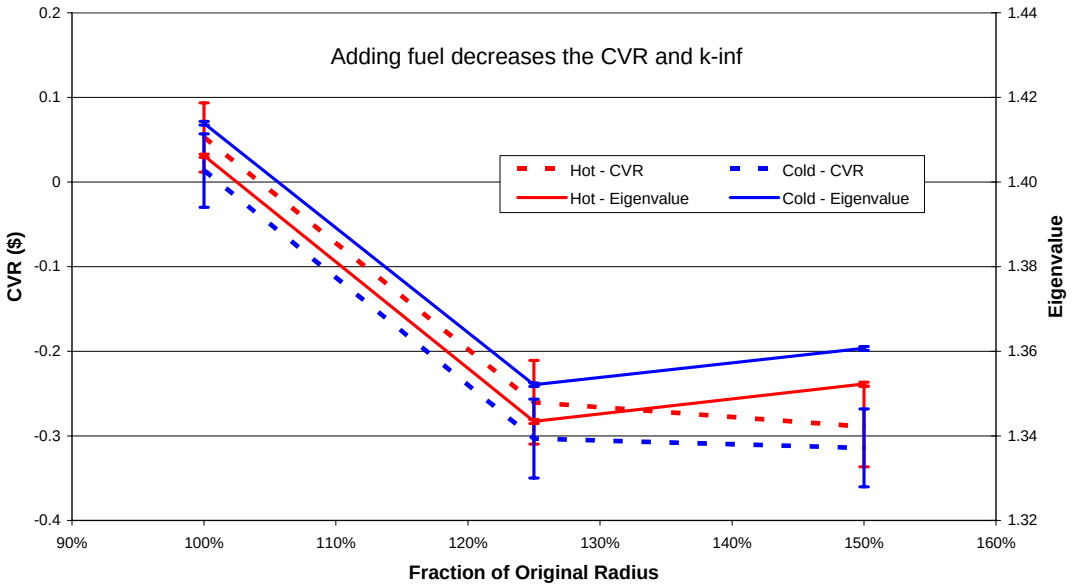

Fig. 5.8. Eigenvalue (k_{cool}) and CVR as a function of fuel radius.

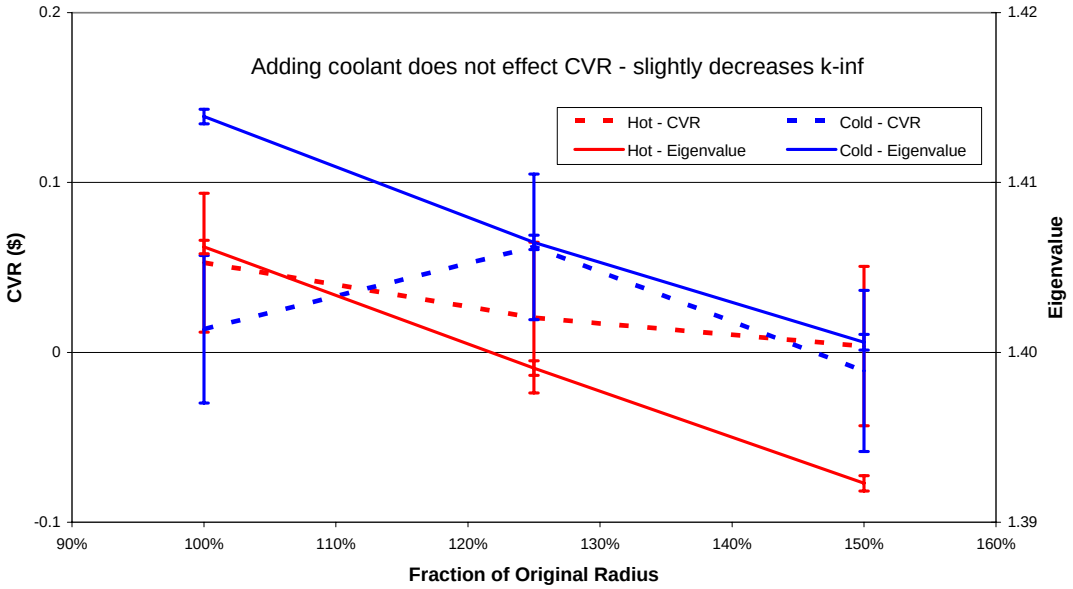

Fig. 5.9. Eigenvalue (k_{cool}) and CVR as a function of coolant radius.

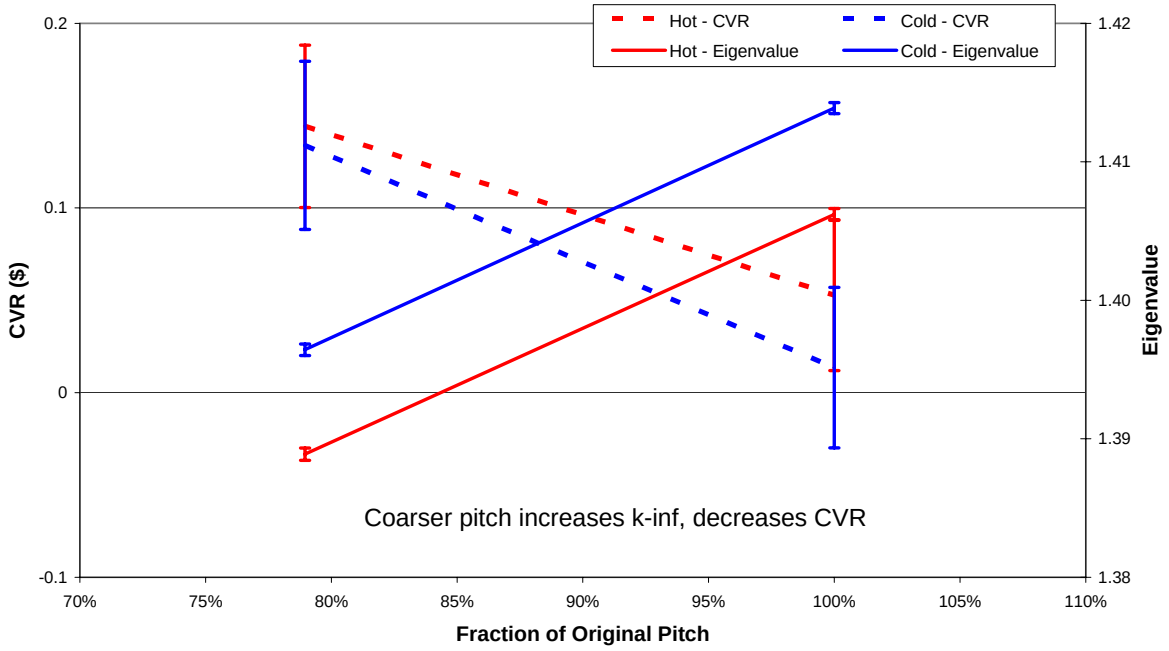

Fig. 5.10. Eigenvalue (k_{cool}) and CVR as a function of channel pitch.

In Fig. 5.10, the results of an analysis of the effect of the pitch (fuel and coolant) on the multiplication factor and CVR are shown. The pitch was reduced from 1.9 cm (216 pins per block) to 1.5 cm (360 pins per block), and the radii of the coolant and fuel channels were reduced to maintain a constant fuel/coolant/graphite ratio. The multiplication factor decreased and the CVR increased as the pitch was reduced. Therefore, it would seem that a coarser (increased) pitch would be very beneficial to both the reactivity and the voiding challenge.

An extreme increase in the pitch and radius leads to several very large fuel pins per block, rather than 216 closely spaced pins. Therefore, this leads to an alternative block design that utilizes a 'clustered-rod' configuration that consists of three to six tightly spaced clusters of fuel pins surrounded by coolant in each block. This would give the effect of a large-pitch geometry, while ensuring the pins are cooled effectively, and could also ease in refueling because every block would not have to be removed, but the clusters could be coupled like a present-day fuel assembly. The results of an analysis of clustered designs are presented in the next section.

A second parametric study was performed to determine the effect on the void reactivity by varying the liquid-salt coolant channel radius and, hence, the volume of liquid salt in the core. Three uranium block loadings using a uranium enrichment of 15 wt % were evaluated. The calculations assumed a Flibe coolant temperature of 950°C and a coolant density of 1.816 g/cm^3.

Figure 5.11 shows the calculated void reactivity (Δk) as a function of the coolant channel radius for different ^{235}U loadings in the fuel blocks. It is interesting to note that as the Flibe coolant channel radius increases, the void reactivity becomes more negative for the two heavier block loadings (941.83 and 1,200.83 g ^{235}U per block). The lighter loaded block (686.19 g ^{235}U

per block) produces a positive void coefficient and becomes more positive with increasing coolant channel radius, or just the opposite of the more heavily loaded blocks.

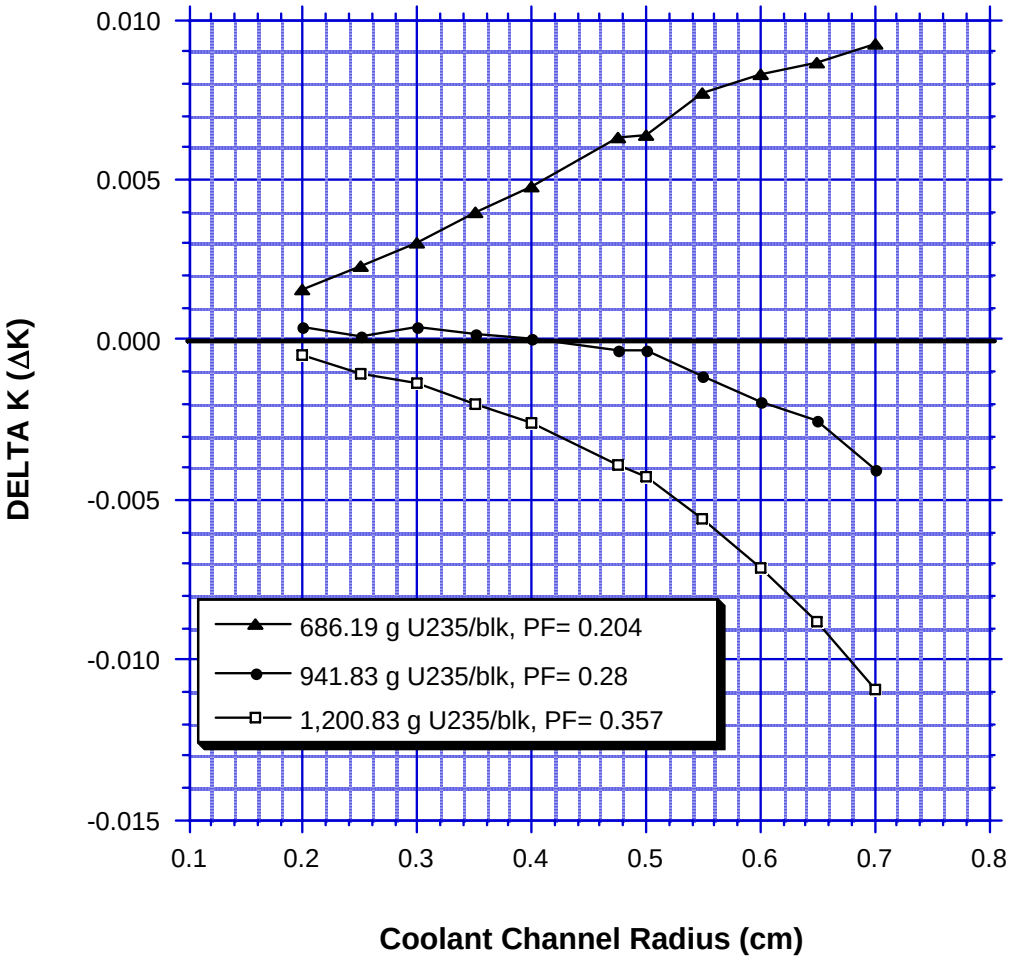

Fig. 5.11. Flibe void reactivity as a function of coolant channel radius and ^{235}U fissile block loading.

5.7.2 Clustered-Rod Configuration

As noted in the previous section, a possible core configuration that will reduce the CVR and maintain a high eigenvalue is a 'clustered-rod' configuration. In this configuration (several possibilities are shown in Fig. 5.12), the fuel pins are clustered in a hexagonal array and surrounded by coolant. Each block contains several (2 to 4) rows of fuel rods in three or six clusters. Each cluster sits within a hole in the graphite block and is surrounded by coolant. The rods are composed of fuel compacts, which are identical to those found in the base configuration,

surrounded by a thin layer of graphite cladding. Each modified block configuration has a comparable fuel/coolant/graphite ratio as the base configuration. The channels for the clustered rods are hexagonal to maintain the coolant volume fraction at 7% of the block.

This block design will simplify refueling because they can be removed like present-day fuel assemblies without moving each entire block individually. Such improvements in refuel options are important since the base configuration has three to four times as many fuel blocks as the gas-cooled VHTR because of the much higher design power. In addition, less graphite will be wasted, because the graphite blocks will not have to be replaced at each refueling. In the 'clustered-rod' configuration, the coolant is in much closer proximity to the fuel than the base-design, which may increase the passive safety limits because the reactor will be cooled by natural circulation of the liquid salt, not conduction through the graphite blocks as in the gas-cooled VHTR.

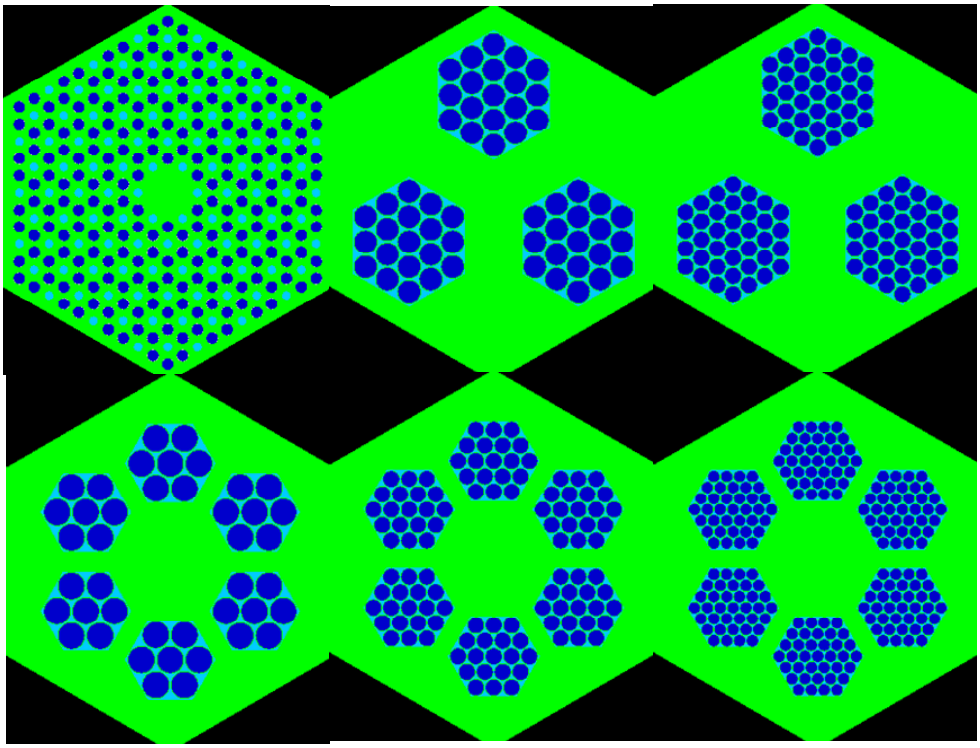

Fig. 5.12. Baseline (top left) and 'clustered-rod' fuel block configurations of the LS-VHTR.

Calculations for several clustered-rod configurations, with a variety of enrichments and BPs, were performed to determine the effect on the reactivity due to voiding. Each design used 14% enriched uranium, and all calculations were performed with KENO-VI and a 238-group ENDF/B-VI cross-section set (2σ uncertainties in the stochastic results are shown).

Table 5.6 shows the results using no BP. The three configurations at the top of Fig. 5.12 are shown in Table 5.6, respectively, and listed by their number of rows and number of clusters per block. The changes in the block design did increase the multiplication factor significantly, but the CVR increased also. The increase in multiplication factor is due to greater self-shielding of the fuel; neutrons tend to be moderated in the graphite and leak back into the fuel at thermal

energies, thus increasing the resonance escape probability. However, this also reduces the importance of the moderating ability of the coolant. The high moderation occurs in the graphite, and the high-power pins are on the outer row of fuel rods in the cluster. Therefore, the moderation of neutrons in the center is less significant and the CVR increases.

Table 5.6. Four-factor analysis of clustered-rod configurations with no poisons

No poison	Baseline geometry	3 Rows 3 Clusters	4 Rows 3 Clusters
k_{cool}	1.42	1.50	1.47
η	\$0.00	\$0.00	\$0.00
ε	\$0.62	\$0.53	\$0.51
f	\$1.40	\$1.21	\$1.24
p	–\$1.65	–\$1.01	–\$0.91
CVR	\$0.37	\$0.73	–\$0.84
Uncertainty	\$0.02	\$0.02	\$0.02

As shown previously, the CVR decreases when BPs are introduced in the graphite moderator or fuel matrix. In this analysis, the erbium poison levels in the fuel matrix of the 'clustered-rod' configurations were adjusted such that the multiplication factor was roughly similar. As shown in Table 5.7, the poison reduced the CVR in the 'clustered-rod' configurations, but it is still significantly greater than the base geometry. The fuel has a constant 14% enrichment in all configurations. In the base geometry, there is 50 mg/cm^3 of Er_2O_3 per compact; the "3 Rows–3 Clusters" (per block) has 55 mg/cm^3; the "4 Rows–3 Clusters" (per block) has 58 mg/cm^3.

Table 5.7. Four-factor analysis of clustered-rod configurations with poisoned compacts

Equally distributed erbium	Base geometry	3 Rows 3 Clusters	4 Rows 3 Clusters
k_{cool}	1.10	1.14	1.09
η	–\$0.35	–\$0.34	–\$0.36
ε	\$1.16	\$1.04	\$1.13
f	\$1.40	\$1.21	\$1.21
p	–\$2.27	–\$1.42	–\$1.51
CVR	–\$0.06	\$0.49	–\$0.47
Uncertainty	\$0.01	\$0.01	\$0.01

In the base geometry, there is little spatial variation of the power by fuel pin because of the relatively homogeneous geometry. In the 'clustered-rod' designs, there is significantly higher power in the outer pins and a very strong spectral change by fuel pin row. The outer pins have a

very soft spectrum that doesn't change much with coolant voiding. The inner pins have a much harder spectrum that changes significantly when the coolant voids because the coolant is an important moderator in this region.

By introducing a spatial distribution of fuel enrichments and poison, the spatial distribution of the change in spectrum can be utilized to reduce the CVR. In Table 5.8, the results of using a spatially dependent distribution of ^{235}U enrichment and erbium poison are presented. The enrichment in the inner pins has been decreased from 14 to 10%, the enrichment in the outer row of pins has been increased from 14 to 19%, and all of the poison has been placed in the central rod (1.26 and 1.33 g/cm^3 for "3 Rows–3 Clusters" and "4 Rows–3 Clusters," respectively), rather than equally distributed among all pins. The multiplication factors in Table 5.7 could not necessarily sustain an 18-month cycle length; therefore, poison was removed and the target multiplication factor was set at a value of 1.25.

Table 5.8. Four-factor analysis with space-dependent enrichment and poison distributions

Spatial distribution of erbium and fuel	Base geometry	3 Rows 3 Clusters	4 Rows 3 Clusters
k_{cool}	1.24	1.26	1.23
η	–$0.17	–$0.69	–$0.44
ε	$0.90	$1.02	$1.04
f	$1.40	$1.08	$1.21
p	–$2.05	–$1.38	–$1.69
CVR	$0.08	$0.03	$0.03
Uncertainty	$0.01	$0.01	$0.01

When there was no spatial distribution of poison or enrichment, the reproduction factor (η) was similar for each configuration and negative because of the erbium resonance in the thermal range. When a distribution of poison and enrichment was utilized, the large spectral shift on the interior of the cluster increased the fraction of thermal neutrons in the interior pins, especially the poisoned central rod, which significantly decreased the reproduction factor (η). This created a 'clustered-rod' configuration with a multiplication factor and CVR that is similar to the poisoned base geometry.

5.7.3 Parfait Core

Based on previous work with fast reactors [Ducat, 1974], it is well understood that as the surface area to volume of a core increases (a pancake design for instance), the effect of voiding decreases because the neutrons that would have been absorbed in the coolant, but are no longer, are more likely to leak from the core. However, it is difficult for a high-leakage core design to have a high power level without being excessively large in any dimension (diameter for a pancake design).

One option for a high-leakage core design that has a high power level is the parfait core. This design segregates the core into a series of axial layers (pancakes) separated by high BP regions. Each individual fuel layer is neutronically separated from the other fuel layers by poison layers. This leads to a set of 'pancake' cores that leak many neutrons into the poisoned

region. If a higher power level is desired, additional 'pancakes' may be added. When the coolant voids, the neutrons are less likely to be absorbed in the salt but more likely to stream into the poisoned region. The harder spectrum, due to a loss of moderation, will also increase the absorption in the resonances of the poison and ^{238}U, thus lowering the CVR.

The KENO 3-D, multigroup, stochastic transport code was used with the doubly heterogeneous fuel option to study the effects of axial layering of high burnable-poison fuel with fuel that contains low levels of BP to create a 'parfait' core. This effectively creates a core that is composed of several high-leakage pancake cores. When the leakage is increased, the CVR is substantially reduced. For this analysis, the amount of BP in the fuel compacts varied by about a factor of 100 between the "poison" layers (~1 g erbium per compact) and the "fuel" layers (~10 mg erbium per compact).

The results show significant improvement in the CVR with the baseline coolant (Flibe–99.995% enriched ^{7}Li) using Er_2O_3 poison in the compact matrix. An 11-block tall active core (8.754 m) was considered, and the concentration of Er_2O_3 in both the poison and fuel blocks was adjusted to produce a comparable eigenvalue in each core configuration (reflecting boundaries were used radially and vacuum boundaries were used axially). As shown in Table 5.9 (a single layer of fuel), the CVR is significantly reduced when the core becomes flatter with more leakage.

Table 5.9. Single-layer parfait core reduces the CVR as the leakage increases

Cooled eigenvalue	1.259	1.249	1.255	1.259
Voided eigenvalue	1.265	1.254	1.258	1.257
CVR ($)	$0.54	$0.46	$0.27	–$0.19
1	Reflector	Reflector	Reflector	Reflector
2	Fuel	Poison	Poison	Poison
3	Fuel	Fuel	Poison	Poison
4	Fuel	Fuel	Poison	Poison
5	Fuel	Fuel	Fuel	Poison
6	Fuel	Fuel	Fuel	Fuel
7	Fuel	Fuel	Fuel	Fuel
8	Fuel	Fuel	Fuel	Fuel
9	Fuel	Fuel	Fuel	Poison
10	Fuel	Fuel	Poison	Poison
11	Fuel	Fuel	Poison	Poison
12	Fuel	Poison	Poison	Poison
13	Reflector	Reflector	Reflector	Reflector

Similar analyses were performed with multiple layers, and the best results are shown in Table 5.10. The CVR is very negative using 2 to 3 layers of fueled blocks with no more than two fuel blocks axially per layer. This will have a substantial effect on the power distribution and possibly the stability of the core, but has been shown to significantly reduce the CVR. This design option may be required if a coolant salt with less favorable neutronic properties is selected for use in the LS-VHTR.

Table 5.10. Parfait core designs with a strongly negative CVR

Cooled eigenvalue Voided eigenvalue	1.250 1.240	1.250 1.241	1.250 1.241
CVR ($)	–$0.94	–$0.83	–$0.88
1	Reflector	Reflector	Reflector
2	Poison	Poison	Poison
3	Poison	Poison	Fuel
4	Fuel	Fuel	Fuel
5	Fuel	Fuel	Poison
6	Poison	Poison	Poison
7	Poison	Fuel	Fuel
8	Poison	Poison	Poison
9	Fuel	Fuel	Poison
10	Fuel	Fuel	Fuel
11	Poison	Poison	Fuel
12	Poison	Poison	Poison
13	Reflector	Reflector	Reflector

The effect of layering with the 'clustered-rod' design will be more substantial due to the closer proximity of the coolant and fuel. Therefore, the continued analysis of this design may prove to couple the benefits of BPs, 'clustered-rod' configurations, and a parfait core to design a LS-VHTR core with a strongly negative CVR.

5.8 IMPACT OF FLIBE MOLAR RATIO

The neutronic performance of Flibe was further evaluated to determine if a more optimal molar ratio of the LiF and BeF_2 salt components might produce an even a stronger negative void coefficient. The baseline Flibe mixture is ^{2}LiF-BeF_2 with a 2:1 molar ratio between the two salt constituents, LiF and BeF_2. Parametric studies were performed with different Flibe molar ratios including 1:1 (49.8% LiF and 50.2% BeF_2) and 1:3 (25.1% LiF and 74.9% BeF_2) ratios. In addition, 100% LiF and 100% BeF_2 mixtures were also evaluated, but only for neutronic interest and not as practical liquid salt mixtures. Table 5.11 gives some liquid salt characteristics [Janz, 1992] for Flibe as a function of molar ratio.

Neutronic evaluations were performed using the density data along with the 941.83 g ^{235}U per block uniform core loading, 15 wt % enrichment, TRISO-coated particle PF=0.28, 1100°C fuel temperature, 750°C liquid-salt temperature, and the reference LS-VHTR geometric prismatic fuel block details in the MCNP 1/12-core model.

Calculated void coefficient results are plotted in Fig. 5.13 and clearly show that molar ratios of Flibe weighted in favor of the BeF_2 produce more negative void coefficients. This is, of course, due to the superior moderating properties of the beryllium relative to both the lithium and bulk graphite in the fuel blocks. Again, the negative void coefficients become larger in magnitude with increasing coolant channel radius for the beryllium-containing Flibe mixtures.

It is interesting to note that the 1:1 and 1:3 Flibe mixtures have melting points at 363 and 515°C, respectively [McDonald, 2005;Naka, 2003]. The 2:1 Flibe has a melting point of approximately 460°C. The lower melting point of the 1:1 Flibe represents a nearly 100°C

advantage over the 2:1 reference mixture. However, the higher BeF_2 content creates other challenges, such as an increase in the viscosity of the liquid-salt coolant.

Table 5.11. Liquid salt characteristics for Flibe as a function of molar ratio

Flibe liquid salt	Approxmate molar ratio	Actual molar ratio (%)	Melting temperature (°C)	Density* (g/cm^3)
100% LiF	1:0	100:0	–	1.85655
LiF—BeF_2	2:1 (ref)	66.6:33.4	460	1.94298
LiF—BeF_2	1:1	49.8:50.2	363	1.91518
LiF—BeF_2	1:3	25.1:74.9	515	1.91347
100% BeF_2	0:1	0:100	–	1.95716

*Density at 750°C.

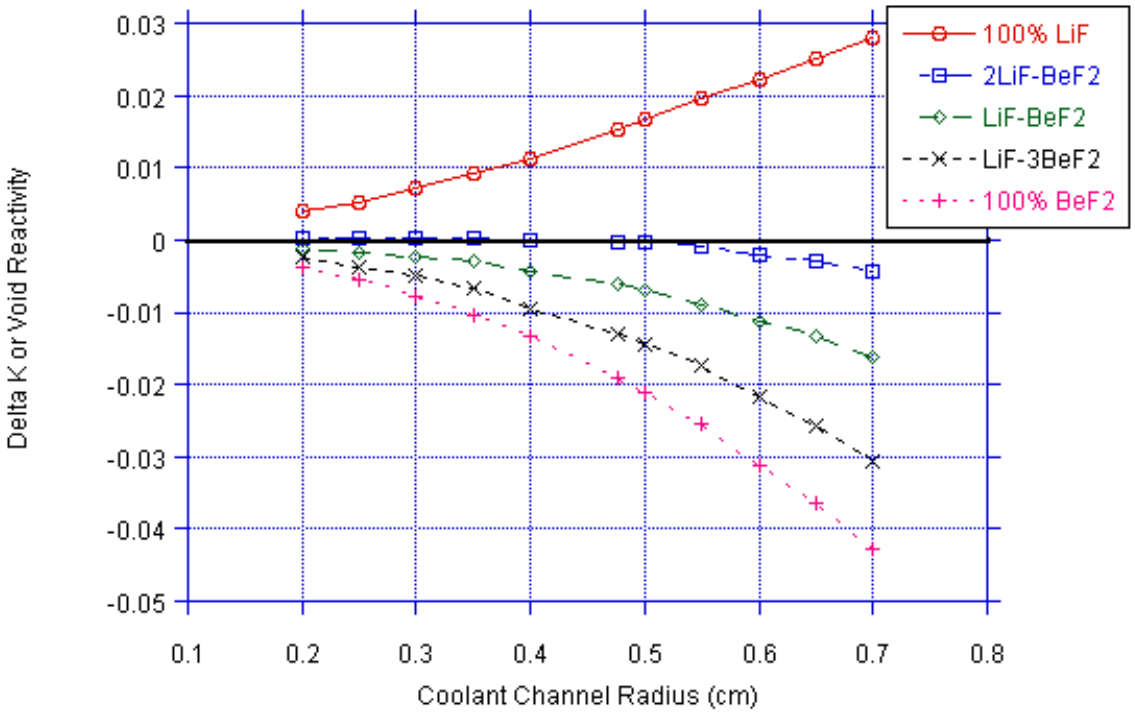

Fig. 5.13. Void reactivity (Δk) as a function of coolant channel radius and molar ratio of LiF and BeF_2.

5.9 CONCLUSIONS ON COOLANT VOID REACTIVITY

The LS-VHTR has very similar neutronics performance as the gas-cooled VHTR, especially for Flibe because it appears relatively transparent to the neutrons (i.e., its moderation and absorption characteristics are nearly balanced). However, in the initial baseline LS-VHTR, a loss of coolant would lead to a slight reactivity insertion. Consequently, the coolant void

reactivity of the LS-VHTR was evaluated as function of several design and operational parameters, including burnup, BP, core geometry, and coolant isotopics.

First, it was found that the CVR becomes more negative with burnup, suggesting that the CVR could be negative at the beginning of cycle with a multibatch core, except for the initial start-up core. In this case, additional measures would be necessary to ensure a negative CVR at beginning of life. Flibe was found to produce a strong negative void coefficient of reactivity for uranium block loadings needed to achieve an 18-month power cycle length for the 10-ring LS-VHTR at 2400 MW(t) power. Also, for these block loadings (900-1, 200 g ^{235}U per block) the uranium enrichments were in the desirable range of 10–20 wt %.

The LS-VHTR was shown to have a very high fuel temperature reactivity feedback due to the Doppler effect, which decreases the likelihood of fuel failure during a coolant voiding scenario. The fuel temperature reactivity is 2 orders of magnitude greater than traditional LWRs. Even in the base LS-VHTR design, with the simple addition of erbium BP, the Doppler effect would result in a zero net change in reactivity due to voiding with a 10^{o}C rise in fuel temperature. Therefore, no realistic voiding scenario could occur that would lead to an increase in reactivity of such magnitude that the increase in fuel temperature would not quickly lead to a subcritical core.

The use of BPs showed that the spectral shift in the flux can be utilized to increase the absorption in the BP resonances when the coolant voids. Among the several candidate BPs, erbium makes the CVR more negative, especially at zero burnup. This is because of the proximity of the erbium absorption cross section resonance peak to the neutron spectrum peak in the low energy range. Modification of the fuel element dimension (spectral change) was another approach that was found to reduce the CVR.

It was observed that a larger coolant hole compared to that of the baseline LS-VHTR design makes the CVR more negative because a harder spectrum increases the absorption rate in ^{238}U. The larger coolant channel is very desirable from a thermal hydraulic standpoint because the pumping power required to move the coolant across the core can be reduced, and because the larger coolant hole results in lower fuel temperatures. Also, a larger Flibe inventory in the core provides a larger thermal mass to deposit heat under transient conditions. There is, however, a penalty on the cycle length due to the poisoning effect of the coolant.

The homogeneous distribution of fuel compacts in a regular, hexagonal lattice within the fuel blocks can be modified to a ‘clustered-rod’ design. The clustered-rod design, a tight-pitch array of fuel rods within a single coolant channel surrounded by the graphite block, simplifies refueling by creating a set of assemblies that are removed like present-day LWRs and increases the heat exchange between the coolant and fuel, which improves thermal performance and decreases the fuel temperature response time (Doppler effect) during an accident scenario. The clustered-rod design did not appear to significantly reduce the CVR but could be configured to have a low CVR similar to the baseline design because of the spatial distribution of the spectral change during a voided coolant scenario.

In addition, the CVR can be reduced by introducing axial layering of the fuel blocks. The large LS-VHTR core can be split effectively into multiple thin pancake cores, each having large neutron leakage rates into the high-poison layers between the pancakes. This parfait-type core design was studied as a function of the number of core layers. It was determined that the most negative CVR occurs with two nonpoised fuel layers. Additional work is necessary to determine

the effect of such a heterogeneous axial power distribution on the stability of the neutron flux spectrum due to xenon perturbations.

Finally, it was also found that increasing the molar fraction of the BeF_2 component in the Flibe salt leads to more negative void coefficients of reactivity. For a 1:1 molar ratio, or equal parts LiF and BeF_2, more negative void coefficients could be realized over the reference 2:1 molar ratio Flibe and, in addition, a 100°C reduction in melting point could be achieved. Hence, the 1:1 Flibe can potentially improve the void coefficient neutronics and reduce the temperature required to maintain the Flibe salt in the liquid state. Unfortunately, the impact of the change in molar concentration on the thermo-physical properties of the binary salt, especially a significant increase in viscosity, will likely preclude this option.

This page intentionally blank

6. SAFETY PERFORMANCE

Thermal-hydraulic analyses were performed to evaluate the safety characteristics of the LS-VHTR. A one-dimensional model of the LS-VHTR was developed using the RELAP5-3D computer program [INEEL, 2003]. The thermal calculations from the one-dimensional model of a fuel block were benchmarked against a multidimensional ABAQUS model [Hibbitt, 2005]. The RELAP5-3D model was then used to simulate a transient initiated by LOFC in which the RVACS passively removed decay heat. Parametric calculations were performed to investigate the effects of various parameters, including bypass flow fraction, coolant channel diameter, the number of fueled rings in the core, and the coolant outlet temperature. Additional parametric calculations investigated the effects of an enhanced RVACS design, failure to scram, and radial/axial conduction in the core.

6.1 RELAP5-3D MODEL

The RELAP5-3D model of the LS-VHTR is illustrated in Fig. 6.1. The model represents the portion of the primary coolant system within the reactor vessel and the RVACS. The primary coolant is represented by Components 120 through 290. The inlet plenum is represented by Components 120 through 140. The core is represented by Components 151 through 156. The ten fueled rings in the design are simulated with six channels in the model. The inner two high-powered rings are modeled explicitly with Components 151 and 152. The remaining eight rings are represented with four channels (Components 153 through 156), each of which represents two rings in the design. The outer eight rings were combined into four channels so that the effects of radial and axial conduction between prismatic blocks in the core could be simulated. Parametric calculations to be discussed later showed that the effects of conduction between blocks were small in the LS-VHTR. Consequently, each fueled ring could be modeled explicitly if desired. Each of the core channels is modeled with 12 axial control volumes. The upper and lower control volumes represent the axial reflectors. The other ten volumes represent the active core region.

The outlet plenum is modeled with Component 170. Component 290 simulates the inlet lines to the reactor vessel while Component 205 simulates the coolant risers, which connect the outlet plenum and the heat exchangers. The heat exchangers and pumps are not modeled explicitly, but their effects are modeled with boundary conditions of flow in Component 285, temperature in Component 280, and pressure in Component 215. The flow area of the coolant risers is based on that of eight hexagonal blocks in the outer reflector. Preliminary calculations performed based on an area of two blocks resulted in a pressure drop that significantly exceeded that of the core.

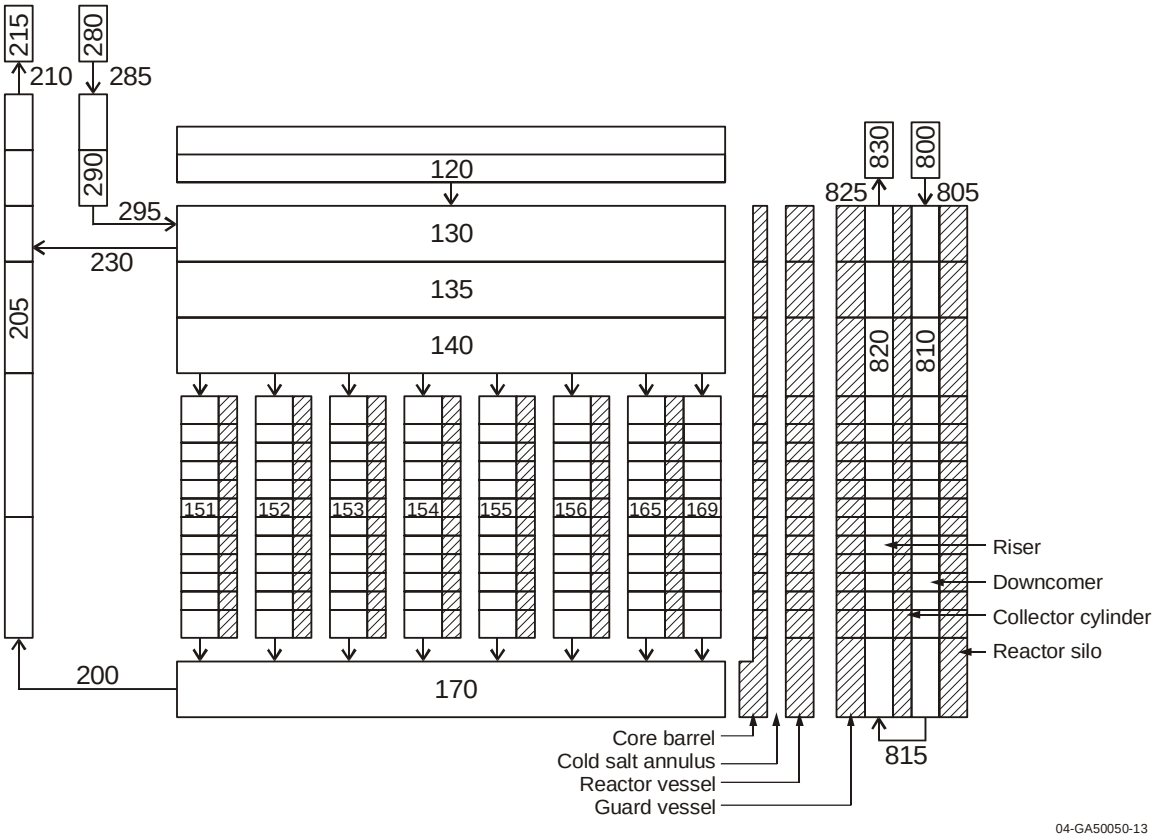

Fig. 6.1. RELAP5-3D model of the LS-VHTR.

The model simulates a thermal blanket system that consists of a core barrel and an annulus filled with cold salt. The thickness of the annulus was set to limit the reactor vessel temperature in the inlet plenum to 750°C during normal operation, assuming that conduction was the only heat transport mechanism through the salt. Additional insulation, assumed to be graphite, was required to limit the reactor vessel temperature near the outlet plenum, which was 100°C hotter than the inlet plenum. An engineered bypass path (Component 169) was used to heat the reactor vessel to near 750°C in the core region. The engineered bypass path consists of a small gap between the outer reflector and the core barrel. Two other bypass paths around the core are represented. These bypass paths include the gaps between the fuel and reflector blocks (Component 165) and a siphon breaker between the inlet plenum and the coolant riser (Component 230).

Heat structures are used to represent the core barrel, the reactor vessel, and the prismatic blocks in the core and the upper, lower, and outer reflectors. The radial power profile in the core is based on the results shown previously in Fig. 3.3. The maximum radial power peaking factor is 1.41 and occurs in the innermost ring (Component 151). Component 155, which represents the seventh and eighth fueled rings, approximates an average channel as it has a radial power peaking factor of 0.98. The axial power profile is based on a profile used for the gas-cooled VHTR [MacDonald, 2003] and is bottom skewed with a peak value of 1.38. The use of a bottom-skewed power profile results in higher fuel temperatures than a symmetric power profile

with the same peak value because the power is shifted towards the bottom of the core where the coolant temperatures are higher.

The reactor power is calculated with a point kinetics model. The decay heat is calculated from the ANS-5.1 standard [ANS, 1979] for the infinite operation of ^{235}U. The total decay heat determined from the ANS-5.1 standard was about 30% greater than detailed heat calculations performed specifically for the gas-cooled VHTR [MacDonald, 2003]. Since the decay heat calculations performed for the gas-cooled VHTR are expected to be applicable for the LS-VHTR, the decay heat assumed here has a significant amount of conservatism.

The RVACS is represented by Components 800 through 830. The air supply and exhaust are represented with two time-dependent volumes, Components 800 and 830, which are set at atmospheric pressure. The RVACS downcomer and riser are represented by Components 810 and 820, respectively. The model represents all the major heat structures associated with the RVACS, including the reactor and guard vessels and the collector cylinder that separates the downcomer and the riser. Radiation enclosure models are used to represent the heat transfer between the reactor and guard vessels and between the guard vessel and the collector cylinder. The emissivity of these surfaces was set to 0.75, which is representative of the average measured value during the Power Reactor Inherently Safe Module (PRISM) test program [Hunsbedt, 1988]. The convection and conduction of the inert gas in the gap between the reactor and guard vessels was neglected. The outside surface of the collector cylinder was insulated to prevent preheating of the cold air flowing down the downcomer.

The RVACS model is based on the PRISM design [GE, 1986]. In the PRISM design, the hot and cold air columns were significantly longer than the length of the reactor vessel. However, details of the inlet and outlet air ducts were not provided. These inlet and outlet air ducts were neglected to simplify the model. The model was adjusted to represent RVACS performance during emergency operation in the PRISM test program. Adjustments included setting the form loss coefficient at the bottom of the downcomer (Component 815) to 0.26 and reducing the heat transfer coefficient on the outer surface of the guard vessel and the inner surface of the collector cylinder by 20% using a fouling factor. The resulting model predicted the mass flow rate of air and the total power removed during emergency operation within 10%. The model was then modified to represent the LS-VHTR geometry by increasing the diameter and height of the reactor vessel. The thicknesses of the guard vessel, riser, collector cylinder, and downcomer were based on the PRISM values.

The geometry for the RELAP5-3D model of the LS-VHTR is summarized in Table 6.1. Note that the inner vessel diameter was modeled more than 1 m smaller than the baseline model, which produces an outer reflector that is approximately 0.5 m thinner than the baseline. This resulted in a lower amount of decay heat being removed from the system during the transients because of a lower bypass flow. This modeling conservatism is in addition to the 30% conservatism introduced by using the ANS-5.1 standard for decay heat. Future analyses will focus on best-estimate calculations.

Table 6.1. Geometrical parameters of the LS-VHTR used in RELAP model

Parameter	Value
Core:	
Coolant channel diameter, mm	9.53
Fuel compact diameter, mm	12.45
Fuel channel diameter, mm	12.70
Fuel channel pitch, mm	18.8
Number of coolant channels per block	108
Number of fuel channels per block	216
Number of fuel columns	265
Flat-to-flat distance of hexagonal block, mm	360
Gap between hexagonal blocks, mm	1
Heated length, m	7.93
Length of upper and lower reflectors, m	1.19
Thickness of outer reflector, m	0.834
Thermal blanket system:	
Gap between outer reflector and core barrel, mm	5
Core barrel inner diameter, m	7.952
Core barrel thickness, mm	25
Cold salt annulus thickness, mm	9
Outlet plenum graphite insulation thickness, mm	180
RVACS:	
Reactor vessel inner diameter, m	8.02[a]
Reactor vessel thickness, m	0.10
Gap between reactor and guard vessels, m	0.20
Guard vessel thickness, m	0.025
Riser gap thickness, m	0.178
Collector cylinder thickness, m	0.0254
Collector cylinder insulation thickness, m	0.0508
Active heat transfer length, m	18.4

[a]Outer reflector was modeled ~0.5 m thinner than baseline design.

The RELAP5-3D model was used to determine the steady-state operating conditions for the LS-VHTR. The results of the steady-state calculation are presented in Table 6.2. The table also includes results presented in the 2004 LS-VHTR study [Ingersoll, 2004]. Some of the parameters vary significantly. For example, the average and peak fuel temperatures are, respectively, 43 and 156°C higher this year. These differences prompted the thermal analysis described in the Sect. 6.2. The higher fuel temperatures this year were caused by several factors. First, the power density in the core was higher because this year's core contained 265 fuel columns while last year's core contained 324. Second, a lower graphite thermal conductivity was used this year to account for the effects of irradiation. As shown in Fig. 6.2, irradiation initially causes a large decrease in the thermal conductivity, but the effects of continued irradiation disappear after the fast fluence exceeds 3×10^{25} n/m^2. The thermal conductivity used in the RELAP5-3D model is based on the lowest curve shown in Fig. 6.2, which applies to the radial orientation of H-451 graphite after a fast fluence of 10×10^{25} n/m^2. This amount of irradiation reduces the thermal conductivity of the graphite by 40% at 1000°C. As described in the next section, the one-dimensional heat-conduction model used this year results in higher fuel temperatures than the model used last year, but this year's model is in good agreement with a detailed finite-element calculation. Finally, the maximum radial peaking factor was increased from 1.20 to 1.41, which caused a further increase in the maximum fuel temperature. This year's maximum fuel temperature exceeds the steady state limit of 1250°C. The maximum fuel temperature can be reduced by various means, such as decreasing the reactor power or lowering the coolant inlet temperature.

Table 6.2. Initial conditions for the LS-VHTR at rated power

Parameter	Value	
	2004 results	**RELAP5-3D**
Core power, MW	2400	2400
Mass flow rate, kg/s	12,070	10,264
Core inlet temperature, °C	900	900
Core outlet temperature, °C	1000	1000
Average fuel temperature, °C	1050	1093
Maximum fuel temperature, °C	1168	1329
Maximum RV temperature, °C	750	750
Total bypass, %	20	12.0
Gaps between blocks, %		4.4
Engineered bypass, %		5.6
Siphon breaker, %		2.0
Core pressure drop, MPa	0.129	0.211
Vessel pressure drop, MPa		0.276
RCCS/RVACS heat removal, MW	15[a]	6.2[b]

[a]Water-cooled RCCS.
[b]Air-cooled RVACS.

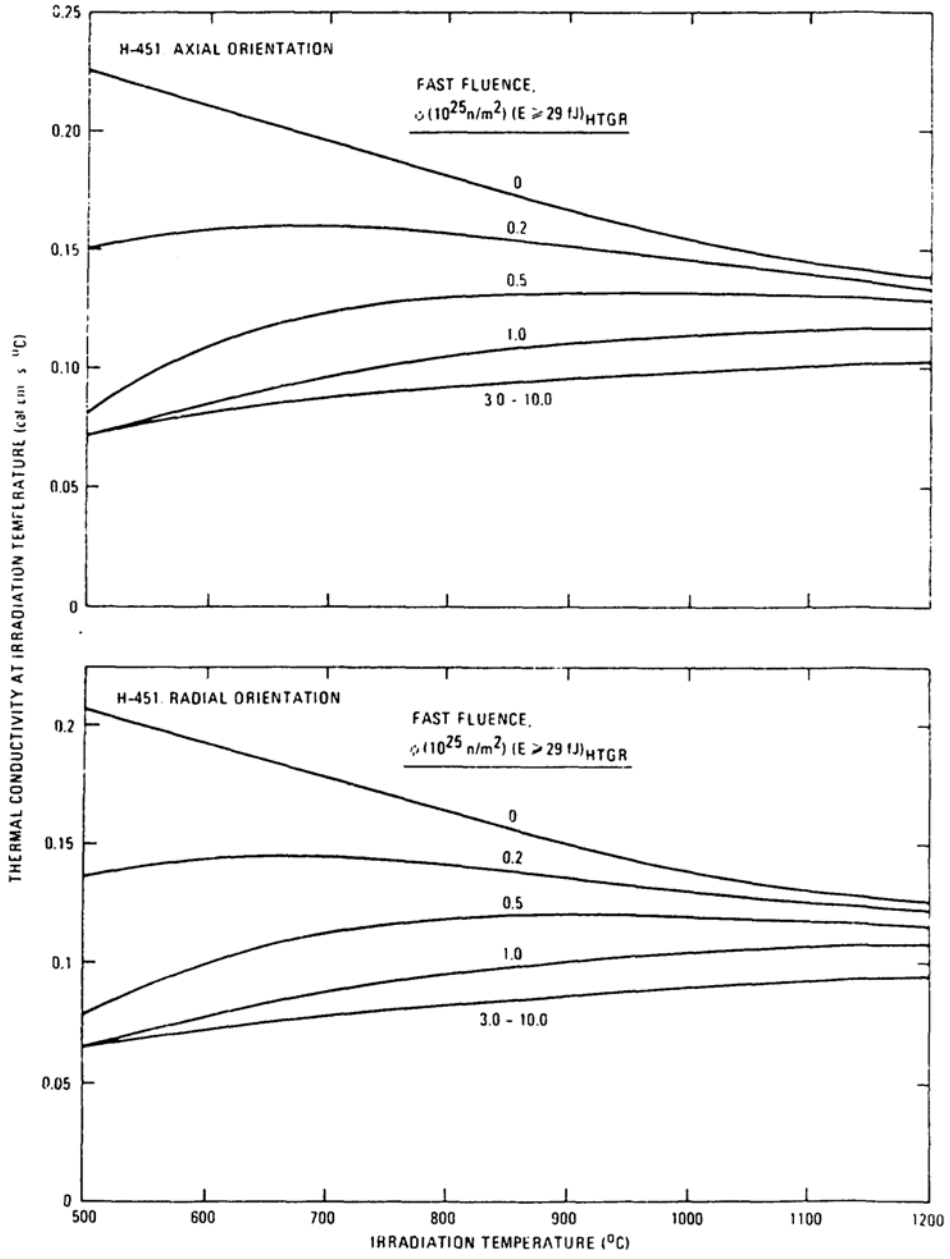

Fig. 6.2. The effect of irradiation on the thermal conductivity of H-451 graphite [GA, 1977].

Table 6.2 also shows that the heat removed by the RVACS is less than half of last year's value, which was based on a GT-MHR design with a water-cooled reactor cavity cooling system. The outer surface of the reactor vessel in the 2004 study was able to radiate directly to the water-filled riser pipes of the RCCS. With the present RVACS model, the reactor vessel has to radiate first to the guard vessel and then a significant fraction of the heat has to radiate to the collector cylinder. The extra radiation path and the heat transfer to air added significant thermal resistances that reduced the power removed in this year's calculations. A task is planned for next year to evaluate various passive decay heat removal systems.

Table 6.2 shows that the core pressure drop was significantly higher in this year's calculation. This difference is believed to be caused by the different number of fuel columns used in this year's analysis. An increase in the number of fuel columns from 265 to 324 would have reduced this year's pressure drop by about 33%, which would have been in reasonable agreement with last year's value. The difference in bypass flow rates is simply due to different assumptions.

6.2 STEADY-STATE TEMPERATURE DISTRIBUTION

The RELAP5-3D model of the fuel block is based on a one-dimensional representation of a unit cell. Figure 6.3 shows a unit cell, which contains one coolant channel, 120° segments from the six surrounding fuel channels, and the intermediate graphite matrix. The unit cell effectively contains one coolant channel and two fuel channels. The gap between the fuel channel and the fuel compact was assumed to be filled with helium. The corresponding one-dimensional heat structure utilized annular geometry as shown in the figure. The inner radius of the heat structure was set to the radius of the coolant channel and the thickness of the graphite ring preserved the volume of the graphite. Similarly, the thicknesses of the helium and fuel rings preserved the volume of the corresponding regions in the unit cell. An additional annular region was modeled outside the fuel region to account for the graphite not contained within any unit cell, such as that near the periphery of the block.

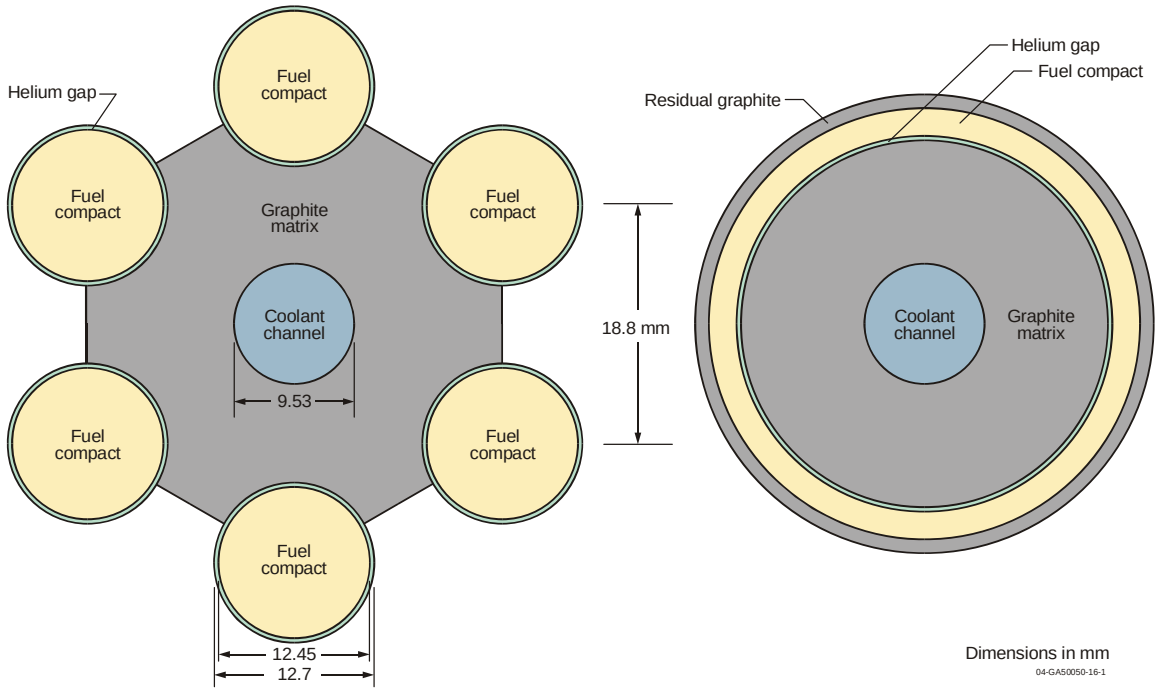

Fig. 6.3. RELAP5-3D model of a unit cell in a fuel block.

The annular model used in this analysis resulted in a fuel ring thickness that was significantly smaller than the diameter of the fuel compact. The thermal conductivity of the fuel was multiplied by a factor of 0.324 in the one-dimensional model to compensate for the smaller thickness. This factor was obtained from a comparison of the exact solution for the temperature

rise across a cylinder with the exact solution for the temperature rise across an annulus with an outer adiabatic surface. The exact solutions utilized uniform volumetric heat generation rates and constant thermal conductivities. The use of the annular geometry also resulted in a thinner helium gap and more heat transfer area in the gap than in the actual design. The thermal conductivity of the helium was multiplied by a factor of 0.742 in the one-dimensional model to compensate for the distortion in geometry. This factor was obtained from a comparison of the exact solutions for the temperature rise across the helium gap in the fuel channel and in the one-dimensional model assuming constant thermal conductivity.

A comparison of this result to the results from the 2004 study [Ingersoll, 2004] revealed significant differences in the modeling of the graphite matrix. The previous model utilized a graphite thermal conductivity of 60 W/m-K, which is representative of unirradiated H-451 graphite. The results from this study were based on irradiated graphite, which reduced the thermal conductivity (see Fig. 6.2). There were also differences in the representation of the geometry of the graphite matrix. This year's model used an annular representation of the graphite as described previously. The resulting graphite thickness was representative of an average distance between the fuel and coolant channels. Last year's model used a rectangular representation based on the minimum distance between the fuel and coolant channels. The heat transfer area in the unit cell varies between a minimum that is based on the wetted perimeter of one coolant channel to a maximum that is near that calculated from the wetted perimeter of two fuel channels. Since the selection of an optimal heat transfer area to use in a one-dimensional model is not obvious, detailed finite-element calculations were performed with the ABAQUS computer code [Hibbitt, 2005].

The ABAQUS model represented a 60° segment of the unit cell as shown in Fig. 6.4. All boundaries in the ABAQUS model were adiabatic except for that of the coolant channel, located in the lower left corner of the figure, which was modeled with boundary conditions of heat transfer coefficient and sink temperature. The helium gap was modeled as a heat conducting region. Convection and radiation were neglected. The ABAQUS model represented the outlet of an average-powered fuel column in last year's design. To accomplish this, the heat transfer coefficient and fluid sink temperature were set at 13,000 W/m^2-K and 1000°C, respectively. The thermal conductivities of the graphite, helium, and fuel compact were 60, 0.44, and 10 W/m-K, respectively. A uniform volumetric heat generation rate in the fuel compact of 44.28 MW/m^3 was applied. A RELAP5-3D model simulating these same parameters was developed for comparison. The RELAP5-3D results presented in Fig. 6.5 were generated using constant thermal properties, whereas the results presented previously in Table 6.2 and later in Sect. 6.3 were generated using temperature-dependent thermal properties.

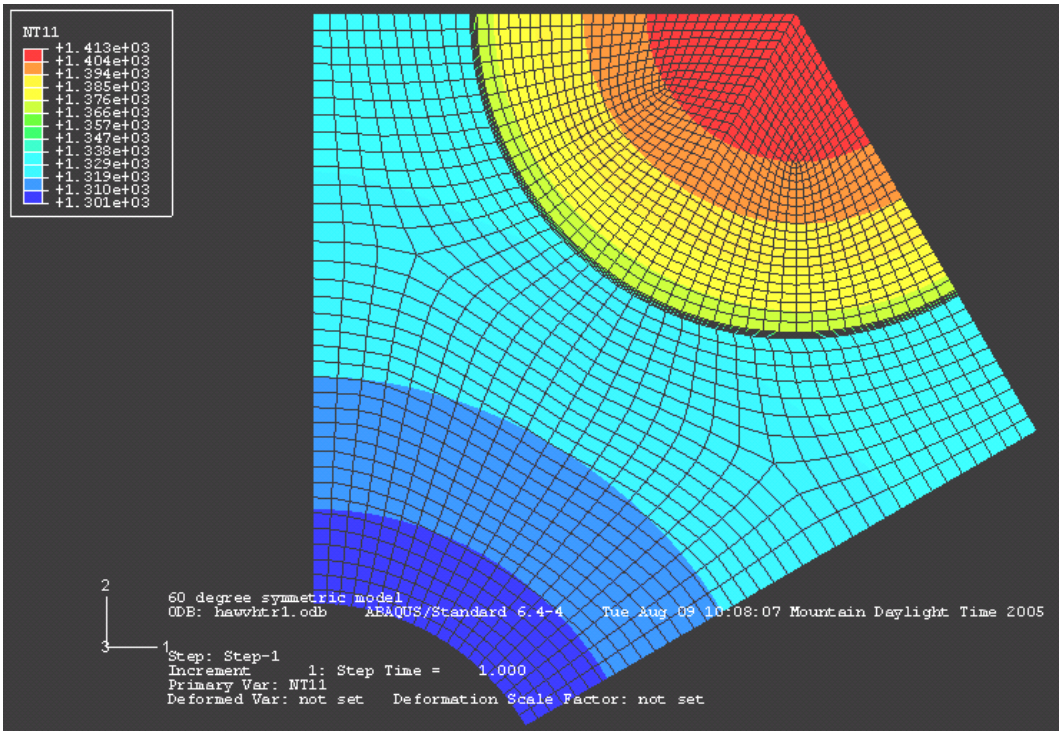

Fig. 6.4. ABAQUS model of a unit cell in a fuel block of the LS-VHTR (temperatures shown in legend are in units of degrees-Kelvin).

Figure 6.5 compares the temperatures in the unit cell calculated in the 2004 study with those calculated this year with RELAP5-3D and ABAQUS. The abscissa of the figure corresponds to a straight line connecting the center of the coolant and fuel channels. The increase in temperature near 4.8 mm corresponds to the thermal resistance associated with the heat transfer coefficient at the surface of the coolant channel. The temperature rise near 12.5 mm in the 2004 and ABAQUS calculations and near 14.7 mm in the RELAP5-3D calculation corresponds to the thermal resistance of the helium gap. The temperature rises between the fluid and the wall and across the fuel compact were nearly the same in all three calculations. The largest difference between calculations was in the temperature rise across the graphite compact. The temperature difference across the graphite was about 60% larger in RELAP5-3D and ABAQUS than in the 2004 calculation. The temperature difference across the helium gap was about 20% larger in the RELAP5-3D and ABAQUS calculations, probably because of the use of a different helium thermal conductivity than in the 2004 calculations.

The centerline fuel temperature calculated by RELAP5-3D was 1.3°C higher than the corresponding value calculated by ABAQUS. Additional calculations were performed in which the volumetric heat generation rate was varied between 20.27 and 82.29 MW/m^3, corresponding to the minimum and maximum power locations in the 2005 core design during normal operation. The fuel centerline temperatures calculated by RELAP5-3D were within 0.6 and 2.2°C, respectively, of the values calculated by ABAQUS. Thus, the RELAP5-3D one-dimensional annular model can accurately predict fuel centerline temperatures given the correct thermal properties.

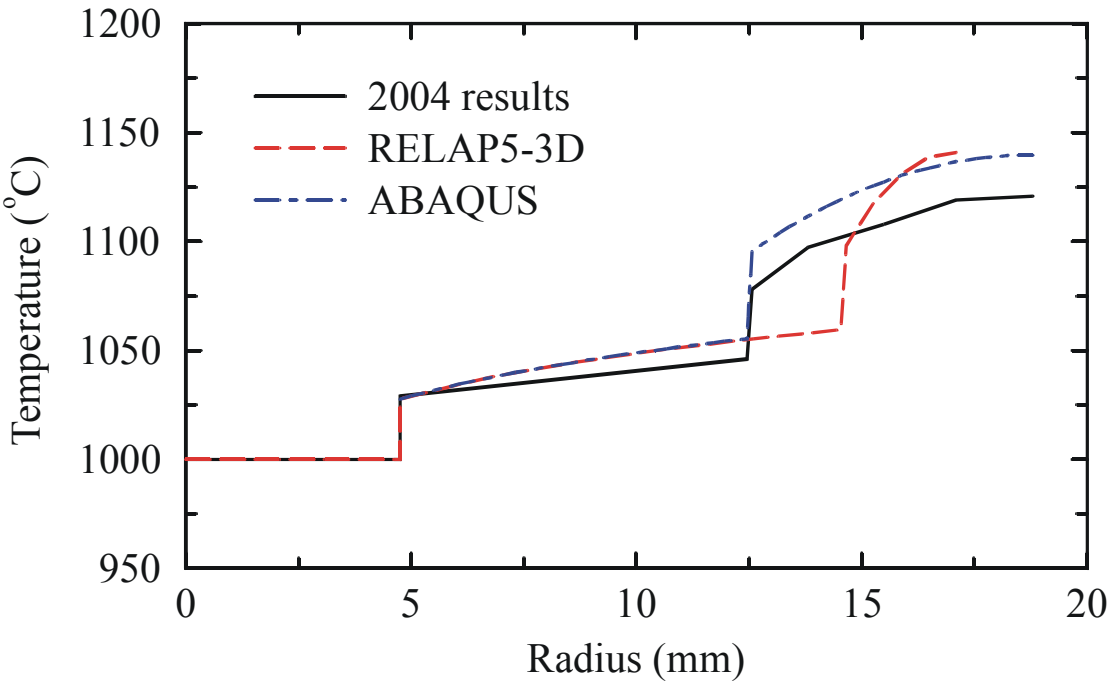

Fig. 6.5. A comparison of calculated temperatures in a unit cell of a fuel block.

6.3 LOFC TRANSIENT

The RELAP5-3D model was used to simulate a transient initiated by LOFC. The transient was simulated by linearly reducing the flow in Component 285 to zero in 10 s. The reactor scram signal occurred at 1 s and the control rods were fully inserted 3 s later, shutting down the reactor. RVACS was assumed to be the only system available to remove decay heat.

This transient was governed by the balance between the decay heat generated in the core and the power removed by RVACS. The dominant heat transport processes were due to natural circulation of the liquid salt within the reactor vessel, conduction through the reactor vessel, radiation between the reactor and guard vessels and the collector cylinder, and then convection from the surfaces of the guard vessel and collector cylinder to the air flowing through the riser of RVACS. Figure 6.6 shows that the decay heat initially exceeded the power removed by RVACS. This imbalance in power generation and removal caused the LS-VHTR to heat up, which increased the heat removal by RVACS, partially due to the increased temperature difference between the reactor and the heat sink and partially due to more effective radiation at increased temperatures. The increased heat removed by RVACS exceeded the core decay power after 61 h, which resulted in a general cooling of the LS-VHTR.

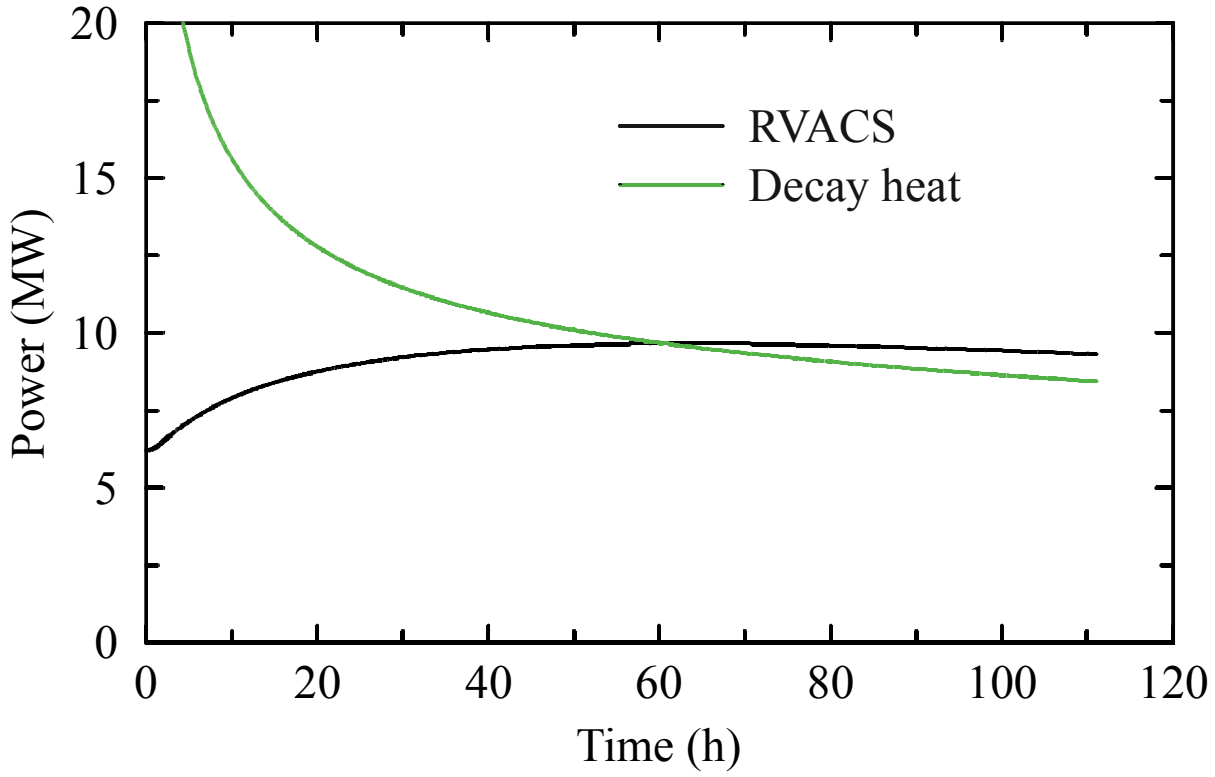

Fig. 6.6. A comparison of RVACS heat removal and core decay power following a LOFC.

The effects of the LOFC on the maximum fuel temperature in the core are shown in Fig. 6.7. The reactor scram caused the maximum fuel temperature to decrease sharply. The fuel temperature then increased following a flow reversal in the core and the transition to natural circulation. The reservoir of cold liquid in the inlet plenum was able to moderate the temperature increase for a few hours. However, the supply of cold liquid was eventually exhausted and the temperature increased due to the imbalance between the power generated in the core and that removed by RVACS. The peak fuel temperature was 1260°C, and occurred near the time that the power removed by RVACS exceeded the decay power. The peak fuel temperature remained well below the boiling limit of 1430°C for Flibe at atmospheric pressure.

The thermal performance of the LS-VHTR is further illustrated in Fig. 6.8. The fluid temperature in the outlet plenum, which supplied liquid to the core after the transition to natural circulation, was generally within 100°C of the maximum fuel temperature. Thus, the axial temperature gradient within the vessel was relatively small, which demonstrates the effectiveness of the natural circulation as a heat transport mechanism. The radial temperature gradient in the core was also relatively small after scram. For example, the differences between fluid and centerline fuel temperatures were generally less than 6°C after scram. The maximum reactor vessel temperature was 985°C and occurred 60 h after the start of the event.

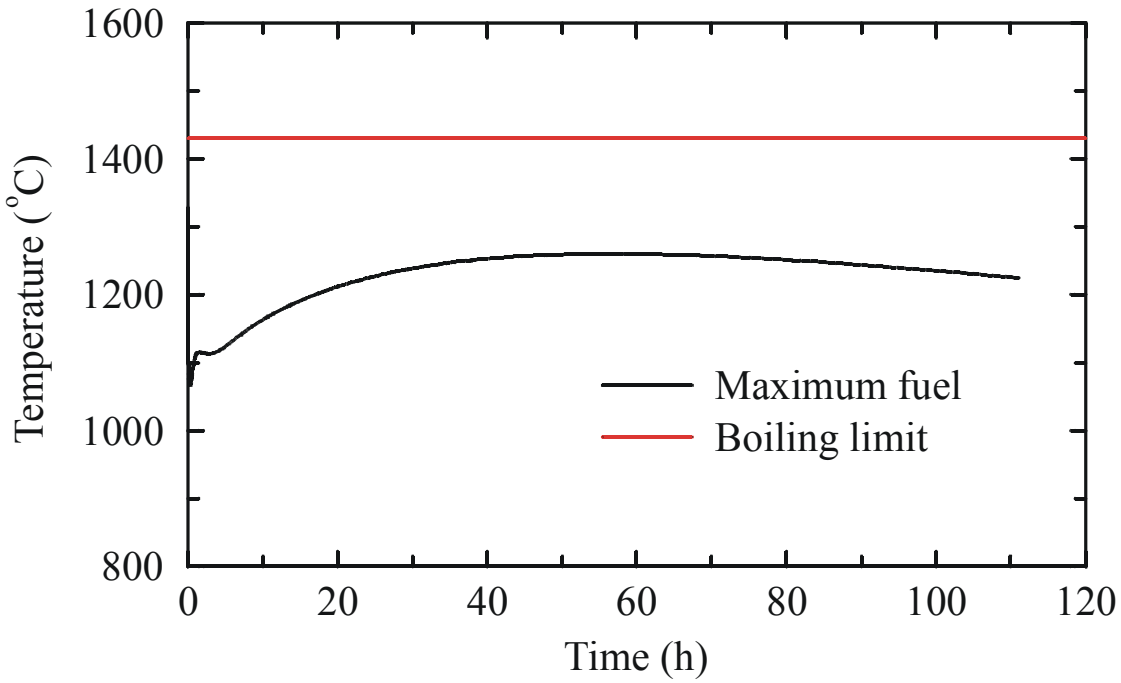

Fig. 6.7. Maximum fuel temperature following a LOFC.

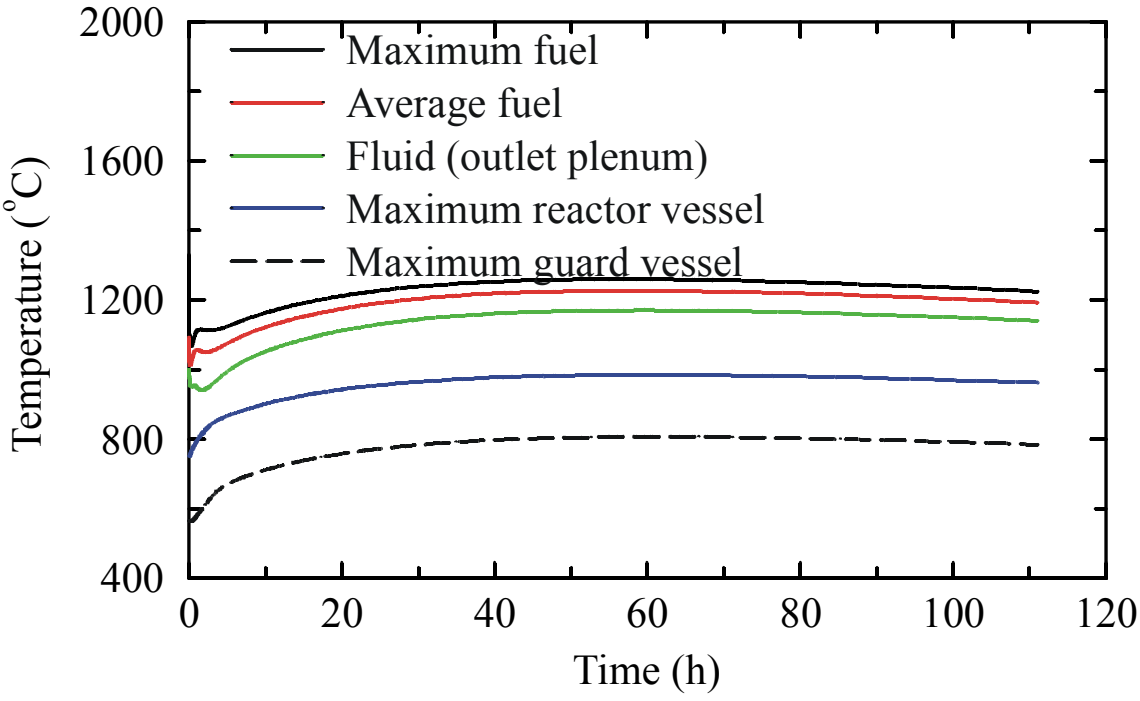

Fig. 6.8. Thermal performance following a LOFC.

The flow patterns within the reactor vessel were fully developed about an hour after the start of the transient. Thereafter, the flow through each of the core channels was upwards. The magnitude of the velocity was consistent with the power distribution, with the highest velocity occurring in the central channel. The principal paths for downward flow were through the engineered bypass path and the coolant riser pipes, which received flow from the siphon breakers.

Analysis of the calculated results showed that radiation heat transfer between the reactor and guard vessels is more effective than conduction through liquid salt. The equivalent thermal conductivity for radiation across the 20-cm gap varies from about 20 to 40 W/m-K, whereas the thermal conductivity of Flibe is only 1.1 W/m-K. Thus, a leak from the reactor vessel could cause the gap to fill with salt, which would significantly degrade the performance of the RVACS if conduction through the salt is the only heat transport mechanism. Evaluations of enclosure heat transfer correlations have been performed [Holman, 1986] that suggest that convection in liquid salt will not be a significant heat transport mechanism between the reactor and guard vessels, but these evaluations are not definitive because the geometry of the RVACS is well outside the database of the correlations. Because liquid salts are transparent, radiative heat transfer through the salts will help mitigate this concern. However, the viability of the RVACS for passive cooling of the LS-VHTR in the presence of a reactor vessel leak will require relevant experiments or more detailed calculations. General Electric [GE, 1986] evaluated the effectiveness of the PRISM RVACS with a leak from the reactor vessel. In PRISM, the effectiveness of the RVACS improved with a leak because of the high thermal conductivity of sodium, about 60 W/m-K. Note that if convection and/or radiation are effective heat transport mechanisms in the LS-VHTR RVACS, the cold salt annulus of the thermal blanket system will not be as effective as assumed here and additional insulation will be required.

6.4 PARAMETRIC STUDIES

Calculations were performed to investigate the sensitivity of the calculated results to various parameters, including the size of the coolant channels, the bypass flow fraction, the number of fueled rings in the core, the coolant outlet temperature, and radial/axial conduction in the core. Additional parametric calculations investigated the effects of an enhanced RVACS design and a failure to scram (discussed in Sects. 6.5 and 6.6). In each case, the calculation was identical to the base calculation described previously except for the identified change. The results of these parametric calculations are described below.

The diameter of the coolant channel was 9.53 mm in the base calculation. Parametric calculations were performed in which the diameter was increased to 11.8 and 14.0 mm. The effects of the coolant channel diameter on the performance of the LS-VHTR are summarized in Table 6.3. The maximum fuel temperature decreased as the channel diameter increased, primarily because of the smaller conduction distance across the graphite. The effect was modest (<25°C) at steady state, where the heat fluxes were relatively large, and small (<5°C) during the transient, where the heat fluxes were relatively small. The diameter had a large effect on the differential pressure across the vessel during normal operation. For example, the differential pressure was reduced by more than 60% with the largest diameter. A corresponding reduction would occur in the required pumping power. The reduction in differential pressure associated with the larger coolant diameter also significantly reduced the bypass flow around the core. The

parametric calculations show that the thermal-hydraulic performance of the design is improved with larger coolant channel diameters.

Table 6.3. Effect of coolant channel diameter on LS-VHTR performance

Parameter	Coolant channel diameter, mm		
	9.53	**11.8**	**14.0**
Maximum fuel temperature Steady state/transient, °C	1329/1260	1312/1257	1304/1255
Vessel differential pressure, MPa	0.276	0.146	0.102
Total bypass, %	12.0	6.6	4.2

A parametric calculation was performed to determine the effect of bypass on the performance of the LS-VHTR. In the base calculation, the bypass through the gaps between the fuel and reflector columns was based on mechanistic estimates of the flow area and hydraulic diameter at cold conditions. In the parametric calculation, the hydraulic diameter of the gaps was arbitrarily increased by a factor of 5. As a result, the bypass flow around the core increased to 18.3% of the total, with 11.2% of the flow passing through the gaps. The additional bypass flow reduced the flow through the coolant channels and increased the maximum fuel temperature by 12°C at steady state. However, the increased bypass flow did not significantly affect the response of the LS-VHTR following a LOFC. The maximum fuel temperature following the reactor scram increased by less than 1°C from that shown previously.

A parametric calculation was performed to determine the effects of making the LS-VHTR core more compact by reducing the number of fueled rings from ten to nine. The number of fuel columns decreased from 265 to 211. The radial dimensions of the outer reflector, core barrel, reactor and guard vessels, and RVACS were decreased commensurate with the reduced number of fueled rings.

The effects of the number of fueled rings on calculated parameters at steady state are shown in Table 6.4. The reduced number of fuel columns increased the power density in the core by 26%, which increased the average and maximum fuel temperatures by 30 and 58°C, respectively. The reduced number of coolant channels increased the pressure drop across the core by 48%. The increased pressure drop across the coolant channels caused the bypass flow fraction to increase by 16%. The heat removal by the RVACS decreased by 8% because the reduced radii of the reactor and guard vessels reduced the area for heat transfer.

The reduced number of fueled rings caused the maximum fuel temperature during the transient to increase by nearly 70°C as shown in Fig. 6.9. An extrapolation of these results indicates that a further reduction in the number of fueled rings from nine to eight would result in a maximum transient temperature that was near the boiling limit of 1430°C.

Table 6.4. Effect of number of fueled rings on calculated parameters at steady state

Parameter	Value	
	10 rings	9 rings
Core power, MW	2400	2400
Mass flow rate, kg/s	10,264	10,264
Core inlet temperature, °C	900	900
Core outlet temperature, °C	1000	1000
Average fuel temperature, °C	1093	1123
Maximum fuel temperature, °C	1329	1387
Maximum RV temperature, °C	750	749
Total bypass, %	12.0	13.9
Gaps between blocks, %	4.4	5.3
Engineered bypass, %	5.6	6.2
Siphon breaker, %	2.0	2.3
Core pressure drop, MPa	0.211	0.312
Vessel pressure drop, MPa	0.276	0.376
RVACS heat removal, MW	6.2	5.7

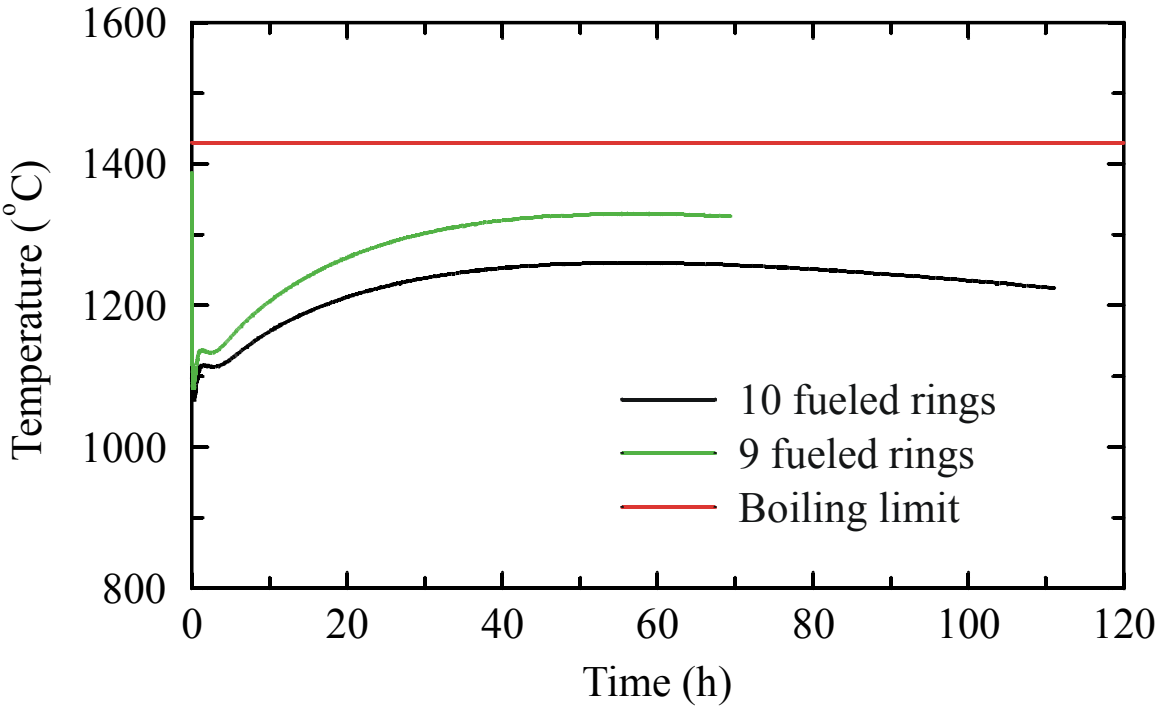

Fig. 6.9. The effect of the number of fueled rings on the maximum fuel temperature following a LOFC.

A parametric calculation was performed to investigate the effects of coolant temperature on the performance of the LS-VHTR. The coolant inlet and outlet temperatures were reduced by 250°C from the values shown in Table 6.2, with resulting values of 650 and 750°C, respectively. The 250°C reduction in coolant temperature reduced the average and maximum fuel temperatures by 229 and 215°C, respectively, at steady state. The reduction in fuel temperatures was less than the change in coolant temperatures because the thermal conductivities of the graphite, helium, and fuel compact increase with temperature. The heat transfer coefficient also increases with temperature because of the changes in the coolant viscosity. The maximum fuel temperature was 1114°C, well below the steady-state limit of 1250°C. The maximum reactor vessel temperature during steady state operation was reduced by 161°C from 750 to 589°C.

The effect of the initial coolant temperature on the power removed by RVACS is shown in Fig. 6.10. The lower coolant temperature initially reduced the power removed by RVACS by more than 40%, but the relative effect decreased during the transient. The lower initial coolant temperature also delayed the time when the power removed by RVACS exceeded the core decay power by about 40 h.

The initial coolant temperature significantly affected the maximum fuel temperature following a LOFC. Figure 6.11 shows that the lower initial coolant temperature reduced the maximum fuel temperature by 90°C to 1170°C during the transient. The lower initial coolant temperature also resulted in a slower increase in fuel temperature during the transient and delayed the occurrence of the maximum fuel temperature. During the LOFC transient, the peak vessel temperature dropped from 985 to 923°C and occurred at 100 h instead of 60 h.

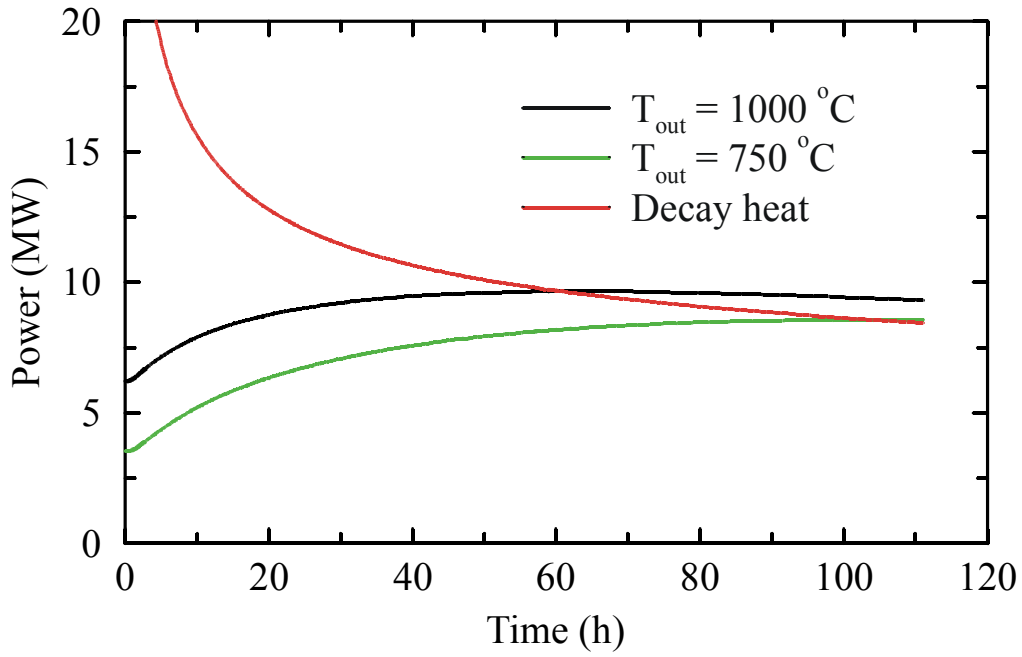

Fig. 6.10. The effect of initial coolant temperature on the power removed by RVACS.

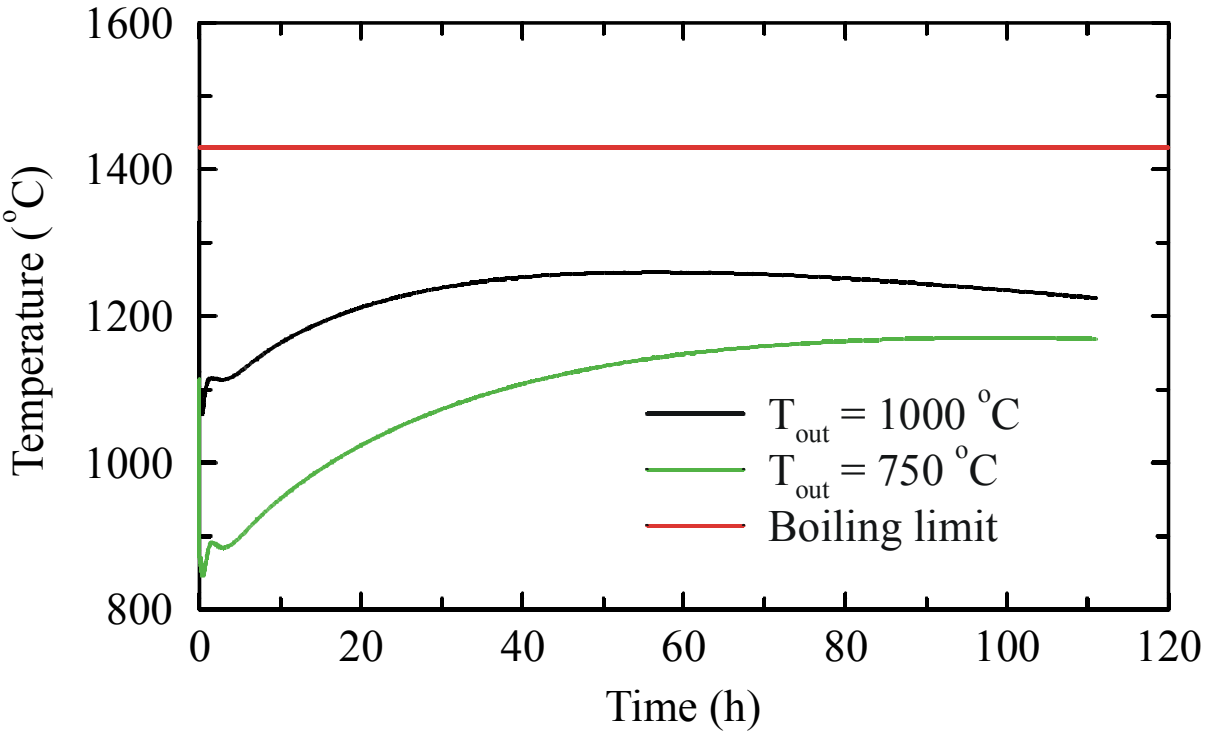

Fig. 6.11. The effect of initial coolant temperature on the maximum fuel temperature following a LOFC.

A final parametric calculation was performed to investigate the effects of radial and axial conduction in the core. In the base calculation, the effects of radial conduction between fuel columns and axial conduction within a fuel column were simulated using an enclosure model similar to the one developed for the NGNP [MacDonald, 2003]. In the parametric calculation, the conduction enclosure model was deleted, leaving natural circulation of the liquid salt as the only heat transfer transport mechanism between the core and the thermal blanket system after the LOFC.

The parametric calculation showed that radial and axial conduction are not important heat transport mechanisms in the LS-VHTR, a very different result from that obtained in the gas-cooled NGNP. The maximum fuel temperatures at steady state and during the transient in the parametric calculation differed by less than 1°C from the results obtained in the base calculation. Thus, natural circulation is the dominant heat transport mechanism following LOFC in the LS-VHTR.

6.4 ENHANCED RVACS

The calculations discussed previously were based on the PRISM RVACS design [GE, 1986]. An enhanced RVACS design has been proposed for S-PRISM [Boardman, 2000] as illustrated in Fig. 6.12. The enhanced RVACS design utilizes ribs to trip the boundary layer and increase the heat transfer coefficient in the riser because of thermal entry region effects. The enhanced design also includes a perforated plate to increase the surface area for heat transfer.

A RELAP5-3D model of the enhanced RVACS design was developed. The boundary layer trips were modeled by increasing the heat transfer coefficient on the outer surface of the guard

vessel, which is referred to as the containment vessel in the figure, and the inner surface of the collector cylinder by a factor of 1.6. This factor accounts for the enhanced heat transfer in the thermal entry region for a circular tube with constant heat rate [Kayes, 1980] assuming that the ribs are effective in tripping the boundary layer. The perforated plate was modeled as an additional heat structure in the riser. The holes in the perforated plate, which were assumed to occupy 40% of the surface area, allowed the guard vessel to radiate to both the perforated plate and the collector cylinder. The gaps on either side of the perforated plate were represented as a single flow path in the model.

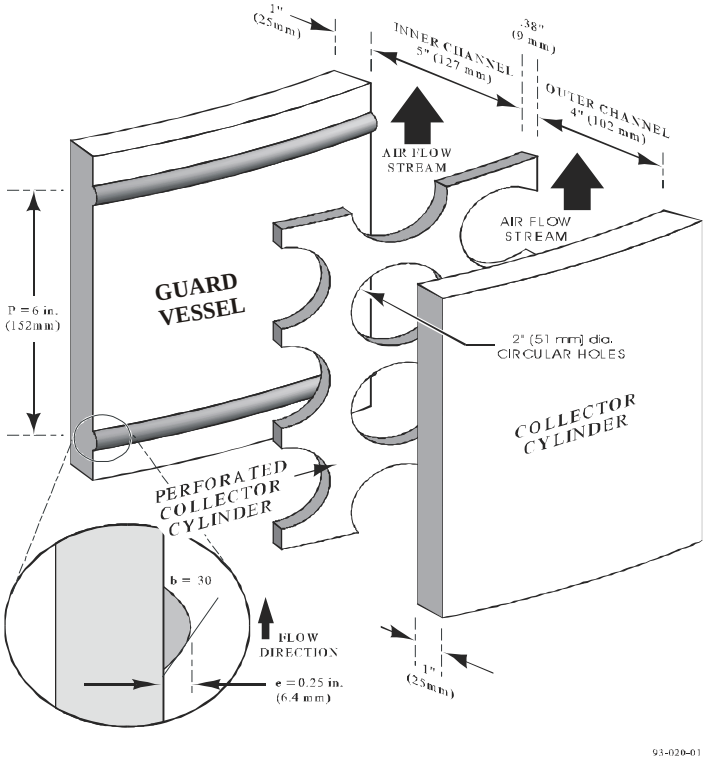

Fig. 6.12. Enhanced RVACS for S-PRISM.

The enhanced design increased the power removed by RVACS by 26% at steady state. Most of the increased heat transfer was due to the ribs. The effects of the RVACS enhancements on the power removed during the transient are shown in Fig. 6.13. The power removed by RVACS exceeded the core decay power about 30 h earlier with the enhanced design and the maximum fuel temperature was 87°C lower as shown in Fig. 6.14. The peak vessel temperature dropped to 905°C and occurred at 31 h. Although the enhanced RVACS appears to improve the decay heat removal parameters, it is only a proposed concept, and there are no direct data to substantiate the choice of heat transfer values used in this study or to validate the overall effectiveness of the enhancements.

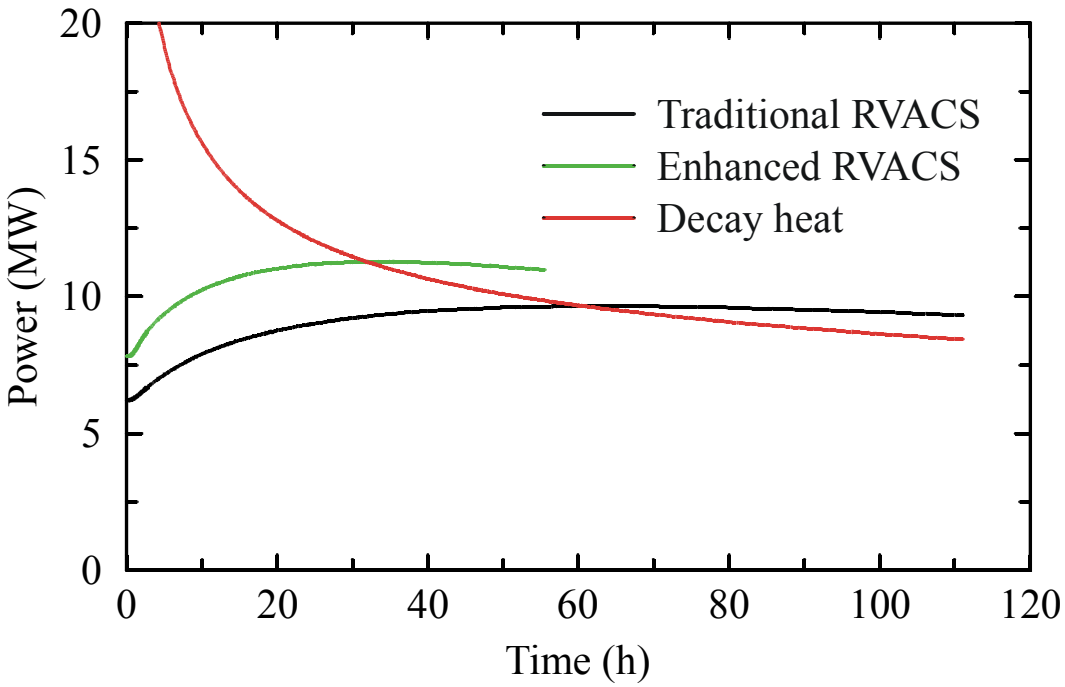

Fig. 6.13. The effect of design enhancements on the power removed by RVACS.

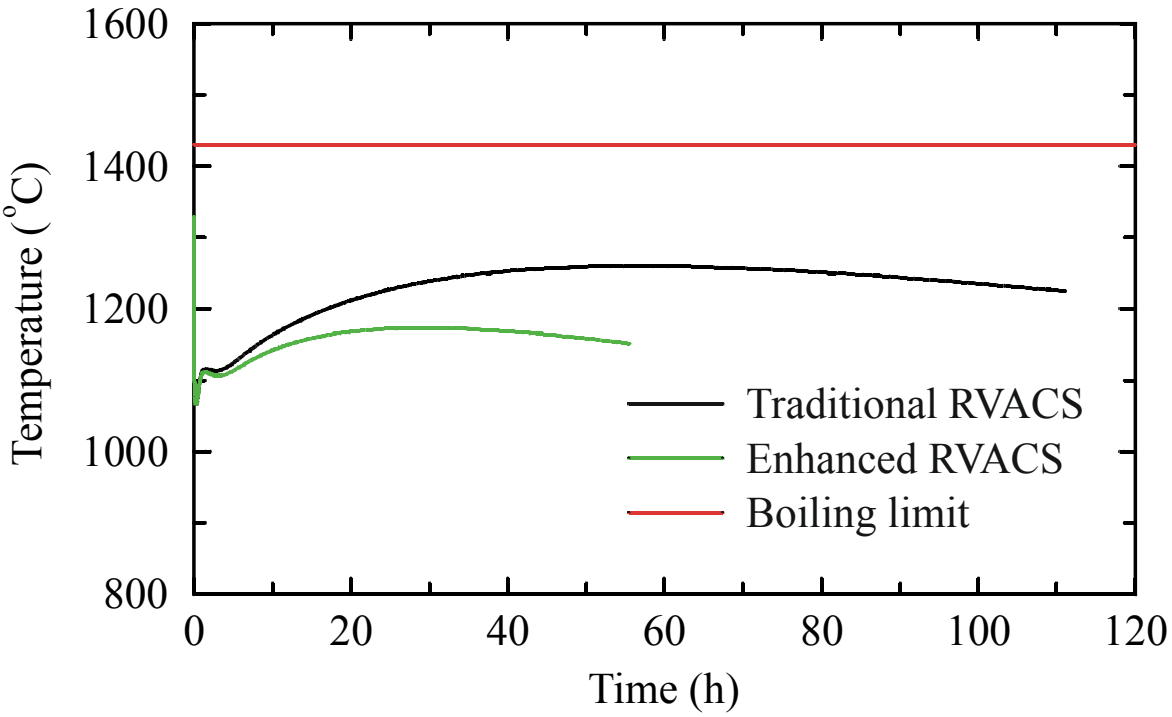

Fig. 6.14. The effect of RVACS design enhancements on the maximum fuel temperature following a LOFC.

6.5 LOFC WITH FAILURE TO SCRAM

A parametric calculation was performed to investigate the performance of the LS-VHTR following LOFC with a failure to scram. The Doppler reactivity feedback coefficient was assumed to be –0.01$/°C. The coolant density feedback coefficient was calculated from a total voiding worth of –0.03$.

The effect of the failure to scram on reactor power is shown in Fig. 6.15. In the base calculation, the scram quickly reduced the power to decay heat levels. Without scram, the LOFC caused the fuel temperature to increase which caused negative reactivity feedback and slowly reduced the core power. The reactivity feedback was eventually able to shut down the reactor.

The effect of the failure to scram on average fuel temperature is shown in Fig. 6.16. The LOFC coupled with a failure to scram caused the average fuel temperature to increase until reaching a peak near 90 s. The fuel temperature then decreased in response to the reduction in power caused by reactivity feedback and the establishment of natural circulation flow. However, the fuel temperature increased again in the long term because the core decay power exceeded that removed by the RVACS. Figure 6.17 shows that the maximum fuel temperature without scram remained above the corresponding value with scram for the duration of the transient. A long-term maximum in fuel temperature occurred near 50 h, but this maximum was about 70°C less than the peak value that occurred early in the transient. These results indicate the LS-VHTR can withstand a failure to scram and still remain below the boiling limit.

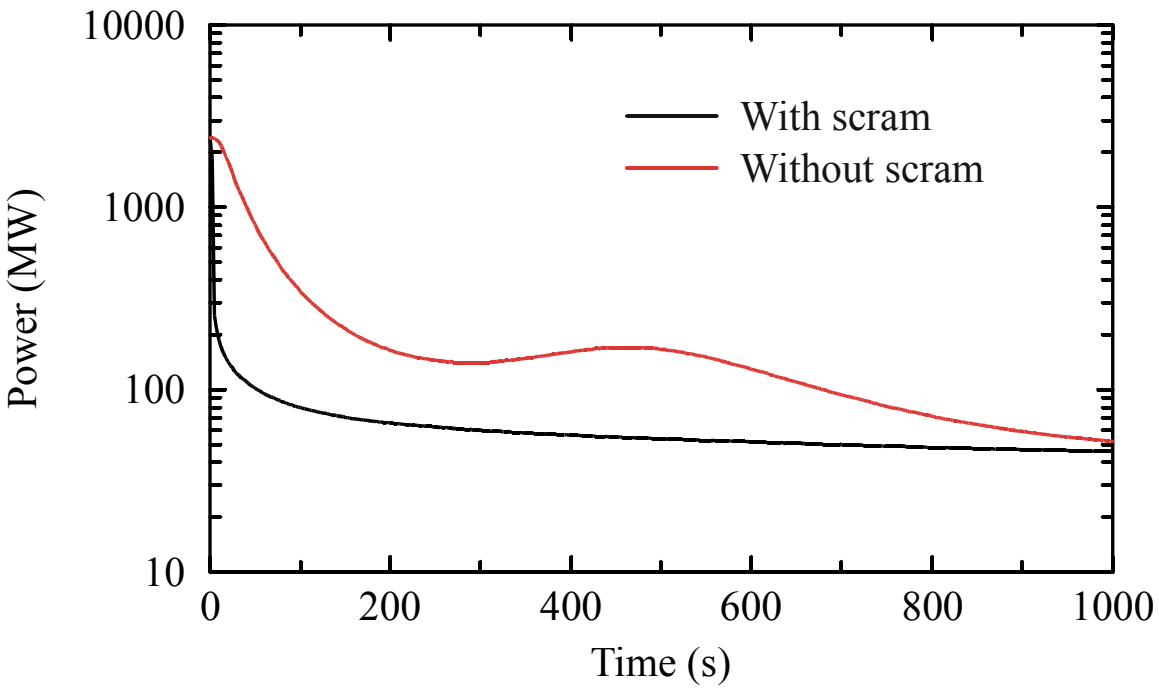

Fig. 6.15. The effect of a failure to scram on the reactor power following a LOFC (short term).

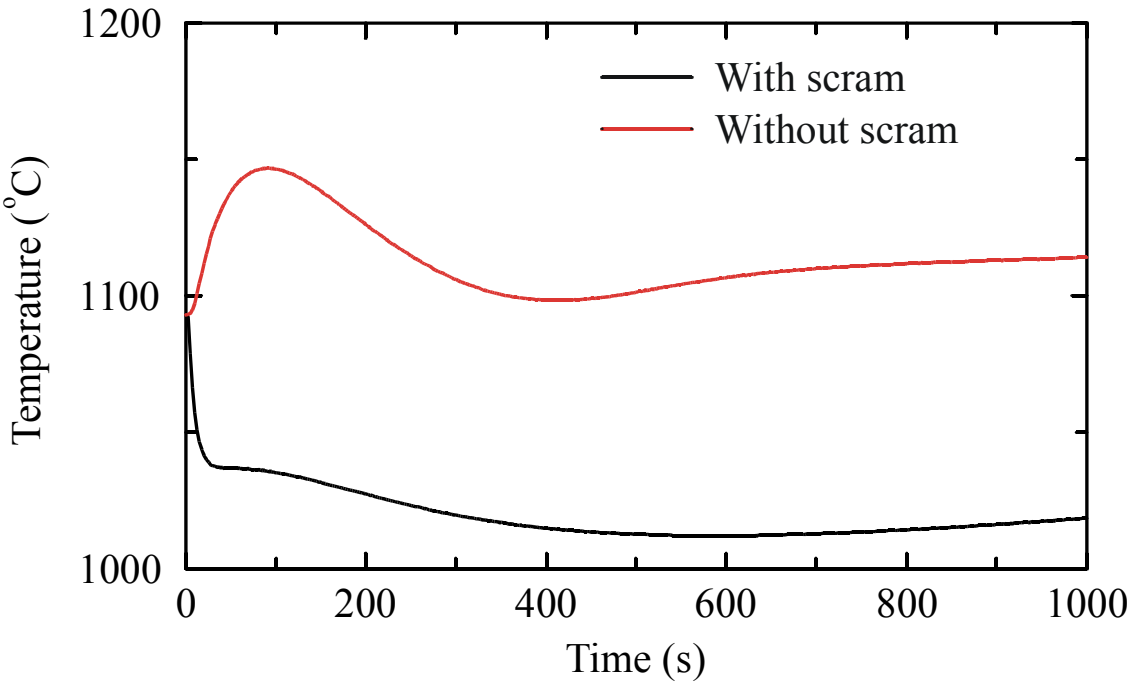

Fig. 6.16. The effect of a failure to scram on the average fuel temperature following a LOFC (short term).

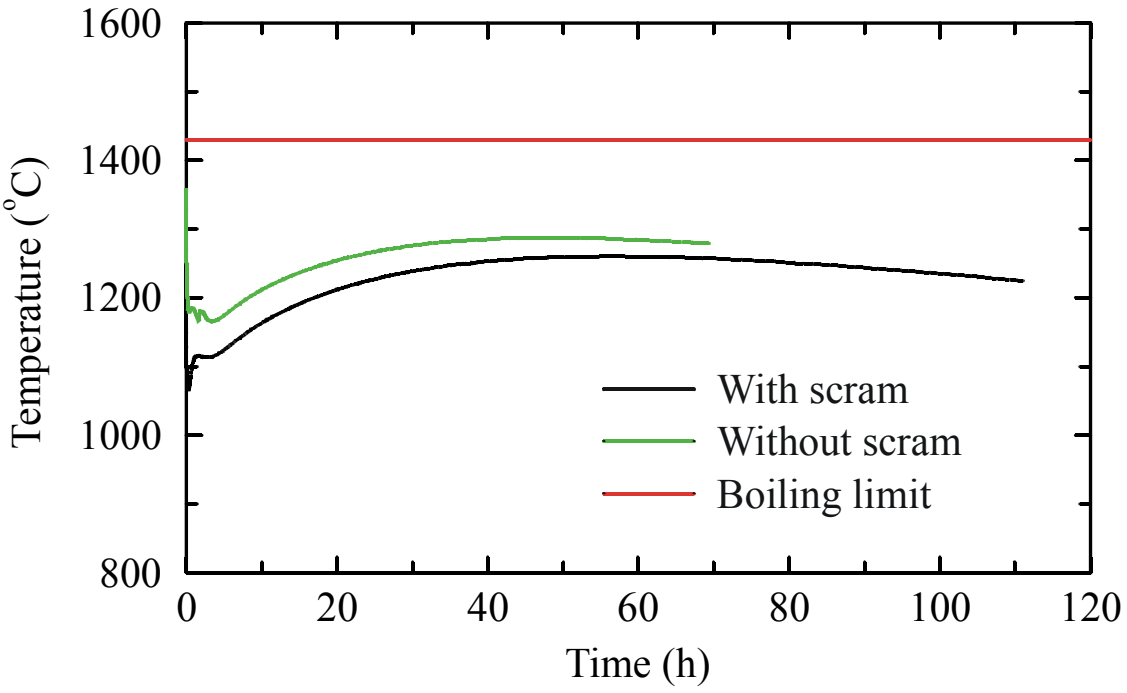

Fig. 6.17. The effect of a failure to scram on the maximum fuel temperature following a LOFC (long term).

6.6 CONCLUSIONS ON SAFETY ANALYSES

The RELAP5-3D one-dimensional annular model accurately represents the heat conduction process in a unit cell of a fuel block. Fuel centerline temperatures calculated with the one-dimensional RELAP5-3D model were within 2.2°C of the values obtained with a multidimensional ABAQUS model for a wide range of volumetric power generation rates.

The RELAP5-3D model of the LS-VHTR was used to simulate the reactor's performance during steady operation and during a transient initiated by a LOFC. Steady operation at full power is more challenging than the transient with regards to temperature limits. In fact, the maximum predicted fuel temperature with this year's design was about 1330°C, which exceeds the steady state temperature limit of 1250°C. A variety of options are available to lower the maximum fuel temperature, including lowering the operating power or fluid temperature. The maximum calculated fuel temperature during the transient was about 1260°C and occurred about 60 h after the LOFC. The peak fuel temperature during the transient was less than the temperature during normal operation and was considerably less than the transient temperature limit of 1430°C. Natural circulation of the liquid salt was the dominant heat transport mechanism within the reactor vessel. Transient temperature limits were met even with a failure to scram.

An RVACS model based on the PRISM design was able to adequately cool the LS-VHTR, even with a decay heat curve that was about 30% higher than best-estimate calculations of a similar gas-cooled reactor. An enhanced RVACS model based on the proposed S-PRISM design was also developed. The maximum fuel temperature during the transient was reduced by about 90°C with the enhanced RVACS. However, because the temperature response during the transient is less limiting than that during normal operation, RVACS enhancements are not needed at this time. Also, there are no data to substantiate the apparent benefits of the enhanced design and justify the additional design complexity. RELAP5-3D should be benchmarked against RVACS experiments to provide additional confidence in the predicted results, including for the enhanced RVACS.

The effectiveness of the RVACS during a transient in which salt leaks into the gap between the reactor and guard vessels should be evaluated further. A preliminary evaluation indicated that the performance of the RVACS would be degraded significantly if conduction through the salt is the only heat transport mechanism. Experiments to determine the effectiveness of convection and radiation in small gaps filled with liquid salt would be useful in determining the viability of the RVACS design for the LS-VHTR.

As expected, the maximum fuel temperatures are significantly affected by the coolant temperature. Lowering the operating coolant temperature by 250°C lowered the maximum fuel temperature by 215°C to 1114°C at steady state and by 90°C to 1170°C during the transient. . The maximum reactor vessel temperature was reduced by 161°C to 589°C during steady-state operation and by 62°C to 923°C during the LOFC transient.

A thermal-hydraulic evaluation indicated that it may be possible to lower the cost of the LS-VHTR by making the core more compact. Reducing the number of fueled rings in the core from ten to nine increased the maximum fuel temperature by about 60°C at steady state and 70 °C during the transient. Reducing the number of core rings can be considered further once the design is modified to meet fuel temperature limits during normal operation by at least 60°C.

The thermal-hydraulic performance of the LS-VHTR improved as the diameter of the coolant channels increased. Increasing the diameter of the coolant channel from 9.53 to 14.0 mm reduced the pressure drop across the core by more than 60% at steady state. The larger diameter also reduced the maximum fuel temperature by 25°C at steady state but had only a small effect during the transient.

This page intentionally blank

7. SUMMARY AND RECOMMENDATIONS

7.1 SUMMARY

The objective of the present study was to develop a new baseline design core design for the liquid-salt-cooled VHTR relative to the 2004 study [Ingersoll, 2004]. Specifically, it was intended to develop a core design that is better optimized for liquid coolant and that satisfies the top level operational and safety targets—demonstrate strong passive safety performance, achieve a fuel cycle length of at least 18 months with a fuel discharge of greater than 100 GWd/t, and have a negative reactivity response to coolant voiding.

Three organizations participated in the study—ORNL, INL, and ANL. Each organization used computational methods that were independently developed. Also, each organization had distinct areas of responsibility with some areas of overlap for comparison. Although the intent was to generate a new reference LS-VHTR design, the emphasis was on performing parametric studies of the many variables that constitute a core design. The results of the parametric studies not only provide the basis for choosing the optimum balance of design options, they also provide a valuable understanding of the fundamental behavior of the core, which will be the basis of future design trade-off studies.

The study successfully met the primary objective (i.e., a new baseline LS-VHTR core design has been identified that satisfies the top level design targets). Specific conclusions regarding the core and coolant characterizations, the neutronics analyses and the safety analyses are given at the end of each of the corresponding sections of this report.

7.2 REVISED LS-VHTR PARAMETERS

Based on the results of the extensive analyses performed for this study, only modest refinements to the initial baseline design have been made. The key parameters for the initial and revised baseline designs are listed in Table 7.1. Although only a few parameters changed (inlet/outlet coolant temperatures and coolant channel diameter), a defensible basis was established for leaving the other parameters unchanged. Also, parameters such as uranium enrichment and fuel packing fraction, which were variables at the beginning of the study, now have baseline values. The selection of baseline dimensions and parameters is still somewhat qualitative and lacks rigorous optimization. Generally, values were selected that are near the middle of the preferred ranges indicated by the parametric studies. This should permit further refinement in future studies without exceeding design constraints

The coolant channel diameter was increased to help decrease the maximum fuel temperature, which was found to be nearly 80°C above the operational limit of 1250°C for the initial baseline design. The combined effect of increasing the coolant channel diameter from 0.953 to 1.4 cm and reducing the inlet and outlet coolant temperatures by 50°C should result in an acceptable maximum fuel temperature. Increasing the diameter of the coolant channel also helps to reduce the coolant void reactivity response of the core.

Although removing the outer row of fuel blocks appeared practical from the stand point of decay heat removal, it resulted in increases in power density and fuel temperature beyond the target values provided by fuels experts. Also, although alternative fuel block designs and a parfait core design may offer some attractive fuel handling or reactivity response features, the

benefits do not appear significant, and their impact on fuel cycle parameters has not been evaluated yet. Therefore, the current design retains the original fuel block design (Fig. 1.2). The same is true for the RVACS design, because the predicted benefits of the enhanced design have not been substantiated yet and the traditional design appears sufficient to provide good passive decay heat removal performance.

Table 7.1. Key parameters for initial and revised baseline LS-VHTR design

Parameter	Initial value	Revised value
Total power output	2400 MW(t)	2400 MW(t)
Coolant salt	^{2}LiF-BeF_2	^{2}LiF-BeF_2
^{7}Li isotopic concentration	99.995%	99.995%
Outlet coolant temperature	1000°C	950°C
Inlet coolant temperature	≥850°C	850°C
Reactor vessel diameter	9.2 m	9.2 m
^{235}U enrichment	≤20%	15%
Particle packing fraction	≤30%	25%
Fuel cycle length	≥18 months	18 months
Discharge burnup	≥100 GWd/t	156 GWd/t
Fuel shuffling	≤3 batches	2 batch
Fuel element:		
Fuel channel diameter	1.27 cm	1.27 cm
Number of fuel channels	216	216
Coolant channel diameter	0.953 cm	1.4 cm
Number of coolant channels	108	108
Pitch between channels	1.88 cm	1.88 cm
Power density	10.0 MW/m^3	10.0 MW/m^3
Number of fuel columns	265	265

The revised design appears to have excellent steady-state and transient performance. The previous concern regarding the core's response to coolant voiding has been resolved for the case of Flibe coolant by increasing the coolant channel diameter and the fuel loading. As a result, the coolant void reactivity feedback appears to be negative, especially for fuel burnup greater than 15 GWd/t. The use of a BP such as erbium is necessary for the startup core, although using it for all cores may be desirable to further reduce the coolant void reactivity and for improved reactor control.

Even with conservative data and analyses, the LS-VHTR has a strong passive safety performance and appears capable of surviving a LOFC even with failure to scram. Significant natural convection of the coolant salt occurs, resulting in fuel temperatures below steady-state values and nearly uniform temperature distributions during the transient.

7.3. FUTURE ACTIVITIES

The present study was successful in developing a LS-VHTR core design with acceptable steady-state and transient response with a total power output of 2400 MW(t). However, considerable effort is needed to further develop, optimize, and validate the design. The most immediate needs are summarized below.

- The current design focused on only Flibe, which is clearly the most favorable from a neutronics perspective. Toxicity concerns for beryllium-containing materials and the potential expense of ^{7}Li enrichment motivate the interest in considering other candidate salts. These other salts need to be evaluated in terms of their impact on the physics and thermal-hydraulic performance of the LS-VHTR and may require design changes to compensate for their less favorable neutronics properties.
- A more detailed design of the reactor core and vessel internals must be developed, including core supports, vessel insulation, control and shutdown systems, flow baffles, etc. The ultimate performance of the reactor will be substantially impacted by the details of the design. Specific materials will need to be selected consistent with the final coolant choice, temperature distributions, and radiation environments.
- Basic phenomenology associated with potential accidents, including "beyond design basis" accidents, must be studied and prioritized as a guide to the safety validation process.
- Fundamental salt properties and chemistry at higher temperatures must be studied. Previous studies for salts in nuclear environments were limited to 700–800°C and must be extended above 1000°C to cover the temperature range resulting from transients.
- Numerous coolant validation experiments need to be conducted to study coolant performance, such as mixing in the inlet/outlet plena, conductive and radiative heat transfer across small salt-filled gaps, etc.

In addition to these activities, which are focused on the primary system, the secondary side of the LS-VHTR and the balance of plant also need to be developed further, including the dynamic modeling of the entire plant. This will be especially important in developing a cogeneration plant capable of producing both electricity and hydrogen.

Finally, activities should include a study of the licensing basis for a LS-VHTR, the development and operation of a small-scale liquid-salt-cooled test reactor and the development of a demonstration-scale reactor.

This page intentionally blank

REFERENCES

[AEA, 1999] "WIMS—A Modular Scheme for Neutronics Calculations," User's Guide for Version 8, ANSWER/WIMS(99)9, The ANSWERS Software Package, AEA Technology.

[ANS, 1979] American Nuclear Society, *Decay Heat Power in Light Water Reactors*, ANSI/ANS-5.1, 1979.

[Boardman, 2000] C. E. Boardman, A. E. Dubberly, D. G. Carroll, M. Hui, A. W. Fanning, and W. Kwant, "A Description of the S-PRISM Plant," ICONE-8168, *Proceedings of ICONE-8, Baltimore, Maryland, April 2–6, 2000*.

[Clarno, 2005] K. T. Clarno, C. W. Forsberg, and J. C. Gehin, "Physics Analysis of Coolant Voiding in the Advanced High-Temperature Reactor (AHTR)," to be published in *Trans. Am. Nucl. Soc.*, ANS Winter Meeting, Washington D.C. (2005).

[Davis, 2005a] C. B. Davis, T. D. Marshall, and K. D. Weaver, "Modeling the GFR with RELAP5-3D," *2005 RELAP5 International Users Seminar, Jackson Hole, Wyoming, September 7–9, 2005*.

[Davis, 2005b] C. B. Davis, *Implementation of Molten Salt Properties into RELAP5-3D/ATHENA*, INEEL/EXT-05-02658, January 2005.

[Driscoll, 1990] M. J. Driscoll et al, "The Linear Reactivity Model for Nuclear Fuel Management," American Nuclear Society, 1990.

[Ducat, 1974] G. A. Ducat, M. J. Driscoll, and N. E. Todreas, *Evaluation of the Parfait Blanket Concept for Fast Breeder Reactors*, MIT AEC Research and Development Report, COO-2250-5, MITNE-157, January 1974.

[Forsberg, 2003] C. W. Forsberg, P. Pickard, and P. F. Peterson, "Molten-Salt-Cooled Advanced High-Temperature Reactor for Production of Hydrogen and Electricity," *Nuclear Technology*, **144**, 289–302 (2003).

[Forsberg, 2005a] C. W. Forsberg, "Brayton Power Cycles and High-Temperature Salt-Cooled Reactors," *ANS Transactions*, **92**, 231 (2005).

[Forsberg, 2005b] C. W. Forsberg and K. T. Clarno, "The Advanced High-Temperature Reactor (AHTR): Flux Distribution and Dosimetry," to Be Published in *J. ASTM Intl*. (2005).

[GA, 1977] General Atomics, *Safety Analysis Report Use of H-451 Graphite in Fort St. Vrain Fuel Elements*, GLP-5588, December 1977.

[GA, 1996] General Atomics, *Gas Turbine-Modular Helium Reactor (GT-MHR) Conceptual Design Description Report*, Revision 1, Report 910720, GA Project No. 7658, July 1996.

[GE, 1986] General Electric, *Preliminary Safety Information Document*, Volume II, GEFR-00793, UC-87Ta, November 1986.

[Hibbitt, 2005] Hibbitt, Karlsson & Sorensen, Inc., *ABAQUS Version 6.4-4*, 2005.

[Holman, 1986] J. P. Holman, *Heat Transfer*, Sixth Edition, McGraw-Hill Book Company, New York, 1986.

[Hunsbedt, 1988] A. Hunsbedt and P. M. Magee, "Design and Performance of the PRISM Natural Convection Decay Heat Removal System," *Proceedings of the International Topical Meeting on Safety of Next Generation Power Reactors, Seattle Washington, May 1–5, 1988*, pp. 844–51.

[INEEL, 2003] *RELAP5-3D Code Manual*, Rev. 2.2, INEEL EXT-98-00834, October 2003.

[Ingersoll, 2004] D. T. Ingersoll et al., "Status of Preconceptual Design of the Advanced High-Temperature Reactor (AHTR)," ORNL/TM-2004/104, Oak Ridge National Laboratory, May 2004.

[Janz, 1992] G. J. Janz (preparer), *"NIST Properties of Molten Salts Database, Version 2.0,"* NIST Standard Reference Database 27, National Institute of Standards and Technology, Gaithersburg, MD (1992).

[Kayes, 1980] W. M. Kayes and M. E. Crawford, *Convective Heat and Mass Transfer*, Second Edition, McGraw-Hill Book Company, New York, 1980.

[Kim, 2004a] T. K. Kim, W. S. Yang, T. A. Taiwo, and H. S. Khalil, *Whole-Core Depletion Studied in Support of Fuel Specification for the Next Generation Nuclear Plant (NGNP)*, Argonne National Laboratory Gen IV Report, July 30, 2004.

[Kim, 2004b] T. K. Kim, W. S. Yang, M. A. Smith, T. A. Taiwo, and H. S. Khalil, *Assessment of Monte Carlo and Deterministic Codes for Next Generation Nuclear Plant (NGNP) Core Modeling*, Argonne National Laboratory Gen IV Report, April 15, 2004.

[LANL, 1993] *MCNP—A General Monte Carlo N-Particle Transport Code*, Version 4C, Los Alamos National Laboratory, LA-13709-M (1993).

[LANL, 2004] *MCNP—A General Monte Carlo N-Particle Transport Code, Version 5—Volume I: Overview and Theory*, LA-UR-03-1987, Los Alamos National Laboratory (April 2003, revised June 2004).

[MacDonald, 2002] P. E. MacDonald and J. Buongiorno, *Design of an Actinide Burning, Lead or Lead-Bismuth Cooled Reactor That Produces Low Cost Electricity*, INEEL/EXT-02-01249, MIT-ANP-PR-092, October 2002.

[MacDonald, 2003] P. E. MacDonald et al., *NGNP Preliminary Point Design—Results of Initial Neutronics and Thermal-Hydraulic Assessment During FY-03*, INEEL/EXP-03-00870, Rev. 1, Idaho National Engineering and Environmental Laboratory (September 2003).

[MacDonald, 2005] P. E. MacDonald et al., *Feasibility Study of Supercritical Light Water Cooled Reactors for Electric Power Production*, INEEL/EXT-04-02530, January 2005.

[McDonald, 2005] J. M. McDonald, R. E. Nygren, T. J. Tanaka, M. A. Ulrickson, T. J. Boyle, and K. P. Troncosa, "Measurement of the Melting Point Temperature of Several Lithium-Sodium-Beryllium Fluoride Salt (FLINABE) Mixtures," Sandia National Laboratories, P.O. Box 5800, Albuquerque, NM 87105, *Fusion Science and Technology*, **47**(3) (April 2005).

[Marleau, 1998] G. Marleau,et al, *A User Guide for DRAGON*, Technical report IGE-174 Rev. 4, Ecole Polytechnique de Montréal, September 1998.

[Naka, 2003] Naka-machi, Naka-gun, and Ibaraki-ken, "*Annual Report of Naka Fusion Research Establishment from April 1, 2002 to March 31, 2003"*, Naka Fusion Research Establishment, Japan Atomic Energy Research Institute, http://www-jt60.naka.jaeri.go.jp/english/annual/03/html/

[ORNL, 2004] *SCALE: A Modular Code System for Performing Standardized Computer Analysis for Licensing Evaluation*, NUREG/CR-0200, Rev. 7 (ORNL/NUREG/CSD-2/R7), Vols. I, II, and III, June 2004 (DRAFT). Available from Radiation Safety Information Computational Center at Oak Ridge National Laboratory as CCC-725.

[Potter, 1996] R. C. Potter and A. Shenoy, *Gas Turbine-Modular Helium Reactor (GTMHR) Conceptual Design Description Report*, GA Report 910720, Revision 1, General Atomics, July 1996.

[Thoma, 1971] R. E. Thoma, *Chemical Aspects of MSRE Operations*, ORNL-4658, Oak Ridge National Laboratory, 1971.

[Toppel, 1983] B. J. Toppel, *A User's Guide to the REBUS-3 Fuel Cycle Analysis Capability*, ANL-83-2, Argonne National Laboratory, 1983.

[Weinberg, 1970] A. M. Weinberg et al., "The Status and Technology of Molten Salt Reactors—A Review of Work at the Oak Ridge National Laboratory", *Nucl. Appl. Tech.* **8**(2) (February 1970).

[Williams, 2005a] D. F. Williams et al., *Assessment of Properties of Candidate Liquid Salt Coolants for the Advanced High Temperature Reactor (AHTR)*, ORNL/GEN4/LTR-05-001, June 30, 2005.

[Williams, 2005b] D. F. Williams and L. M. Toth, *Chemical Considerations for the Selection of the Coolant for the Advanced High-Temperature Reactor*, ORNL/GEN4/LTR-05-011, September 14, 2005.

INTERNAL DISTRIBUTION

1. S. J. Ball (ballsj@ornl.gov)
2. J. L. Binder (binderjl@ornl.gov)
3. K. T. Clarno (clarnokt@ornl.gov)
4. W. R. Corwin (corwinwr@ornl.gov)
5. C. W. Forsberg (forsbergcw@ornl.gov)
6. J. C. Gehin (gehinjc@ornl.gov)
7. S. R. Greene (greenesr@ornl.gov)
8. G. E. Kulynych (kulynychge@ornl.gov)
9. G. T. Mays (maysgt@ornl.gov)
10. G. E. Michaels (michaelsge@ornl.gov)
11. L. J. Ott (ottlj@ornl.gov)
12. C. V. Parks (parkscv@ornl.gov)
13. A. L. Qualls (quallsal@ornl.gov)
14. J. E. Rushton (rushtonje@ornl.gov)
15. D. F. Williams (williamsdf2@ornl.gov)
16. D. F. Wilson (wilsondf@ornl.gov)
17. T. L. Wilson Jr. (wilsontljr@ornl.gov)
18. G. L. Yoder Jr. (yodergljr@ornl.gov)
19. ORNL Central Research Library (conradre@ornl.gov)
20. ORNL Laboratory Records—RC (hamrindr@ornl.gov)

EXTERNAL DISTRIBUTION

21. T. L. Cook, NE-20/Germantown Building, U.S. Department of Energy, 1000 Independence Ave., S.W., Washington, DC 20585-1290 (trevor.cook@hq.doe.gov)
22. C. B. Davis, Idaho National Laboratory, 2525 N. Fremont Avenue, P. O. Box 1625, Idaho Falls, ID 83415 (cliff.davis@inl.gov)
23. G. L. Hawkes, Idaho National Laboratory, 2525 N. Fremont Avenue, P. O. Box 1625, Idaho Falls, ID 83415 (grant.hawkes@inl.gov).
24. R. Kochendarfer, 3315 Old Forest Road, P.O. Box 10935, Lynchburg, VA 24506-0935 (richard.kochendarfer@framatome-anp.us)
25. T. K. Kim, Argonne National Laboratory, 9700 S. Cass Avenue, Argonne, IL 60439 (tkkim@anl.gov)
26. T. K. Larson, Idaho National Laboratory, 2525 N. Fremont Avenue, P. O. Box 1625, Idaho Falls, ID 83415 (thomas.larson@inl.gov)
27. P. E. MacDonald, 2943 Sonterra Drive, Cedar Hill, TX 75104 (pemcedarhill@yahoo.com)
28. P. F. Peterson, University of California, Berkeley, Nuclear Engineering Department, 4153 Etcheverry Hall, Berkeley, CA 94720-1730 (peterson@nuc.berkeley.edu)
29. P. S. Pickard, Sandia National Laboratories, P. O. Box 5800, Albuquerque, NM 87185-1136 (pspicka@sandia.gov)
30. R. Schultz, Idaho National Laboratory, 2525 N. Fremont Avenue, P. O. Box 1625, Idaho Falls, ID 83415 (richard.schultz@inl.gov)
31. K. Sridharan, University of Wisconsin, 1500 Engineering Drive, Madison, WI 53706 (kumar@engr.wisc.edu)
32. J. W. Sterbentz, Idaho National Laboratory, 2525 N. Fremont Avenue, P. O. Box 1625, Idaho Falls, ID 83415 (james.sterbentz@inl.gov) .

33. T. A. Taiwo, Argonne National Laboratory, 9700 S. Cass Avenue, Argonne, IL 60439 (taiwo@anl.gov)
34. R. M. Versluis, NE-20/Germantown Building, U.S. Department of Energy, 1000 Independence Ave., S.W., Washington, DC 20585-1290 (rob.versluis@hq.doe.gov)
35. K. D. Weaver, Idaho National Laboratory, 2525 N. Fremont Avenue, P. O. Box 1625, Idaho Falls, ID 83415 (kevan.weaver@inl.gov)
36. W. S. Yang, Argonne National Laboratory, 9700 S. Cass Avenue, Argonne, IL 60439 (wyang@anl.gov)